NOAA Technical Report NOS CS 41

NOAA'S UPGRADED NORTHERN GULF OF MEXICO OPERATIONAL FORECAST SYSTEM: MODEL DEVELOPMENT AND HINDCAST SKILL ASSESSMENT

Silver Spring, Maryland

April 2022

noaa National Oceanic and Atmospheric Administration

U.S. DEPARTMENT OF COMMERCE
National Ocean Service
Coast Survey Development Laboratory

Office of Coast Survey
National Ocean Service
National Oceanic and Atmospheric Administration
U.S. Department of Commerce

The Office of Coast Survey (OCS) is the Nation's only official chartmaker. As the oldest United States scientific organization, dating from 1807, this office has a long history. Today it promotes safe navigation by managing the National Oceanic and Atmospheric Administration's (NOAA) nautical chart and oceanographic data collection and information programs.

There are four components of OCS:

The Coast Survey Development Laboratory develops new and efficient techniques to accomplish Coast Survey missions and to produce new and improved products and services for the maritime community and other coastal users.

The Marine Chart Division acquires marine navigational data to construct and maintain nautical charts, Coast Pilots, and related marine products for the United States.

The Hydrographic Surveys Division directs programs for ship and shore-based hydrographic survey units and conducts general hydrographic survey operations.

The Navigational Services Division is the focal point for Coast Survey customer service activities, concentrating predominately on charting issues, fast-response hydrographic surveys, and Coast Pilot updates.

NOAA Technical Report NOS CS 41

NOAA'S UPGRADED NORTHERN GULF OF MEXICO OPERATIONAL FORECAST SYSTEM: MODEL DEVELOPMENT AND HINDCAST SKILL ASSESSMENT

Zizang Yang, Philip Richardson, Edward P. Myers
Office of Coast Survey, Coast Survey Development Laboratory,
Silver Spring, Maryland

Lianyuan Zheng
Center for Operational Oceanographic Products and Services
Silver Spring, Maryland

April 2022

noaa **National Oceanic and Atmospheric Administration**

U. S. DEPARTMENT OF COMMERCE **Gina Raimondo,** **Secretary**	**National Oceanic and Atmospheric Administration** **Dr. Richard Spinrad,** **Under Secretary**	**National Ocean Service** **Nicole LeBoeuf,** **Assistant Administrator**

Office of Coast Survey **RDML Benjamin Evans** **Director**	**Coast Survey Development Laboratory** **Dr. Shachak Pe'eri** **Division Chief**

NOTICE

Mention of a commercial company or product does not constitute an endorsement by NOAA. Use for publicity or advertising purposes of information from this publication concerning proprietary products or the tests of such products is not authorized.

Table of Contents

List of Figures

LIST OF TABLES

EXECUTIVE SUMMARY

This report describes the development of the upgraded Northern Gulf of Mexico Operational Nowcast and Forecast System (NGOFS2) by the NOAA National Ocean Service. The NGOFS2 domain encompasses the broad coastal regions spanning from the northern coast of Mexico in the west to the U.S. Gulf Coast in the northwest, north, and northeast. The NGOFS2 will produce operational six-hour nowcast and up to 48-hour forecast guidance of water levels, three-dimensional (3-D) currents, water temperature, and salinity. It will support marine navigation, emergency response, search and rescue, offshore oil/gas operations, and the environmental management communities.

The NOS currently operates three OFSs in the northern Gulf of Mexico (NGOM). These three OFSs include the Northern Gulf of Mexico OFS (NGOFS), the nested northwestern Gulf of Mexico OFS (NWGOFS), and the nested northeastern OFS (NEGOFS). In addition to encompassing the combined NGOFS, NWGOFS, and NEGOFS domains, the NGOFS2 domain also includes the Lower Mississippi River course, Lake Pontchartrain, Barataria Bay, the lower Atchafalaya River, the Texas coastal inlets, intra-coastal waterways, embayments, and the northernmost portion of the Mexican coastal waters.

This report presents the NGOFS2 configuration, the hindcast setup, and the assessment of the hindcast results. The NGOFS2 uses the Finite Volume Community Ocean Model (FVCOM) as the core hydrodynamic model. Its model grid is composed of 303,714 nodes and 569,405 elements. The element size ranges from about 45 m in the nearshore area to around 11 km on the open ocean boundary. The finer scale elements favorably resolve the complex coastline and bathymetric features. The vertical coordinate was configured with 20 non-uniform sigma layers for the hindcast simulation.

We performed both a constant density, tidal forcing only simulation (Chapter 4) and a one year (August 2, 2016 – August 1, 2017) time period hindcast simulation (Chapter 5). The hindcast simulation included the full suite of forcing factors including tidal and non-tidal water levels, currents, water temperature, and salinity on the open ocean boundary, along with meteorological forcing on the surface, and river discharge. The tidal forcing data was based on the tidal database of the Advanced Circulation model (ADCIRC). The other forcing data included nowcasts from NCEP's G-RTOFS subtidal water levels, currents, water temperature, and salinity, as well as the sea-surface wind, mean sea level pressure, air temperature, and relative humidity forecast guidance from the NCEP's NAM weather forecast modeling system. USGS river discharge was also used as forcing data.

The modeled water levels, currents, surface water temperature, and salinity demonstrate generally favorable agreement with in situ observations. For the constant density tidal simulation (Chapter 4), over the 100 stations the averages of the absolute model-data difference of the tidal amplitudes are 1.5, 1.5, 1.1, and 1.76 cm for K_1, O_1, P_1, and M_2, respectively. The corresponding quantities for tide phase are 10.4, 9.5, 15.0, and 20.8 degrees, respectively. For the hindcast results (Chapter 5), the root-mean-squared errors are about 7.4 cm for water levels, about 0.19 cm/s for current speeds, about 12.4 degrees for the current direction, about 1.1 °C for water temperature, and about 3.8 psu for salinity. The NOS standard prescribes the criteria value as 0.15 cm for water level, 0.26

m/s for current speed, 22.5 degrees for the current phase, 3.0°C for water temperature, and 3.5 psu for salinity (Zhang, etc., 2006). The standard also prescribes a constant value of central frequency (CF) equal to 90% for all the above listed ocean state parameters. The corresponding central frequencies are around 90%, 82.8%, 95.0%, 96.0%, and 70.6%, respectively.

In addition to the hindcast simulations, multiple model runs were conducted to investigate the impacts of differing model configurations on the model generated water levels in the lower Mississippi River course (Chapter 6). The discussions cover such topics as (1) river discharge on the model grid nodes vs. on the model grid edges, (2) the impact of surface meteorological forcing and baroclinity, (3) nesting vs. non-nesting approaches to the open ocean boundary (OOB) forcings, (4) differences between the river discharge and the gauge height types of river forcing, (5) the impact of the vertical Prandtl number, and (6) vertical configurations using uniform vs. non-uniform coordinates. The study indicates that the model generated water level values, in general, are not sensitive to the differing configurations such as the forcing locations (nodes or elements) of the river discharge, being with or without surface forcing, the water baroclinity, the vertical Prandtl number, or the uniformity of the vertical coordinate. However, the study demonstrates appreciable differences between both the nesting and non-nesting types of OOB and between the discharge and the gauge height type river forcings. It is noted that in the hindcast setup, NGOFS2 used the nesting type OOB and the river discharge approach to river forcing.

At the time of this writing, the NOS has implemented the hindcast setup into the NOS standard HPC-COMF environment and has completed a one-year time period Nowcast/Forecast (N/F) test run and the associated skill assessment. The model skills demonstrated fully satisfy the NOS skill assessment criteria. The NGOFS2 has already been implemented as an operational OFS in March 2021.

1. INTRODUCTION

Coastal waters of the northern Gulf of Mexico (NGOM) encompass a broad coastal region spanning from the coast of Mexico in the west through the U.S. Gulf Coast in the northwest, north, and northeast of the Gulf of Mexico (Figure 1). The hydrodynamic state in the region is governed by fresh water inflows from river discharge, off shelf dynamics, wind forcing, heat flux across the air-sea interface, and by tidal fields (Etter et al., 1986; Morey et al., 2005; Sturges and Lugo-Fernandez, 2005; Westerink and Luettich, 1992; Longley, 1994; Zhang et al., 2012). The coastal circulation field is characterized by the combined seasonal buoyancy-driven coastal currents, as well as by intrusions onto the shelf of the Loop Current. Cross-shelf exchanges are driven by mixing or by episodic wind events, and by intrusions onto the shelf of the Loop Currents. River runoff onto the shelf is highly variable. Both the Atchafalaya River and the Mississippi River flow onto the Louisiana shelf with a combined annual average discharge of over 14,000 m^3/s (Dinnel and Wiseman, 1986). The major portion of this runoff flows westward onto the west Louisiana shelf and the remaining portion flows to the east onto the Louisiana-Mississippi-Alabama shelf. Both flows introduce buoyancy forcing, and largely define the baseline alongshore coastal current in the NGOM region.

Figure 1. Map of northern Gulf of Mexico. Blue and red lines combine to delineate the NGOFS2 model grid boundary. The red line represents the model's open ocean boundary.

The eastern and western NGOM, which are divided by the Mississippi River delta, demonstrate distinctive circulation features (Dinnel and Wiseman, 1986; Dzwonkowski and Park, 2012). A

large, semi-permanent, cyclonic surface gyre exists in the eastern NGOM (Longley, 1994; Elliott, 1982; Kelly, 1991). This gyre branches into two flows: a southeastern portion into a northward flow following the western rim of the DeSoto Canyon, and a southeastward flow along the Florida Shelf break. Both wind-driven currents and sea level fluctuations are strong in the winter when the eastern shelf is influenced by a series of cold fronts from the north. The Loop Current extrudes water onto the shelf in the DeSoto Canyon (Figure 1) and thus, directly modulates the local density and circulation fields.

Circulation in the western NGOM is influenced largely by river discharge induced buoyancy forcing and by the regional wind field (Zhang and Hetland, 2012; Zhang et al., 2012; Zhang et al., 2014; Wiseman et al., 1997). The combined effect of the buoyancy flux and the easterly wind stress produces a yearly mean westward coastal circulation along the Louisiana-Texas coast. The flow field is highly modulated by wind field fluctuations. Over the inner shelf, currents are predominantly modulated by winds in the weather band, while the outer shelf currents are driven primarily by mesoscale activity (DiMarco, 2000). Using the Regional Ocean Modeling System (ROMS), Zhang et al. (2014) studied the effects of wind forcing on the dynamics of buoyancy circulation over the Louisiana-Texas shelf. It was identified that in the winter and fall, under the impact of the prevailing easterly wind, most of the shelf water was dominated by a geostrophic balance in the cross-shore momentum budget. In the spring and summer, the Ekman flow, driven by strong onshore wind, played a major role in modulating the cross shore mass transport.

Tides in the NGOM region are modest (Westerink et al., 1992) with either diurnal or mixed characteristics. The mean tidal amplitude ranges from several centimeters to somewhat less than 50 cm. The strongest tidal currents are usually less than 15 cm/s. Using both mathematical analysis and one-dimensional water column numerical simulation, Burchard and Hetland (2010) quantified the impact of tidal straining on the circulation field of the region. They found that without wind forcing and river inflows, tidal straining is responsible for about two-thirds of the estuarine circulation, while gravitational circulation is responsible for the remaining one-third.

In addition to tidal dynamics, both inertial oscillations (Gough et al., 2016) and coastally trapped waves (Maksimova, 2016) add to the variability of the shelf circulation field. The inertial frequency is nearly diurnal at 30°N latitude which transects the northeastern Gulf of Mexico (NeGoM). At this latitude, near-surface inertial oscillations can amplify due to resonance with diurnal wind forcing.

The Gulf Coast is an area of active economic and recreational activities. Both the hydrographic and hydrodynamic states impart a significant impact on the local ecosystem and on daily human life. The operational hydrodynamic forecast is of vital importance in its support of marine navigation, emergency response, and the environmental management communities.

The National Oceanic and Atmospheric Administration (NOAA) currently has three operational oceanographic nowcast/forecast modeling systems (OFS) in the NGOM region. These three OFS are the Northern Gulf of Mexico OFS (NGOFS, operational in 2012), the nested northwestern Gulf of Mexico OFS (NWGOFS), and the nested northeastern OFS (NEGOFS) (https://tidesandcurrents.noaa.gov/ofs/ngofs/ngofs.html). Both NWGOFS and NEGOFS were made operational in 2014. These systems all use the Finite Volume Coastal Ocean Model (FVCOM) (Chen et al., 2003) as their core hydrodynamic model. Each OFS produces six-hour nowcast and up to 48-hour forecast guidance of water level, three-dimensional (3-D) current, water

temperature, and salinity. The three systems differ in their domain coverage, model grid resolution, and in their method of applying open ocean boundary forcing (Wei et al., 2014a, 2014b).

Figure 2(a) depicts the domain of each system. Table 1 lists the size and spatial resolution of each model grid. The NGOFS domain spans the northern Gulf of Mexico coastal shelf from South Padre Island, Texas, in the west, to west of Panama City, Florida, in the east. It lacks coverage of several alongshore estuaries and embayments, most notably to the south and to the northeast of Corpus Christi, and it does not resolve fine coastline features. NWGOFS and NEGOFS were developed in part to resolve the limitations of NGOFS. Both NWGOFS and NEGOFS have higher spatial resolution than NGOFS. NWGOFS covers Lake Charles, Sabine-Neches, Galveston, and Matagorda Bay, while NEGOFS covers Mobile Bay, Pascagoula, and the Gulfport area.

Figure 3 shows a diagram illustrating the conceptual structure, forcing data inputs, system operations, analysis, and the archive of model outputs. The CO-OPS implemented the OFS on the NOAA Weather Climate Operational Supercomputing System (WCOSS) which is operated by the National Centers for Environmental Prediction (NCEP) Central Operations (NCO). The system runs make use of forecast guidance from NCEP's North American Mesoscale (NAM) weather forecast modeling system for the atmospheric forcing, and the U.S. Geological Survey (USGS) river discharge for the river forcing. The water level, current, water salinity, and water temperature values used by NGOFS for open boundary conditions (OBC) are generated from NCEP's Global Real-Time Ocean Forecast system (G-RTOFS). The NEGOFS/NWGOFS OBC are taken from the NGOFS output via a one-way nesting approach [20]. The native formats of the forcing files are different from those required by the FVCOM. The OFS (NGOFS, NEGOFS, and NWGOFS) uses the Common Ocean Modeling Framework (COMF) (Zhang and Yang, 2014) software package to transform the data sets into Network Common Data Form (NetCDF) files with data structures conforming to FVCOM requirements. Using the NOS' Continuous Operational Real-Time Monitoring System (CORMS) (https://tidesandcurrents.noaa.gov/corms.html) and NCO's Big Brother monitoring system, the CO-OPS and NCO monitor and log the system operations on a 24x7 basis.

The three OFS produce six hours of nowcast, and up to 48 hours of forecast guidance for water levels and for three-dimensional currents, water temperature, and salinity four times a day at 03, 09, 15 and 21 UTC. Both the hourly field and the 6-minute station (at locations with available observed data) NetCDF outputs are archived and disseminated at the NOAA's National Centers for Environmental Information (NCEI) (https://www.ncei.noaa.gov/thredds/model/ngofs_catalog.

html). In addition, the COMF generates time series plots of station output (24 hour nowcast and 48 hour forecast) which includes water level, current, water temperature, salinity, and surface wind. These outputs are depicted in both contour and vector map plots. Additional graphics include the animation of water level, current, temperature, salinity, and surface wind. The graphics of the nowcasts and forecast guidance are available from the NOS/CO-OPS web site at (https://tidesandcurrents.noaa.gov/ofs/ngofs/ngofs.html). Maps of the latest forecast guidance are available from NOAA nowCOAST (nowcoast.noaa.gov) web mapping services and map viewer.

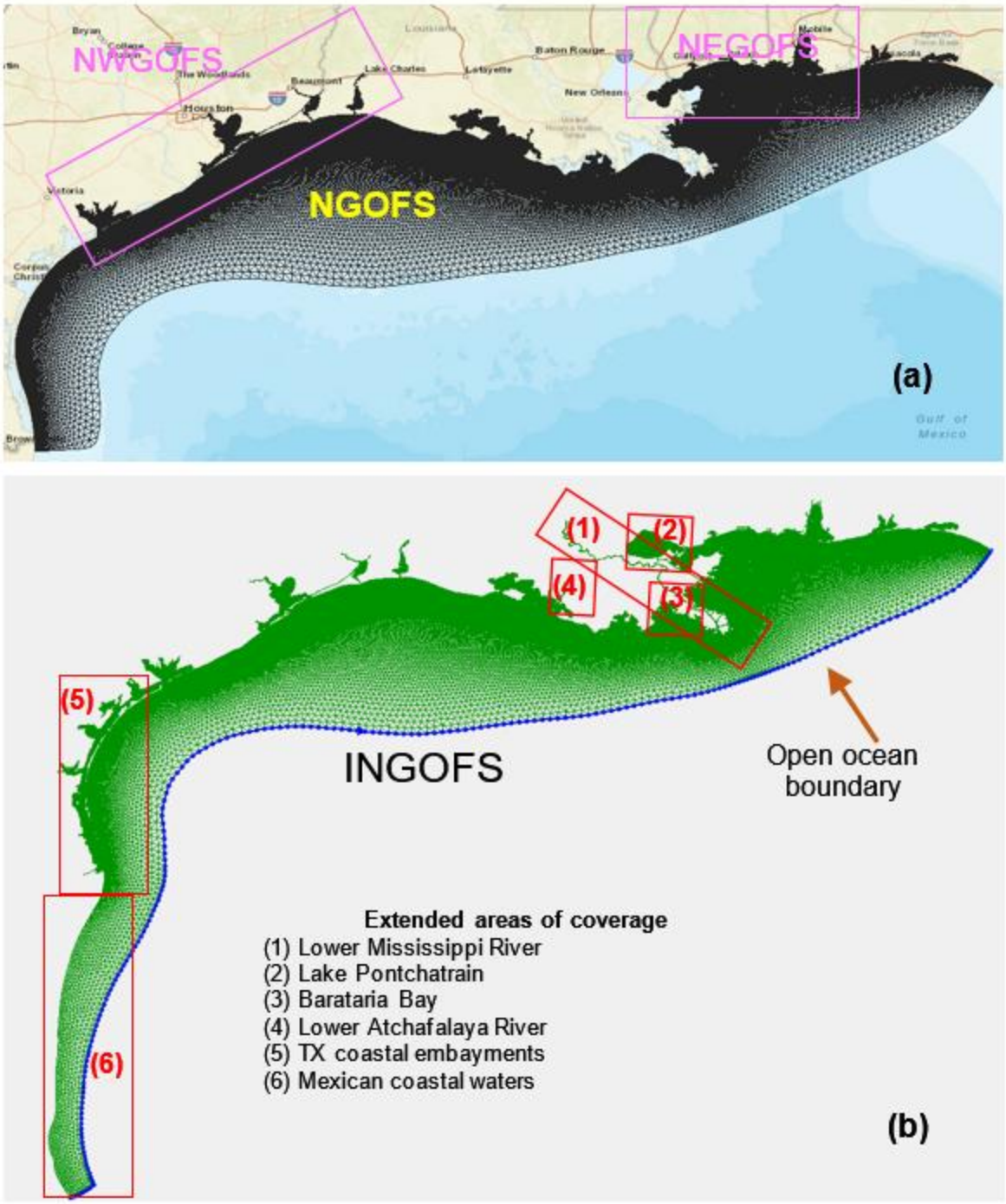

Figure 2. Model grids. (a) Combined grids of three existing OFS and (b) the NGOFS2 grid.

Table 1. Dimension and resolution of NGOFS, NWGOFS, NEGOFS, and NGOFS2 model grids.

Model	Number of Nodes	Number of Elements	Element Size (min, max)
NGOFS	90,267	174,474	(150 m-11 km)
NWGOFS	85,707	160,444	(60 m-3.5 km)
NEGOFS	68,455	131,008	(45 m-2.2 km)
NGOFS2	303,714	569,405	(45 m-11 km)

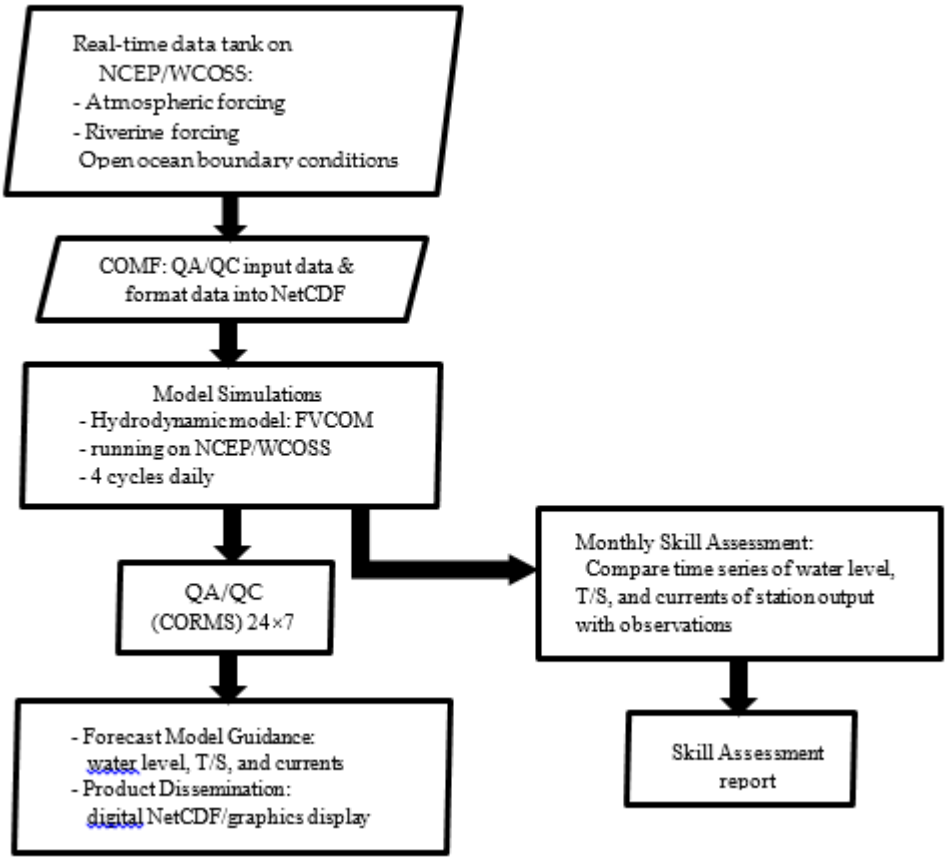

Figure 3. Conceptual structure and the operational and data analysis procedures of the NGOFS2.

In recent years, the Gulf Coast user community has expressed a growing need for forecast guidance in the NGOFS areas not covered by the three existing OFS. A short list of these areas includes the lower Mississippi River, Lake Pontchartrain, various Texas coastal embayments, and the coastal Gulf waters off the coast of northern Mexico (Figure 1). From an operational point of view, it is more efficient to operate and maintain one combined system, rather than three separate systems. To fulfill user needs and to foster the system's operational efficacy, NOAA decided to combine the three existing OFS into one integrated system. The domain of this new system includes the combined domains of the three existing OFS, as well as some previously unresolved coastal embayments and river courses. The upgraded system is named as the NGOFS2. Like NGOFS, NGOFS2 will use the FVCOM as its core hydrodynamic model. It is designed to produce a real-time nowcast, and up to 48 hours of forecast guidance for water levels, 3-D current, water temperature, and salinity. NGOFS2 became operational in March 2021. Meanwhile, NGOFS, NWGOFS, and NWGOFS were decommissioned.

This report describes technical details of the NGOFS2 development, model configurations, as well as setup and verification of hindcast simulations. This chapter introduced background information including the initiative for the system development. Chapter 2 describes the model hindcast simulation setup. Chapter 3 describes the observational data used to verify the hindcast results. Chapter 4 presents the model results. Chapter 5 discusses the domain-averaged model skill of the surface water temperature and water level, and the impact of the initial salinity condition on model performance. Chapter 6 presents the summary and future plan.

2. MODEL DEVELOPMENT

The NGOFS2 uses the Finite Volume Community Ocean Model (FVCOM) (Chen et al. 2003) as its core hydrodynamic model. The FVCOM is a three-dimensional, finite volume, primitive equation, ocean circulation model. It uses triangular grids to map the model domain in the horizontal and a terrain-following σ-coordinate in the vertical. The unstructured grid enables an accurate coastal geometric fit. FVCOM is a prognostic model; it is composed of internal and external modes which are computed separately using two split steps. The model uses a second-order finite-volume method to solve the equations of motion by the flux calculation in the integral form of the primitive equations.

The turbulence parameterization employs the modified Mellor and Yamada level-2.5 turbulence closure model (Mellor and Yamada, 1982) for vertical mixing. The Smagorinsky formulation (Smagorinsky, 1963) is used for horizontal mixing. FVCOM has been successfully applied to studies of the deep ocean (Zheng and Weisberg, 2012), the continental shelf (Chen et al., 2005), and estuaries (Zhao et al., 2006; Zheng et al., 2010). A detailed description of FVCOM is available at http://fvcom.smast.umassd.edu/FVCOM/index.html.

2.1. Model Domain and Grid

The NGOFS2 domain encompasses broad NGOM coastal waters spanning from the coast of Mexico, near (97.6 °W, 21.8 °N) in southwest, all the way across the U.S. Gulf Coast in the northwest, north, and northeast, extending to just west of Panama City in the east (Figures 1.1 and 1.2). The domain's open ocean boundary approximates the 300-m isobath except near the Mississippi river mouth, where the model boundary extends further offshore beyond the shelf break to a depth as deep as 1,700 m. The open ocean boundary for NOGFS and NGOFS2 is the same except for the inclusion of Mexican coastal waters in the NGOFS2 grid.

In addition to encompassing the combined NGOFS, NWGOFS, and NEGOFS domains, the NGOFS2 domain also includes the Lower Mississippi River course, Lake Pontchartrain, Barataria Bay, the lower Atchafalaya River, the Texas coastal embayments to the north of the Mexican border, and a portion of Mexican coastal waters (Figures 1 and 2). From the perspective of grid generation, the NGOFS2 grid is composed of two parts: the combined NGOFS, NWGOFS, and NEGOFS grids, and the newly generated grids for extended coverage. The former includes Lake Charles, Sabine-Neches, Galveston Bay, Matagorda Bay, Mobile Bay, Pascagoula, and Gulfport. Figures 1.2a and 1.2b show the combined NGOFS, NWGOFS/NEGOFS grid and the NGOFS2 grid, respectively. Figures 4a and 4b display zoomed in views of the grids covering the Texas coastal embayments and the lower Mississippi River and adjacent waters, respectively. The NGOFS2 grid is composed of 303,714 nodes and 569,405 elements. For the purpose of comparison, Table 1 lists the number of nodes, elements, and the spatial resolution for both the existing OFS grids and the NGOFS2 grid.

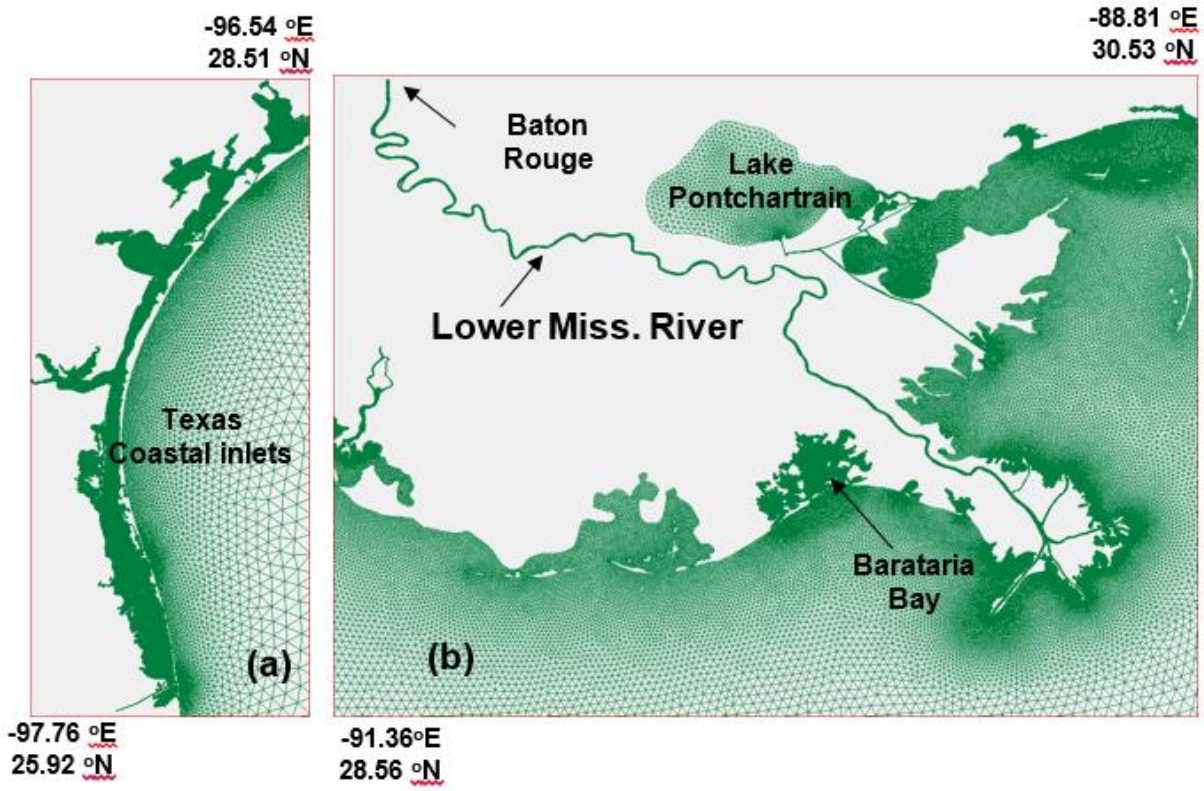

Figure 4. Close-up view of the NGOFS2 model grid in two regions: (a) Texas coastal embayments and (b) the lower Mississippi River course, Barataria Bay, and Lake Pontchartrain.

2.2. Model Grid Bathymetry

The NGOFS2 bathymetry (Figure 5) was populated using the NGOFS bathymetry, the NWGOFS/NEGOFS grid bathymetry, the Vertical Datum (VDatum) (https://vdatum.noaa.gov/welcome.html) model grid bathymetry (Yang et al., 2010), the NOAA Sounding and Electronic Chart (ENC) bathymetry (https://www.nauticalcharts.noaa.gov/ENCOnline/enconline.html), and the ADCIRC model grid bathymetry in the Western North Atlantic, Caribbean and Gulf of Mexico ADCIRC Tidal Database (EC2015) (Szpilka et al., 2016). Depending on sources of the NGOFS2 grid generation and the geographical location, bathymetry was populated in three ways. For any portion of the grid which originated from any of the three pre-existing OFS, the bathymetry remained the same as the bathymetry in the source grid. For the remaining portion of the grid in U. S. coastal waters, the bathymetry was populated by linearly interpolating the combined VDatum model grid for the Mississippi River and the New Orleans region (Yang et al., 2010) as well as the ENC bathymetry. Bathymetry of the grid covering Mexican waters was populated by linearly interpolating the EC2015 ADCIRC grid bathymetry.

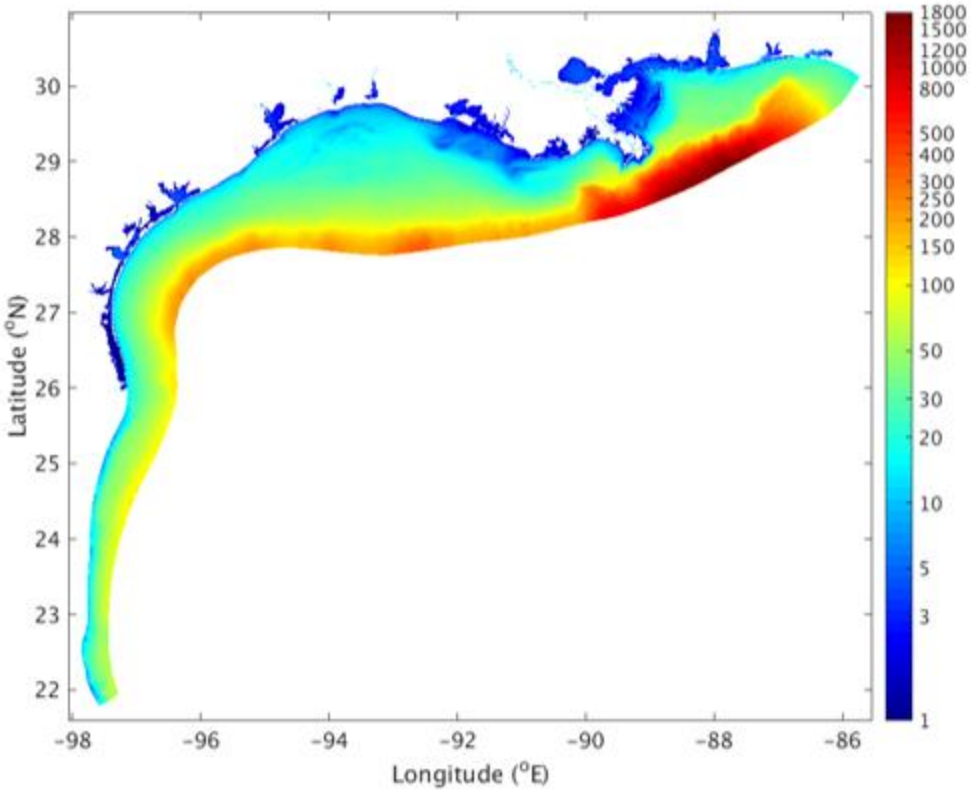

Figure 5. The NGOFS2 model grid bathymetry (meters).

2.3. Model Setup and Computation

Using the model grid (Figure 4) and bathymetry configuration (Figure 5), we conducted a one-year (August 2, 2016-August 1, 2017) hindcast simulation. The simulation was driven with the complete suite of model forcing data including open ocean boundary forcing of the combined tidal and subtidal water level and current. Additional model forcing included 3-dimensional temperature (T) and salinity (S), river flow, and sea-surface meteorological forcing. The tidal water level harmonics were interpolated using the EC2015 tidal database (Szpilka et al., 2016). Considering the relative importance of tidal constituents in the model domain, we chose eight major tidal constituents to reconstruct the tidal forcing data: luni-solar (K_1), principal lunar (O_1), principal solar (P_1), elliptical lunar (Q_1), principal lunar (M_2), principal solar (S_2), elliptical lunar (N_2), and luni-solar (K_2).

The non-tidal open ocean conditions made use of the nowcasts from the Global Real-Time Ocean Forecast System (G-RTOFS) (Mehra et al., 2015; Garaffo et al., 2016). The G-RTOFS is run by the National Weather Service (NWS) National Centers for Environmental Prediction (NCEP). G-RTOFS makes use of the Naval Oceanographic Office's configuration of the 1/12 eddy resolving global Hybrid Coordinates Ocean Model (HYCOM) as its core hydrodynamic model. It runs once a day and produces nowcast and forecast guidance for sea surface values of SSH, SST, and sea-surface salinity (SSS) at three-hour intervals. In addition, it produces full volume parameters (3-dimensional temperature, salinity, currents, and mixed layer depths) at six-hour intervals. The

nowcasts of three-hourly water levels and six-hourly 3-D currents, water temperature (T) and salinity (S) as the non-tidal forcing were spatially interpolated onto the model grid's open ocean boundaries and temporally interpolated throughout the NGOFS2 hindcast period.

The river forcing used discharge from 29 rivers along the NGOFS2 land boundary. Table 2 lists the USGS station identifications (IDs) and station names. Some big rivers, with wide cross sections, were resolved through multiple grid nodes. In such cases, river discharge was evenly distributed across the nodes. Discharge from the 29 rivers are distributed over a total of 63 model nodes. Figure 6 shows the river node locations.

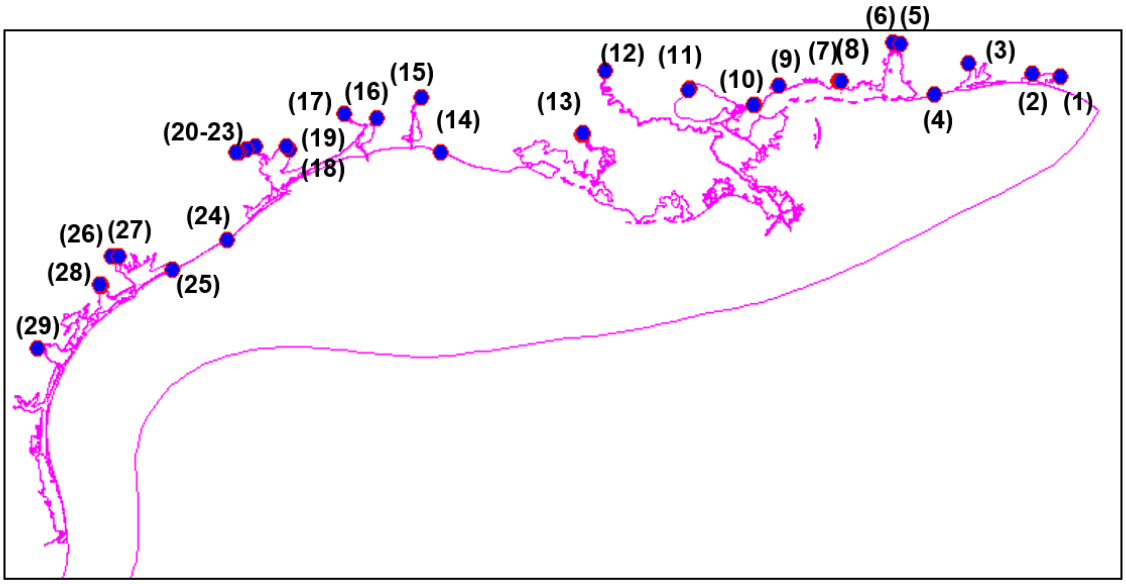

Figure 6. River forcing locations on the NGOFS2 grid. Discharges of the total 29 rivers are distributed across 63 grid nodes.

Table 2. USGS river station IDs and names.

No.	IDs	station names	No.	IDs	station names
1	2365500	Chocta Whatchee River at Caryville, FL	16	8015500	Calcasieu River Near Kinder, LA
2	2368000	Yellow River at Milligan, FL	17	8030500	Sabine Rv Nr Ruliff, TX
3	2375500	Escambia River Near Century, FL	18	8041780	Neches Rv Saltwater Barrier at Beaumont, TX
4	2376500	Perdido River at Barrineau Park, FL	19	8066500	Trinity Rv at Romayor, TX
5	2470629	Mobile River Near Landon, MS	20	8069000	Cypress Ck Nr Westfield, TX
6	2471019	Tensaw River Near Mount Vernon, AL	21	8075000	Brays Bayou at Houston, TX
7	2479000	Pascagoula River at Merrill, MS	22	8075400	Sims Bayou at Hiram Clarke St, Houston, TX
8	2479560	Escatawpa River Near Agricola, MS	23	8076000	Greens Bayou Nr Houston, TX
9	2481510	Wolf Rv Nr Landon, MS	24	8116650	Brazos Rv Nr Rosharon, TX
10	2489500	Pearl River Near Bogalusa, LA	25	8162500	Colorado Rv Nr Bay City, TX
11	2492000	Bogue Chitto River Near Bush, LA	26	8164000	Lavaca Rv Nr Edna, TX
12	7374000	Mississippi River at Baton Rouge, LA	27	8164800	Placedo Ck Nr Placedo, TX

13	7375500	Tangipahoa River at Robert, LA	28	8188800	Guadalupe Rv Nr Tivoli, TX
14	7381600	Lower atchafalaya River at Morgan City, LA	29	8211200	Nueces Rv at Bluntzer, TX
15	8012000	Nezpique Near Basile, LA			

The river flow data were from U.S. Geological Survey (USGS) river discharge observations (USGS, 2013). Note that not all USGS river discharge measurements were accompanied by simultaneous water temperature measurements. For the stations without temperature data, the temperature measurements from nearby Center for Operational Oceanographic Products and Services (CO-OPS) stations were used. The salinity was specified to be zero for all 29 rivers.

The hindcast made use of the 12-km resolution forecast guidance from the NCEP's North American Mesoscale (NAM) Forecast Modeling System for surface meteorological forcing. The NGOFS2 hindcast was forced with 10-m wind velocity to compute the surface wind stress, and with the mean sea level pressure, 2-m surface air temperature and relative humidity. Additional forcing included the total shortwave radiation, the downward longwave radiation, the FVCOM bulk formulation to calculate the air-sea momentum, and the Coupled Ocean–Atmosphere Response Experiment (COARE) algorithm (Cowels et al., 2008) to compute heat flux across the air-sea interface.

The hindcast simulation ran from August 2, 2016 to August 1, 2017. It started from a still water state with the water temperature and salinity fields initialized with the G-RTOFS output. The model was configured in 20 sigma layers. It used the FVCOM wetting and drying feature with a minimum depth of 0.5 m, the quadratic bottom friction scheme, and the two-equation model of the Mellor-Yamada Level 2.5 turbulence closure (Mellor and Yamada, 1982). The internal model time step was 9 seconds and the external to internal time step split ratio was equal to three.

3. OBSERVATIONAL DATA

The observational data used to verify the model results include time series of water level, currents, and surface water temperature and salinity. The water level data were collected at the National Ocean Service (NOS) CO-OPS water level stations (Section 3.1). The current data were collected by either the CO-OPS current stations (https://tidesandcurrents.noaa.gov/cdata/StationList?type=Current+Data&filter=historic) or the Texas Automated Buoy System (TABS) operated by the Texas A&M University (http://tabs.gerg.tamu.edu/) (Section 3.2). The water temperature (T) data were from either the CO-OPS meteorological observation stations or the National Data Buoy Center (NDBC) buoys (Section 3.3). The salinity (S) data were from the CO-OPS meteorological observation stations (Section 3.4).

3.1. Water Level

The water level data were downloaded via the CO-OPS online archive (CO-OPS, 2018). Table 3 lists the station IDs, names, and station location information. Figure 7 displays the station map.

Table 3. Station meta data of water level observations.

No.	IDs	station names	longitude (°E)	latitude (°N)
1	8735180	Dauphin Island	-88.075	30.25
2	8735391	Dog River Bridge	-88.088	30.5652
3	8735523	East Fowl River, Hwy 193 Bridge	-88.1139	30.4437
4	8741533	Pascagoula NOAA Lab, MS	-88.5667	30.3583
5	8747437	St. Louis Bayentrance	-89.3258	30.3264
6	8760721	Pilot Town	-89.2583	29.1783
7	8760922	Pilots Station E, SW Pass, LA	-89.4067	28.9317
8	8761305	Shell Beach, Lake Borgne	-89.6732	29.8681
9	8761724	East Point, Grand Isle	-89.9567	29.2633
10	8761927	New Canal USCG station, Lake Pontchartrain	-90.1134	30.0272
11	8762483	I-10 Bonnet Carre Floodway, TX	-90.39	30.0683
12	8764314	Eugene Island, North of Atchafalaya Bay	-91.3839	29.3675
13	8767961	Bulk Terminal	-93.3007	30.1903
14	8768094	Calcasieu Pass	-93.3429	29.7682
15	8770475	Port Arthur	-93.93	29.8667
16	8770570	Sabine Pass	-93.8701	29.7284
17	8770613	Morgans Point, Barbours Cut	-94.985	29.6817
18	8770808	High Island, ICWW	-94.3903	29.5947
19	8770822	Texas Point, Sabine Pass	-93.8418	29.6893
20	8770971	Rollover Pass	-94.5133	29.515
21	8771013	Eagle Point	-94.9183	29.48
22	8771341	Galveston Bay Entrance, TX	-94.7248	29.3573
23	8771450	GALVESTON, Galveston Channel	-94.7933	29.31
24	8771486	Galveston Railroad Bridge, TX	-94.8967	29.3017
25	8771972	San Luis Pass	-95.1133	29.095
26	8773259	Port Lavaca, TX	-96.6094	28.6403
27	8773701	Port O'Connor, Matagorda Bay	-96.3883	28.4517
28	8773767	Maragorda Bay Entrance Channel, TX	-96.3283	28.4267

29	8774513	Copano Bay, TX, TCOON	-97.0217	28.1183
30	8774770	Rockport, TX	-97.0467	28.0217
31	8775237	Port Aransas, TX	-97.0733	27.8383
32	8775296	USS Lexington,TX	-97.39	27.8117
33	8775792	Packery Channel	-97.2367	27.6333
34	8775870	Corpus Christi	-97.2167	27.58
35	8776139	S. BirdIsland, TX	-97.3217	27.48
36	8776604	Baffin Bay, TX	-97.405	27.295
37	8777812	Rincon Del San Jose, TX	-97.4917	26.825
38	8779748	South Padre Island, TX	-97.1767	26.0767
39	8779770	Port Isabel	-97.215	26.06
40	8778490	Port Mans Field, TX	-97.4217	26.555
41	8774230	Aransas Wildlife Refuge	-96.795	28.2283
42	8773037	Seadrift TCOON, TX	-96.7117	28.4083
43	8772447	USCG Freeport, TX	-95.3017	28.9433
44	8770777	Manchester, Houston Ship Channel	-95.2658	29.7263
45	8770733	Lynchburg Landing, San Jacinto River	-95.0783	29.765
46	8770520	Rainbow Bridge	-93.8817	29.98
47	8767816	Lake Charles	-93.2217	30.2236
48	8762075	Port Fourchon	-90.1993	29.1142
49	8741041	Dock E, Port of Pascagoula	-88.5054	30.3477
50	8739803	Bayou LaBatre Bridge	-88.2477	30.4057
51	8738043	West Fowl River, Hwy 188 bridge	-88.1586	30.3766
52	8737048	MOBILE, Mobile River, State Dock	-88.0433	30.7083
53	8736897	Coast Guard Sector Mobile	-88.0583	30.6483
54	8732828	Weeks Bay, AL	-87.825	30.4167
55	8729840	Pensacola	-87.2111	30.4044

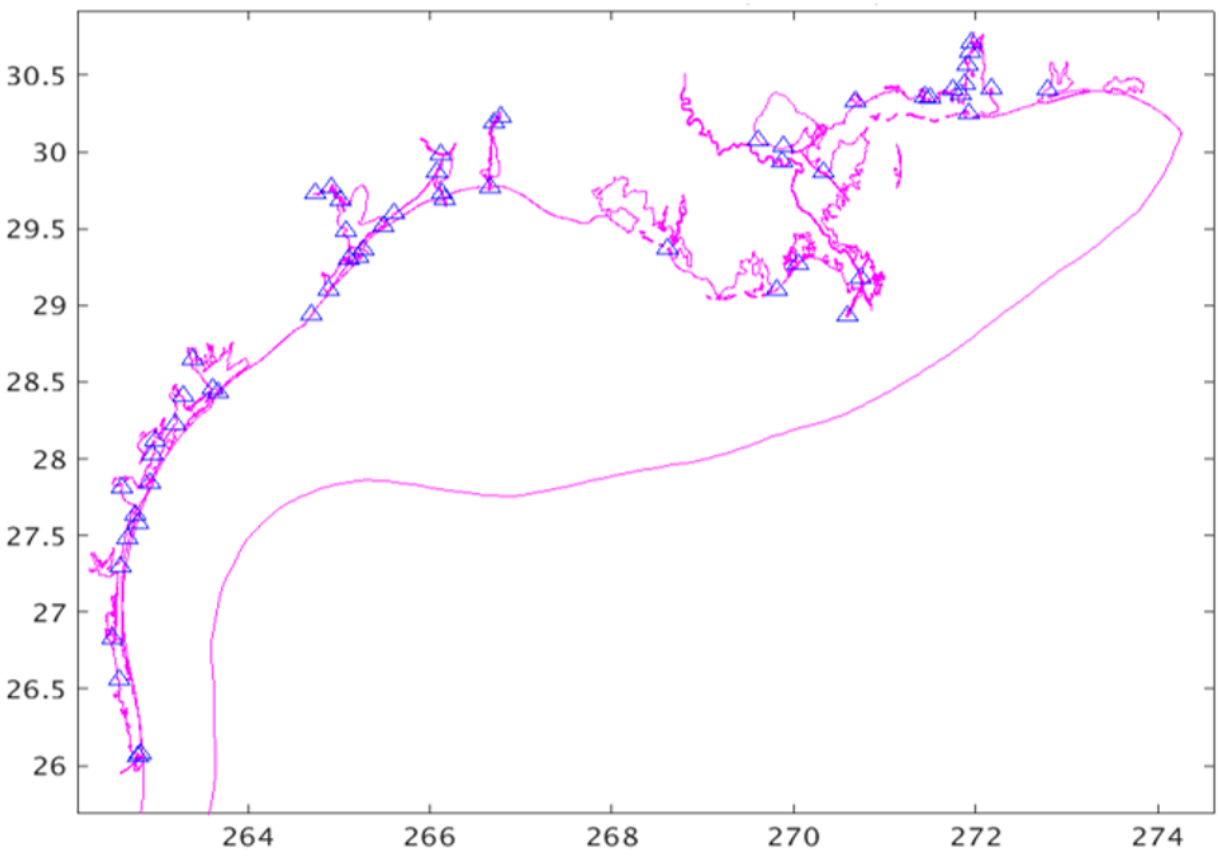

Figure 7. Map of water level stations (Table 3).

3.2. Current

The water current data are Acoustic Doppler Current Profiler (ADCP) measurements from CO-OPS CMIST buoys (Pruessner et al., 2007) and from TABS buoys. The CO-OPS data were downloaded from https://tidesandcurrents.noaa.gov/cdata/StationList?type=Current+Data&filter=historic, whereas the TABS buoy data were downloaded from the NDBC online archive (NDBC, 2018). Table 4 shows the station IDs, names, and geographical information for the stations. Figure 8 displays the station map. For TABS buoys, the measurement depth was about 2 m below the surface, while the measurement depth for CO-OPS stations was 4.57 m (15 feet) below the sea surface (Pruessner et al., 2007).

Table 4. Station meta data for observations of water currents

No.	IDs	Station names	longitude (°E)	latitude (°N)
1	g0601	Galves Ent, TX	-94.7433	29.3417
2	g0801	Fred Hartman Br., Houston Ship Channel, TX	-95.01892	29.7035
3	lc0101	Lake Calcas, LA	-93.3317	29.6933

4	lc0201	Cameron Fis, LA	-93.3433	29.7633
5	lm0201	Port Allen, Lower Mississippi River PORTS	-91.20056	30.43547
6	mb0401	MB Cont term, AL	-88.03167	30.665
7	mc0101	Atchafalaya Bar Channel, Morgan City PORTS, MS	-91.42967	29.318
8	mg0101	Matagorda Ship Channel Marker 19, Mgda PORTS	-96.35617	28.44769
9	ps0301	Pasc NG Pier, MS	-88.5633	30.36
10	sn0101	Sabine LBB 34, LA	-93.8067	29.63
11	sn0301	Sabine Front Range, Sabine Neches PORTS	-93.89	29.75806
12	sn0401	W Prt Arthur Bg, TX	-93.9633	29.8233
13	sn0501	Rainebow Bridge, TX	-93.87	29.98
14	sn0701	Port Arthur, TX	-93.9311	29.8671
15	TAB_B	TABS Buoy B, TX	-94.9183	28.9817
16	TAB_D	TABS Buoy D, TX	-96.8433	27.94
17	TAB_F	TABS Buoy F, TX	-94.2416	28.8433
18	TAB_J	TABS Buoy J, TX	-97.05	26.1917
19	TAB_K	TABS Buoy K, TX	-96.5	26.2167
20	TAB_N	TABS Buoy N, TX	-94.0367	27.89
21	TAB_R	TABS Buoy R, TX	-93.6417	29.635
22	TAB_V	TABS Buoy V, TX	-93.5967	27.8967
23	TAB_W	TABS Buoy W, TX	-96.005	28.35

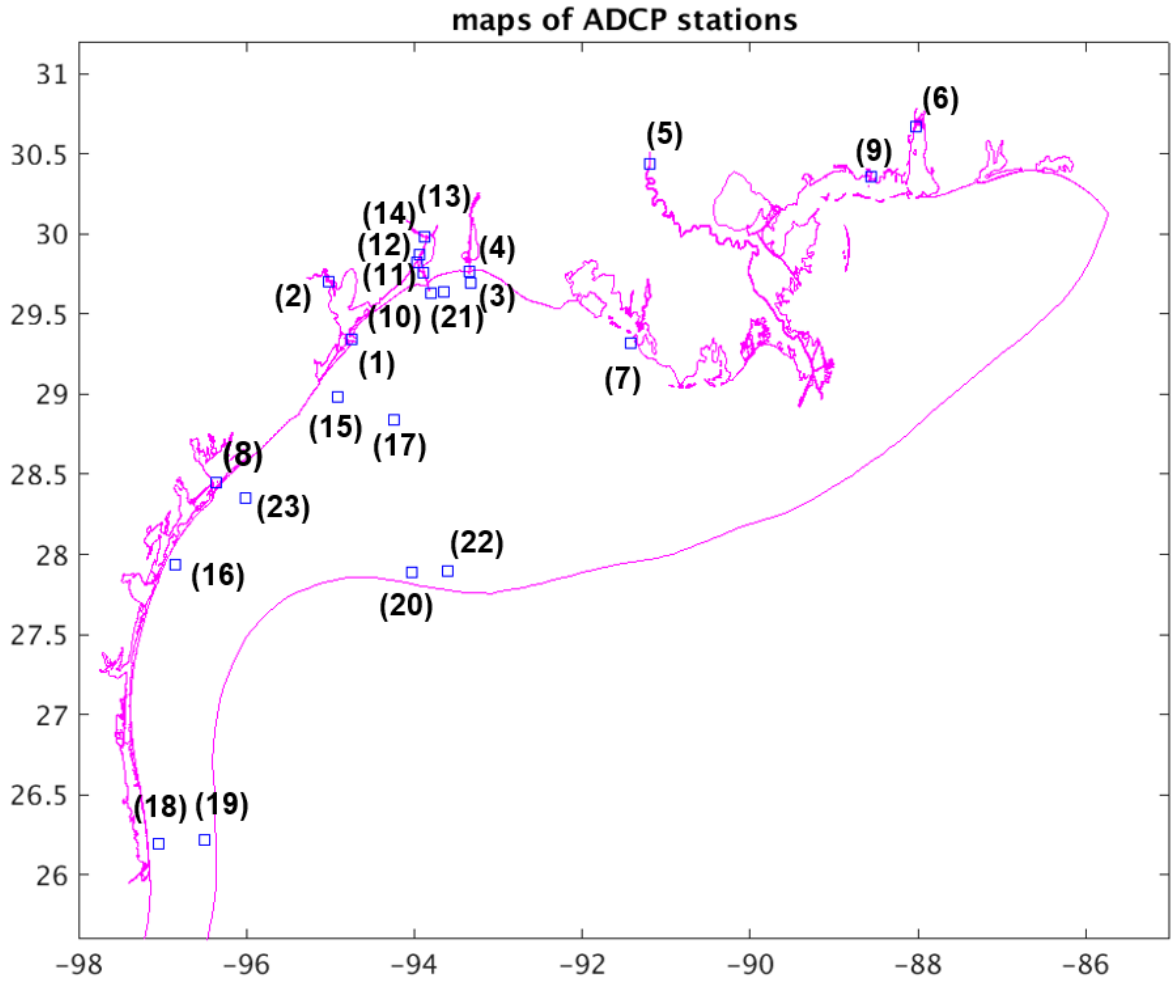

Figure 8. Map of the ADCP locations.

3.3. Sea-Surface Temperature and Salinity

The sea-surface temperature (SST) and salinity (S) data collected from either the CO-OPS or NDBC buoys were downloaded from the NDBC online archive (NDBC, 2018). Tables 5 and 6 show the station IDs, names, and geographical information for temperature and salinity, respectively. Figures 3.3 and 3.4 display the corresponding station maps of the temperature and salinity stations. The observation depth ranges between 0.5 m and 3 m beneath the sea surface. Note that every CO-OPS station possesses dual station IDs: one in the CO-OPS naming convention, and the other in the NDBC naming convention. To be clear, the stations are hereafter referred to only by their NDBC IDs.

Table 5. Station meta data of the SST observations

No.	IDs	station names	longitude (°E)	latitude (°N)
1	42012	44 NM SE of Mobile, Al	-87.555	30.065
2	42019	60 nm South of Freeport, TX	-95.353	27.913
3	42020	60 nm SSE of Corpus Christi, TX	-96.694	26.968
4	42035	22 nm East of Galveston, TX	-94.413	29.232
5	42040	64 NM South of Dauphin Island, Al	-88.207	29.212
6	42043	GA-252 TABS B	-94.919	28.982
7	42044	PS-1126 TABS J	-97.051	26.191
8	42045	PI-745 TABS K	-96.5	26.217
9	42046	HI-A595 TABS N	-94.037	27.89
10	42047	HI-A389 TABS V	-93.597	27.897
11	42067	USM3M02	-88.649	30.043
12	AMRL1	LAWMA, Amerada Pass, LA	-91.338	29.45
13	BABT2	Baffin Bay, TX	-97.405	27.297
14	BKTL1	Lake Charles Bulk Terminal, LA	-93.296	30.194
15	CAPL1	Calcasieu, La	-93.343	29.768
16	CARL1	Carrollton, LA	-90.135	29.933
17	EINL1	North of Eugene Island, LA	-91.384	29.373
18	EPTT2	Eagle Point, TX	-94.917	29.481
19	FCGT2	USCG Freeport, TX	-95.303	28.943
20	FRWL1	Fresh Water Canal Locks, La	-92.305	29.555
21	GISL1	Grand Isle, LA	-89.958	29.265
22	GNJT2	Galveston Bay Entrance (North Jetty), TX	-94.725	29.357
23	IRDT2	South Bird Island, TX	-97.322	27.48
24	LCLL1	Lake Charles, La	-93.222	30.223
25	MBET2	Matagorda Bay Entrance Channel, TX	-96.327	28.422
26	MCGA1	Coast Guard Sector Mobile, AL	-88.058	30.649
27	MGPT2	Morgans Point, TX	-94.985	29.682
28	MQTT2	Bob Hall Pier, Corpus Christi, Tx	-97.217	27.58
29	NUET2	Nueces Bay, TX	-97.486	27.832
30	NWCL1	New Canal Station, LA	-90.113	30.027
31	OBLA1	Mobile State Docks, AL	-88.04	30.705
32	PACT2	Packery Channel, TX	-97.237	27.634
33	PCBF1	Panama City Beach, FL	-85.88	30.213
34	PCLF1	Pensacola, FL	-87.212	30.403
35	PILL1	Pilottown, LA	-89.259	29.179
36	PMNT2	Port Mansfield, TX	-97.424	26.559
37	PNLM6	Pascagoula NOAA Lab, MS	-88.567	30.358
38	PORT2	Port Arthur, TX	-93.93	29.867
39	PTAT2	Port Aransas, TX	-97.05	27.828
40	PTIT2	Port Isabelle, TX	-97.215	26.06
41	RCPT2	Rockport, TX	-97.048	28.024
42	RLIT2	Realitos Peninsula, TX	-97.285	26.262
43	RSJT2	Rincon del San Jose, TX	-97.471	26.801
44	RTAT2	Port Aransas, TX	-97.073	27.84
45	SBPT2	Sabine Pass North, TX	-93.87	29.73
46	SDRT2	Seadrift, TX	-96.712	28.407
47	SHBL1	Shell Beach, LA	-89.673	29.868
48	TESL1	Tesoro Marine Terminal, Berwick, Atchafalaya River, LA	-91.237	29.668

49	TXPT2	Texas Point, Sabine Pass, TX	-93.842	29.689
50	ULAM6	Dock East Port of Pascagoula, MS	-88.505	30.348
51	VCAT2	Port Lavaca, TX	-96.595	28.64
52	WBYA1	Weeks Bay, Mobile Bay, AL	-87.825	30.417

Table 6. Station meta data of surface salinity observations

No.	IDs	Station names	longitude (°E)	latitude (°N)
1	42067	USM3M02	-88.649	30.043
2	BSCA1	Bon Secour, AL	-87.829	30.329
3	CRTA1	Cedar Point, AL	-88.14	30.308
4	PHA1	Dauphin Island, AL (1 psu)	-88.078	30.251
5	KATA1	Katrina Cut, Al	-88.213	30.258
6	BLA1	Middle Bay Lighthouse, AL	-88.011	30.437
7	HPA1	Meaher Park, AL	-87.936	30.667

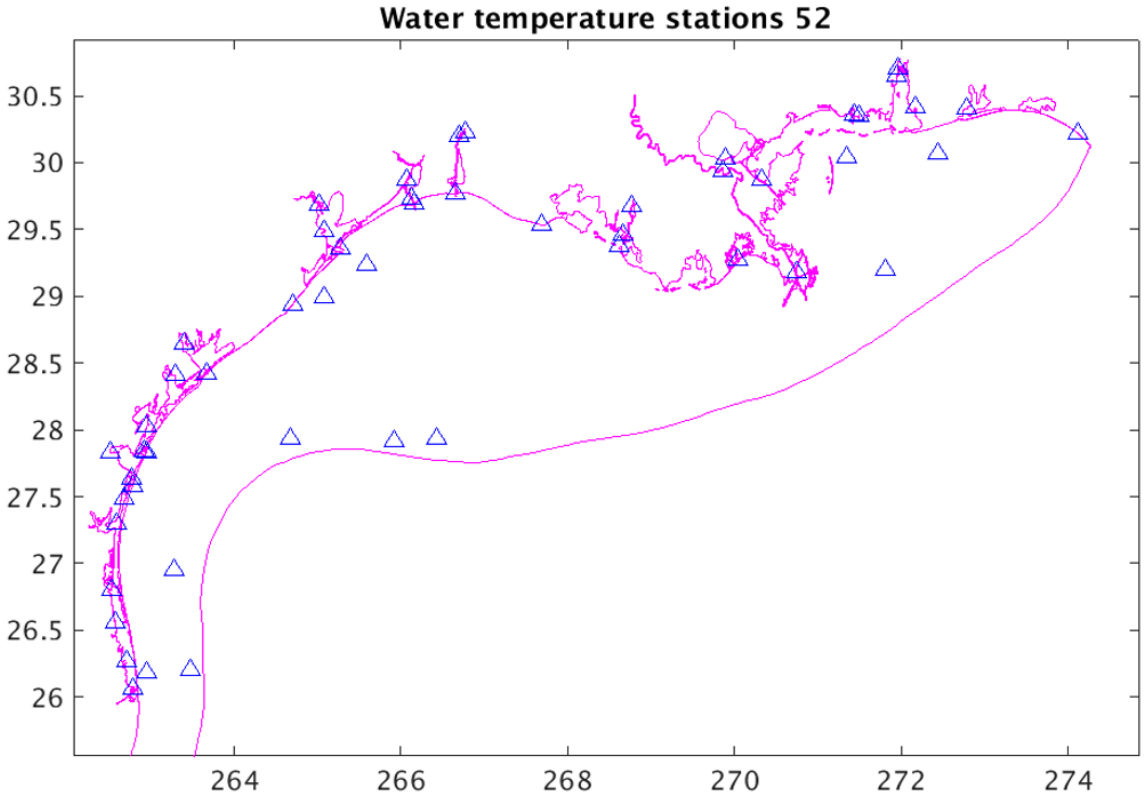

Figure 9. Map of water temperature stations.

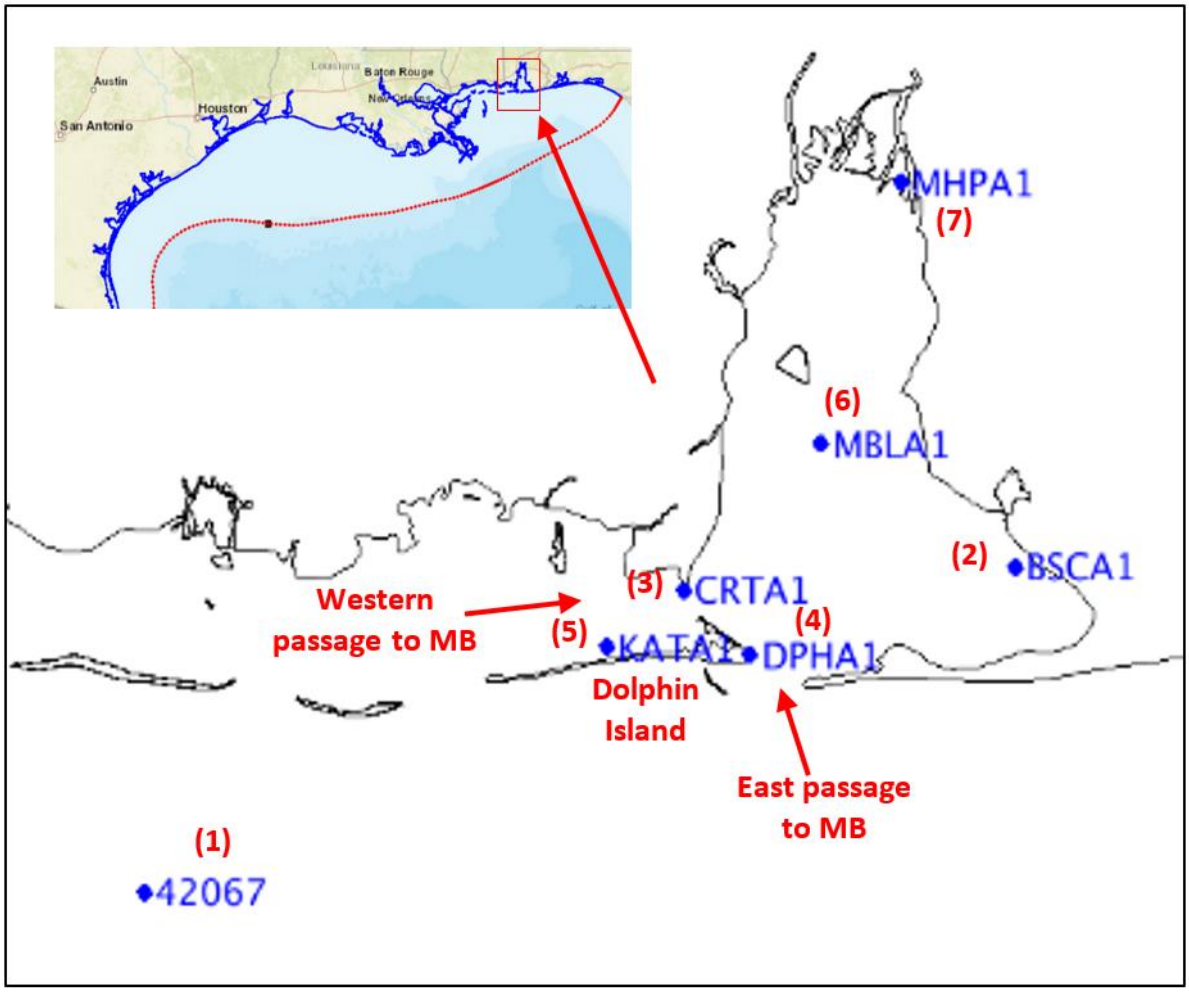

Figure 10. Map of salinity stations.

4. CONSTANT DENSITY TIDAL SIMULATION

4.1. Model Configuration

The constant density tidal only simulation was forced with tidal water level time series along the model grid open ocean boundary (see Chapter 2). The time series was generated using the tidal harmonic constants of the Western North Atlantic, Caribbean, and Gulf of Mexico ADCIRC Tidal Database (EC2015) (Szpilka etc., 2015). See the first paragraph of Section 2.3 for details. The harmonic constants of each constituent were interpolated onto the grid nodes of the NGOFS2 open ocean boundary. Both the magnitude of tidal amplitude and the phase were adjusted to optimize the model-data agreement at 100 water level stations (Table 7). The adjustments were made through a trial-and-error procedure. Multiple model runs were conducted; the results from each run were compared with observed data. Tidal harmonic constants on the model's open ocean boundary were adjusted accordingly to optimize the model-data agreement. It is noted that in principle, with a tidal model, this procedure can be repeated until a perfect fit is achieved. However, this will not necessarily guarantee an improvement on average across the domain. Table 7 lists the station IDs, names, longitudes (^{o}E), and latitudes (^{o}N) of the 100 stations.

To evaluate the model setup, a 200-day tidal simulation was conducted beginning from the still water state. We discarded the model output from the first 15 days (the time required to spin-up and reach the equilibrium state) and analyzed the water level time series for the remaining six months (185 days). The results are presented in the following sections.

4.2. Results

Co-tidal and Co-range Fields Figures 11 and 12 show the co-tidal and co-range fields of the four most prominent tidal constituents: K_1, O_1, P_1, and M_2. For all four constituents, the spatial pattern and magnitude of both the co-tidal and co-range fields demonstrate favorable agreement with those demonstrated in the ADCIRC tidal database (Szpilka etc., 2015).

The fields, both for amplitude and for phase, exhibit significant spatial variability throughout the model domain. Spatial variability is especially evident for the principal lunar constituent, M_2. All four constituents exhibit intensified amplitudes along the coast areas adjacent to Galveston Bay, Sabine Lake, and Calcasieu Lake. This effect is most visible along the coastline east of Galveston Bay, where the coastline exhibits a concave shape. Due to this specific feature, tidal energy converges and produces enhanced tidal amplitudes. In general, tides in the northeastern domain are weaker than those in the southwestern domain. The tidal intensity appears to be the weakest (less than 4 cm) in the Texan coastal embayments and in Lake Pontchartrain.

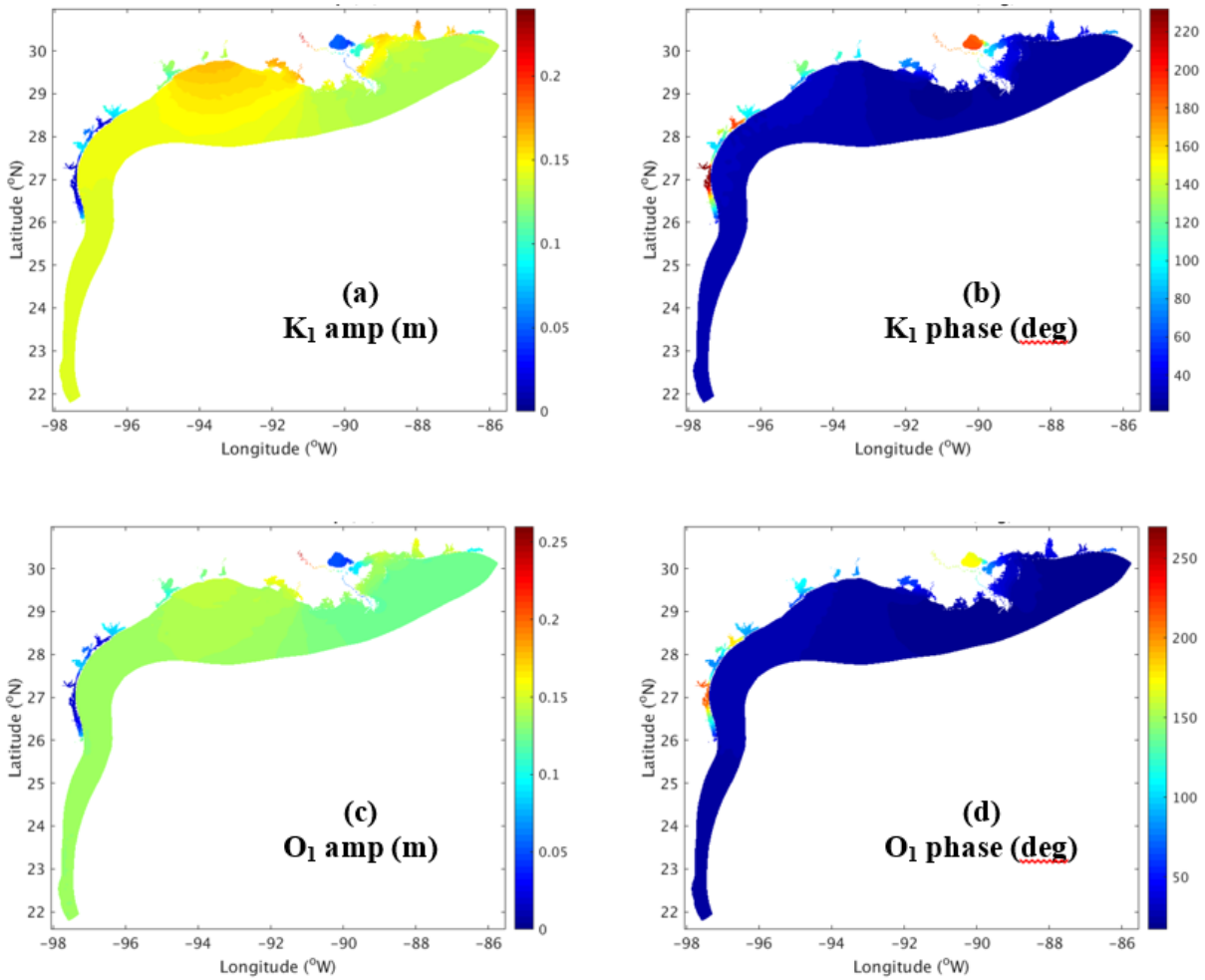

Figure 11. Modeled co-amplitude and co-phase fields of K_1 and O_1.

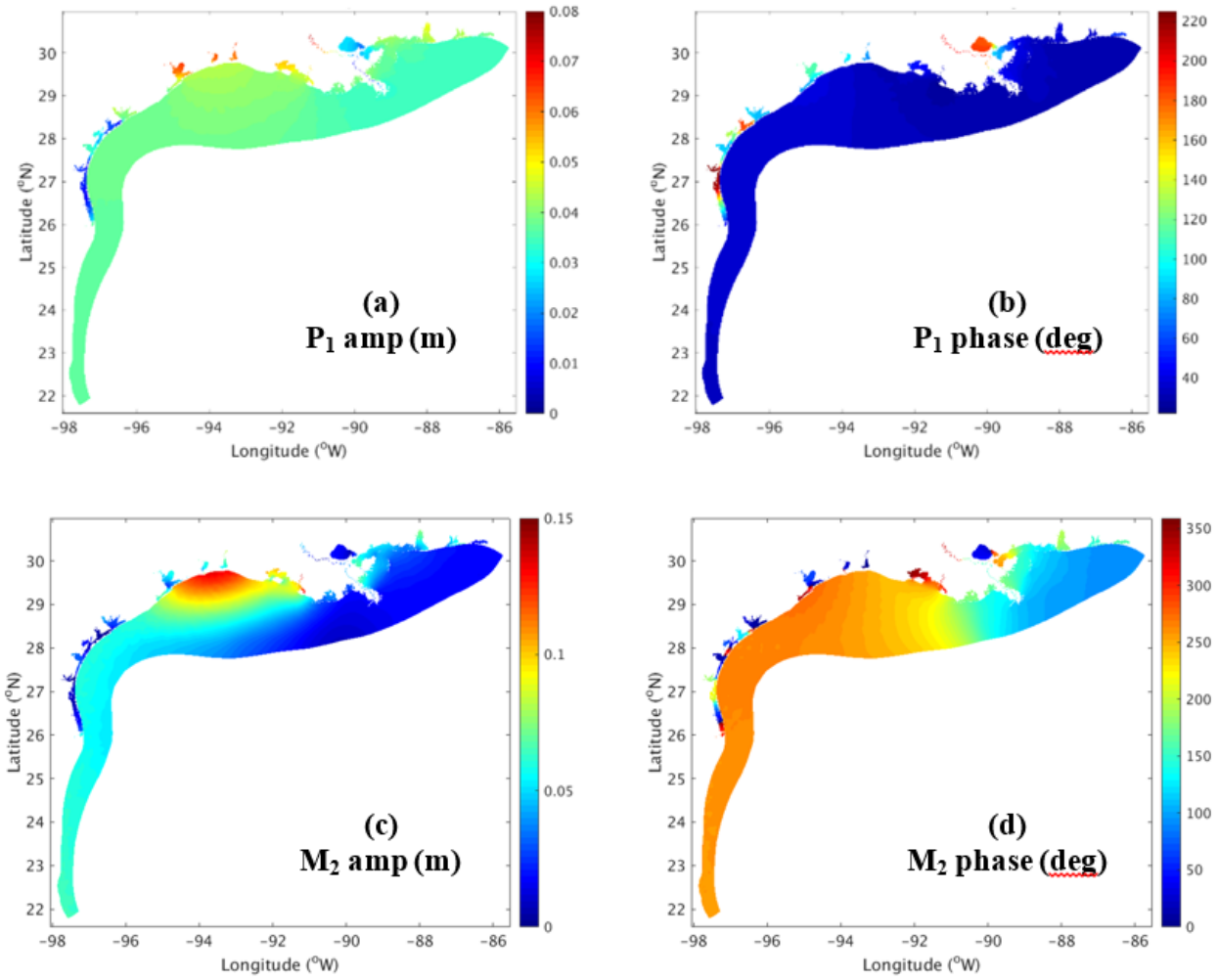

Figure 12. Modeled co-amplitude and co-phase fields of P_1 and M_2.

Model-data Comparison To illustrate model skill, Figure 13 shows scatter plots of the model-data amplitudes (plots (a), (c), (e) and (g)) and phases (plots (b), (d), (f), and (h)) of the four most prominent constituents, K_1, O_1, P_1, and M_2 at 100 stations (Table 7).

Over the 100 stations, the average of the absolute model-data difference of the tidal amplitude are 1.5, 1.5, 1.1, and 1.76 cm for K_1, O_1, P_1, and M_2, respectively. The corresponding quantities for tide phase are 10.4, 9.5, 15.0, 20.8 degrees, respectively. Figures 13 and 14 show scatter plots (model results vs. observations for both amplitude and phase) of the tidal harmonic constants of the K_1, O_1, P_1, and M_2 constituents. The red lines on each plot outline the ten percent deviation from the perfect model-data match.

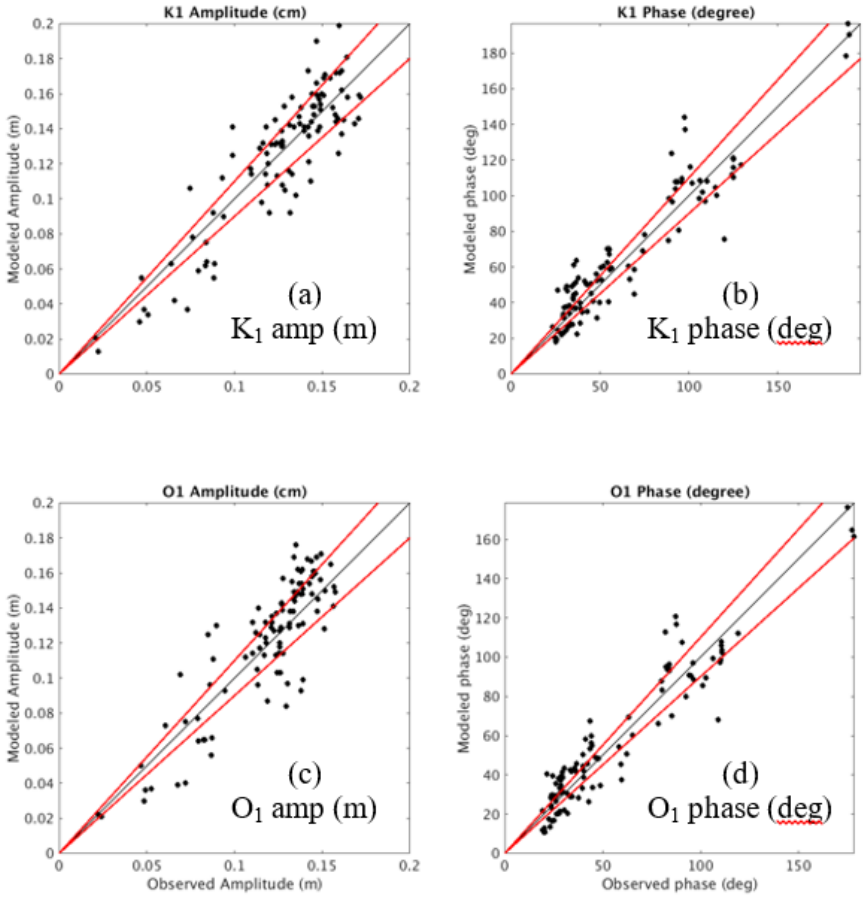

Figure 13. Scatter plots (model results vs. observations for both amplitude and phase) of the tidal harmonic constants of the K_1 and O_1 constituents. The red lines on each plot outline the ten percent deviation from the perfect model-data match.

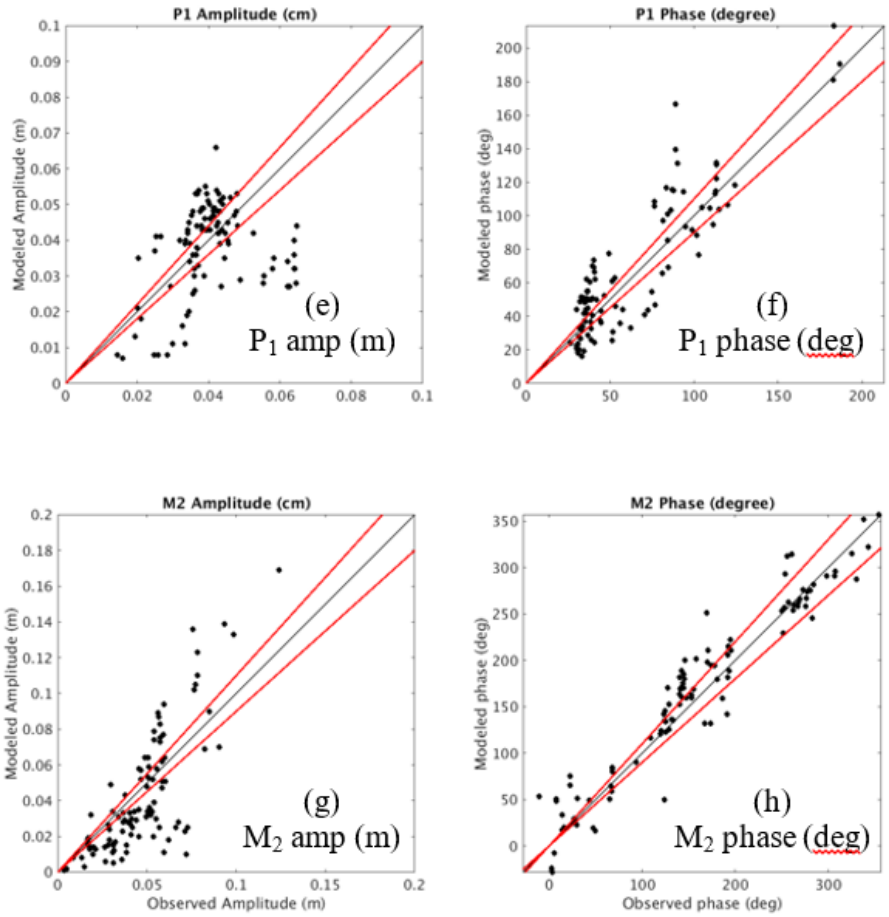

Figure 14. Scatter plots (model results vs. observations for both amplitude and phase) of the tidal harmonic constants of the P_1 and M_2 constituents. The red lines on each plot outline the ten percent deviation from the perfect model-data match.

We compared the model water level time series with tidal predictions. The predicted water levels were reconstructed using harmonic constants that were retrieved from the NOS/CO-OPS database (https://tidesandcurrents.noaa.gov/stations.html?type=Harmonic+Constituents).

Figures 15(a) and 15(b) display the color coded RMSE and CF maps, respectively, from running the skill assessment. Both RMSE and CF are nearly evenly distributed throughout the model domain. The RMSE ranges from 1.6 cm to 7.3 cm and the CF ranges from 95.8% to 100 %. This indicates that the model performance was uniform across the domain.

The average RMSE over the 100 stations equals 3.6 cm with a standard deviation of 1.3 cm. The average CF equals 99.7% with the standard deviation of 0.68%.

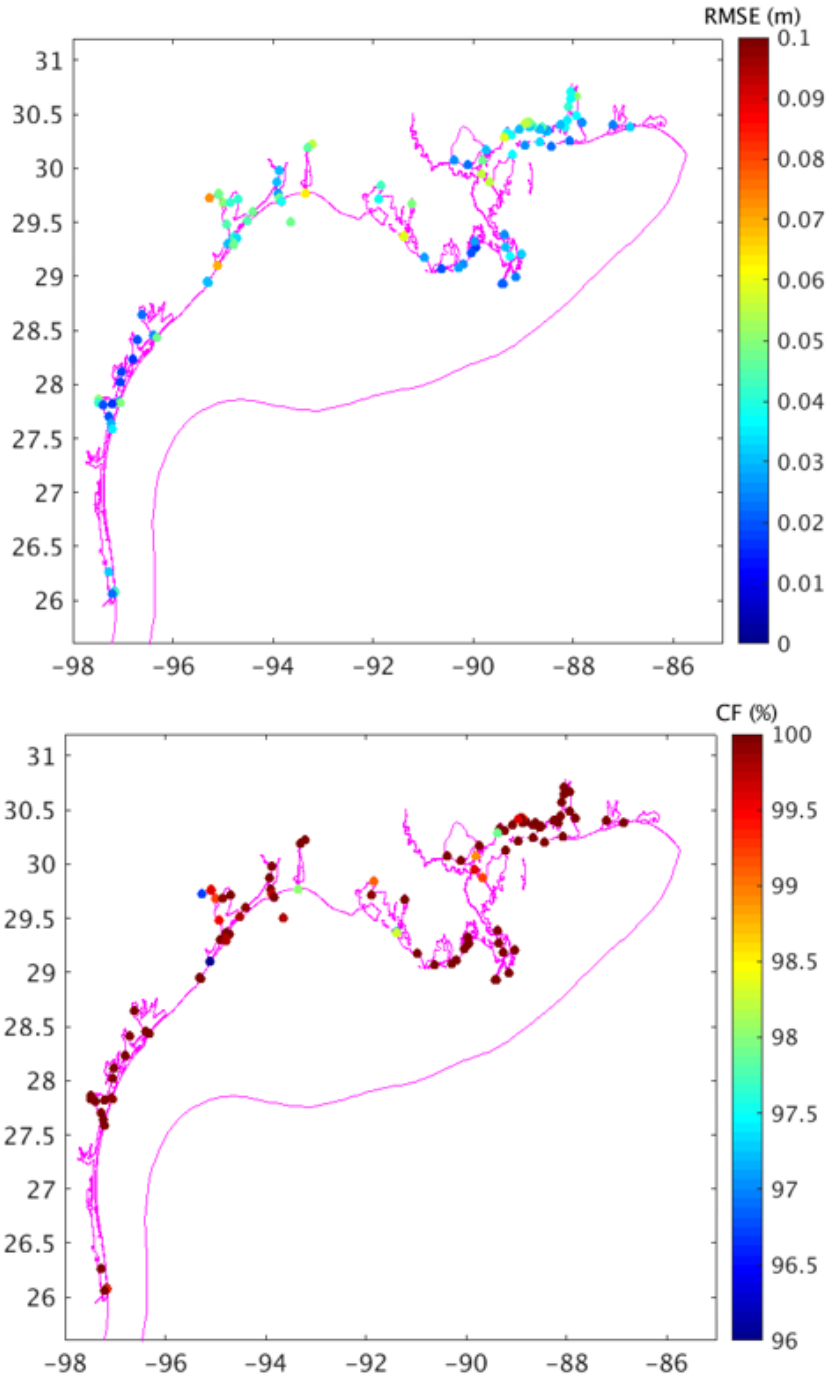

Figure 15. The RMSE and CF of the modeled tidal water levels at 100 CO-OPS stations (Table 7).

Table 7. Stations for Tidal Validation

No.	IDs	Station Names	Longitude (ºE)	Latitude (ºN)
1	8729678	"NavarreBeach"	-86.865	30.3767
2	8729840	"PENSACOLA"	-87.2111	30.4044
3	8732828	"WeeksBay,AL"	-87.825	30.4167
4	8733821	"PointClear,MobileBay"	-87.9345	30.4866
5	8733839	"MeaherStatePark,MobileBay"	-87.9364	30.6672
6	8735180	"DAUPHINISLAND"	-88.075	30.25
7	8735181	"DauphinIslandHydro,AL"	-88.08	30.2517
8	8735391	"DogRiverBridge"	-88.088	30.5652
9	8735523	"EastFowlRiver,Hwy193Bridge"	-88.1139	30.4437
10	8736897	"CoastGuardSectorMobile"	-88.0583	30.6483
11	8737048	"MOBILE,MobileRiver(StateDock)"	-88.0433	30.7083
12	8738043	"WestFowlRiver,Hwy188bridge"	-88.1586	30.3766
13	8739803	"BayouLaBatreBridge"	-88.2477	30.4057
14	8740405	"PetitBoisIsland,MississippiSound"	-88.4417	30.2033
15	8741041	"DockE,PortofPascagoula"	-88.5054	30.3477
16	8741196	"Pascagoula,MississippiSound"	-88.5333	30.34
17	8741533	"PascagoulaNOAALab,MS"	-88.5667	30.3583
18	8741798	"Gautier,MS"	-88.61	30.3833
19	8742205	"GravelineBayouEntrance"	-88.6633	30.3617
20	8742221	"HornIsland,MississippiSound"	-88.6667	30.2383
21	8743281	"OceanSprings,MS"	-88.7983	30.3917
22	8743735	"Biloxi(CadetPoint),BiloxiBay"	-88.8567	30.39
23	8743812	"DeerIsland,MS"	-88.8667	30.3833
24	8743838	"LangleyPoint,MS"	-88.87	30.425
25	8744117	"Biloxi,MS"	-88.9033	30.4117
26	8744284	"KEESLERAFB,BACKBAYOFBILOXI,MS"	-88.925	30.4183
27	8744671	"POPPSFERRY,BACKBAYOFBILOXI,MS"	-88.975	30.4133
28	8744756	"ShipIsland,MississippiSound"	-88.9717	30.2133
29	8745557	"GulfportHarbor,MississippiSound"	-89.0817	30.36
30	8746819	"PassChristianYachtClub,MississippiSound"	-89.245	30.31
31	8747437	"St.LouisBayentrance"	-89.3258	30.3264
32	8747766	"Waveland"	-89.3667	30.2817
33	8760417	"DevonEnergyFacility,LA"	-89.04	29.2
34	8760551	"SOUTHPASS"	-89.14	28.99
35	8760668	"GrandPass"	-89.2217	30.1267
36	8760721	"Pilottown"	-89.2583	29.1783
37	8760849	"Venice,GrandPass"	-89.3517	29.2733
38	8760889	"GrandBay"	-89.3801	29.3866
39	8760922	"PilotsStationE,SWPass,LA"	-89.4067	28.9317
40	8760943	"SWPass,LA"	-89.4183	28.925
41	8761305	"ShellBeach,LakeBorgne"	-89.6732	29.8681
42	8761385	"VICINITYOFUNOCHEFMENTEUR,LA"	-89.8017	30.0683
43	8761402	"TheRigolets,U.S.Highway90"	-89.7367	30.1667
44	8761529	"MARTELLOCASTLE,LAKEBORGNE,LA"	-89.835	29.945
45	8761720	"GRANDISLE,LA"	-89.9683	29.255
46	8761724	"EASTPOINT,GRANDISLE"	-89.9567	29.2633
47	8761742	"MENDICANTISLAND,BARATARIABAY,LA"	-89.98	29.3183
48	8761826	"CaminadaPass(bridge)"	-90.04	29.21

49	8761927	"NewCanalUSCGstation,LakePontchartrain"	-90.1134	30.0272
50	8762223	"EastTimbalierIsland,TimbalierBay"	-90.285	29.0767
51	8762888	"E.ISLEDERNIERES,LAKEPELTO"	-90.64	29.0717
52	8763535	"TexasGasPlatform,CaillouBay"	-90.9764	29.1748
53	8764044	"Berwick,AtchafalayaRiver,LA"	-91.2367	29.6683
54	8764311	"EugeneIsland,LA"	-91.385	29.3717
55	8764314	"EugeneIsland,Northof,AtchafalayaBay"	-91.3839	29.3675
56	8765251	"CypremortPoint"	-91.88	29.7134
57	8767816	"LakeCharles"	-93.2217	30.2236
58	8767961	"BulkTerminal"	-93.3007	30.1903
59	8768094	"CalcasieuPass"	-93.3429	29.7682
60	8770475	"PortArthur"	-93.93	29.8667
61	8770520	"RainbowBridge"	-93.8817	29.98
62	8770539	"MesquitePoint,TX"	-93.895	29.7667
63	8770559	"RoundPoint,TrinityBay"	-94.69	29.7133
64	8770570	"SabinePass"	-93.8701	29.7284
65	8770613	"MorgansPoint,BarboursCut"	-94.985	29.6817
66	8770625	"UmbrellaPoint,TrinityBay"	-94.8683	29.68
67	8770733	"LynchburgLanding,SanJacintoRiver"	-95.0783	29.765
68	8770743	"BattleshipTexasStatePark,TX"	-95.09	29.7567
69	8770777	"Manchester,HoustonShipChannel"	-95.2658	29.7263
70	8770808	"HighIsland,ICWW"	-94.3903	29.5947
71	8770822	"TexasPoint,SabinePass"	-93.8418	29.6893
72	8770971	"RolloverPass"	-94.5133	29.515
73	8771013	"EaglePoint"	-94.9183	29.48
74	8771081	"SabineOffshore,TX"	-93.64	29.4983
75	8771328	"PortBolivar"	-94.78	29.365
76	8771341	""(58):"GalvestonBayEntrance,TX""	-94.7248	29.3573
77	8771450	"GALVESTON,GalvestonChannel"	-94.7933	29.31
78	8771486	"GalvestonRailroadBridge,TX"	-94.8967	29.3017
79	8771510	"GalvestonPleasurePier"	-94.7894	29.2853
80	8771972	"SanLuisPass"	-95.1133	29.095
81	8773037	"Seadrift(TCOON),TX"	-96.7117	28.4083
82	8773259	"PortLavaca,TX"	-96.6094	28.6403
83	8773701	"PORTO'CONNOR,MATAGORDABAY"	-96.3883	28.4517
84	8773767	"MaragordaBayEntranceChannel,TX"	-96.3283	28.4267
85	8774230	"AransasWildlifeRefuge"	-96.795	28.2283
86	8774513	"CopanoBay(TCOON),TX"	-97.0217	28.1183
87	8774770	"Rockport,TX"	-97.0467	28.0217
88	8775188	"WhitePoint,TX"	-97.475	27.8583
89	8775237	"PortAransas,TX"	-97.0733	27.8383
90	8775244	"NuecesBay"	-97.4859	27.8328
91	8775270	"PortAransas(H.CaldwellPier)"	-97.05	27.8267
92	8775283	"PortIngleside(TCOON),TX"	-97.2033	27.8217
93	8775296	"USSLexington,TX"	-97.39	27.8117
94	8775421	"NavalAirStation,TX"	-97.28	27.705
95	8775792	"PackeryChannel"	-97.2367	27.6333
96	8775870	"CorpusChristi"	-97.2167	27.58
97	8779280	"RealitosPeninsula(TCOON),TX"	-97.285	26.2617
98	8779748	"SouthPadreIsland,TX"	-97.1767	26.0767
99	8779750	"PADREISLAND(southend)"	-97.1567	26.0683
100	8779770	"PortIsabel"	-97.215	26.06

5. SYNOPTIC HINDCAST SIMULATIONS

This chapter describes the skill assessment results of the hindcast simulation, using the full suite of forcings including tides, rivers, winds, and head-fluxes. The simulation spans a one-year period from 2 August 2016 to 1 August 2017. It started from a still water state with the temperature (T) and salinity (S) fields initialized with the G-RTOFS nowcast output. Following an initial 6-day ramping up period, the model run continued for another 9 days to ensure that a quasi-equilibrium state was reached. The time series of various ocean state variables including water level, currents, and T/S were recorded at 6-minute intervals from the 16th day to the end of the hindcast period. The time series then underwent skill assessment using the NOS standard skill assessment software (Zhang et al, 2006).

The model time series of water level, currents, temperature, and salinity were compared with the observed data (Chapter 2). The resulting values for the two key model skill parameters, RMSE and CF, are discussed in the following. The present skill assessment results demonstrate that in general the hindcast performance meets the above criteria.

5.1. Water Levels

The model and observed water level time series at 55 NOS/CO-OPS stations (Table 3) were compared.

5.1.1 Time Series

Figures 16-19 show both the model hindcast (red lines) and the observed (blue lines) total water level time series at 16 stations. Stations 8773259, 8775296, 8777812, and 8778490 (Figure 16) are located in the Texas coastal embayments. Stations 8767961, 8770520, 8770777, and 8770808 (Figure 17) are located in Galveston Bay, Sabine Lake, and Calcasieu Lake, respectively. Stations 8761955, 8760721, 8762075, and 8760922 (Figure 18) are located in the Lower Mississippi River and in the adjacent waters. Stations 8737048, 8741533, 8735180, and 8729840 (Figure 19) are located in Mobile Bay and the adjacent waters. For clarity of display, about 10 months (mid-September 2016 through mid-July, 2017) of the entire one-year comparison are displayed. The reference level is the MSL at each station. The model and data exhibit favorable agreement. The model successfully reproduced both the tidal and subtidal water levels.

5.1.2 RMSE and CF

The bar graphs of Figures 20(a) and 20(b) display, by station, the RMSE and CF, respectively. The RMSE ranges from 0.06 m to nearly 0.17 m at station 8776604. The CF ranges from 67% to 99%; there is one station, 8776604, which is the outlier at 67%. Not including the two Mississippi River stations (8760721 and 8761955), the average RMSE and CF are equal to about 7.4 cm and 90%, respectively.

Figure 21 displays the RMSE map of the modeled total water level at 55 stations (Table 3). In general, the RMSE does not vary greatly across the model domain, except for stations 8760721 and 8761955 along the lower Mississippi River (MR). Comparing the model-data water level time

series, and taking into account the Mississippi River discharge measured at USGS station 07374000 (Baton Rouge, LA) (Table 4), we conclude that the large RMSE can be attributed to water level setup from the large river discharge event which occurred between May and June of 2017. The river discharge during this period reached a magnitude of around 36400 m^3/s. This very large value of discharge is about three times that of the average value during the entire hindcast period. The river discharge event is very evident in Figure 18.

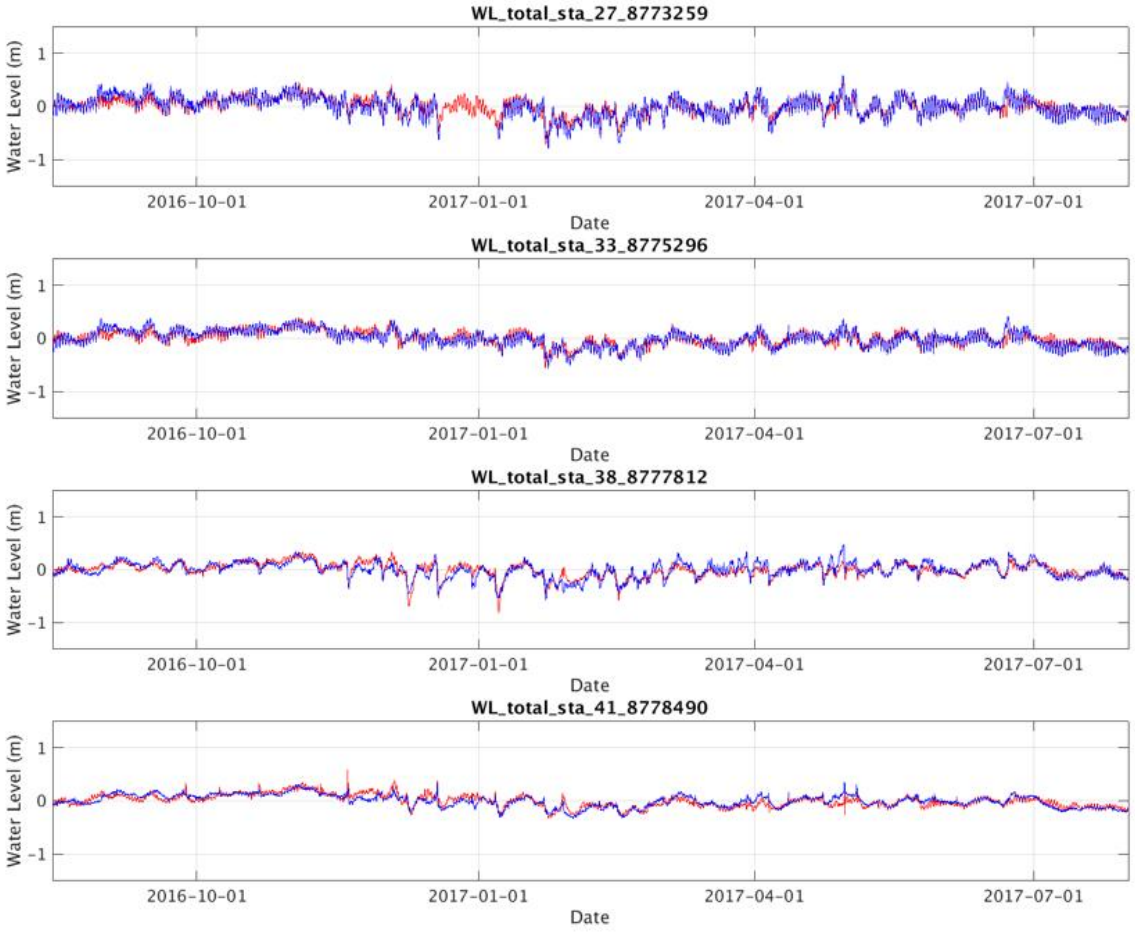

Figure 16. Comparison of hindcast (red lines vs. observed (blue line) water level time series at stations (from top to bottom) 8773259, 8775296, 8777812, and 8778490.

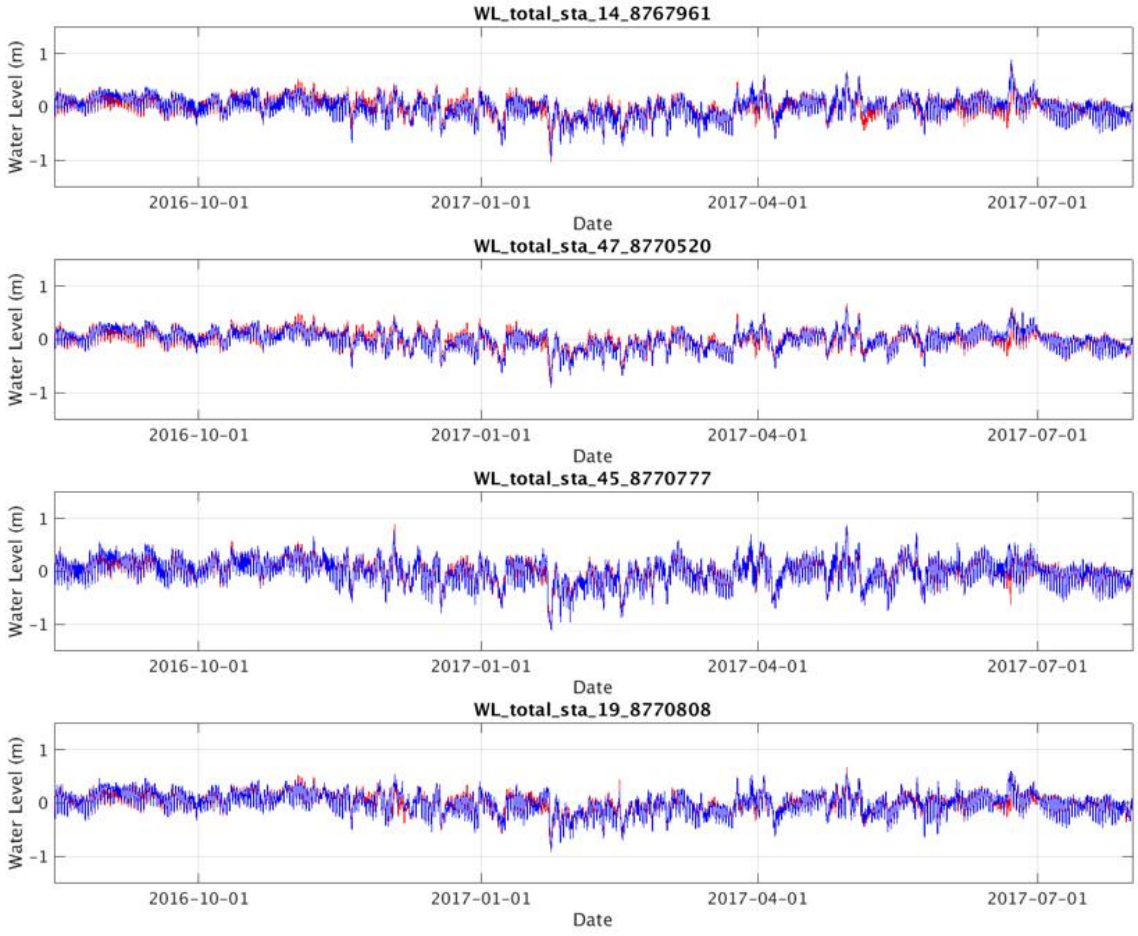

Figure 17. Comparison of hindcast (red line) vs. observed (blue line) water level time series at stations (from top to bottom) 8767961, 8770520, 8770777, and 8770808.

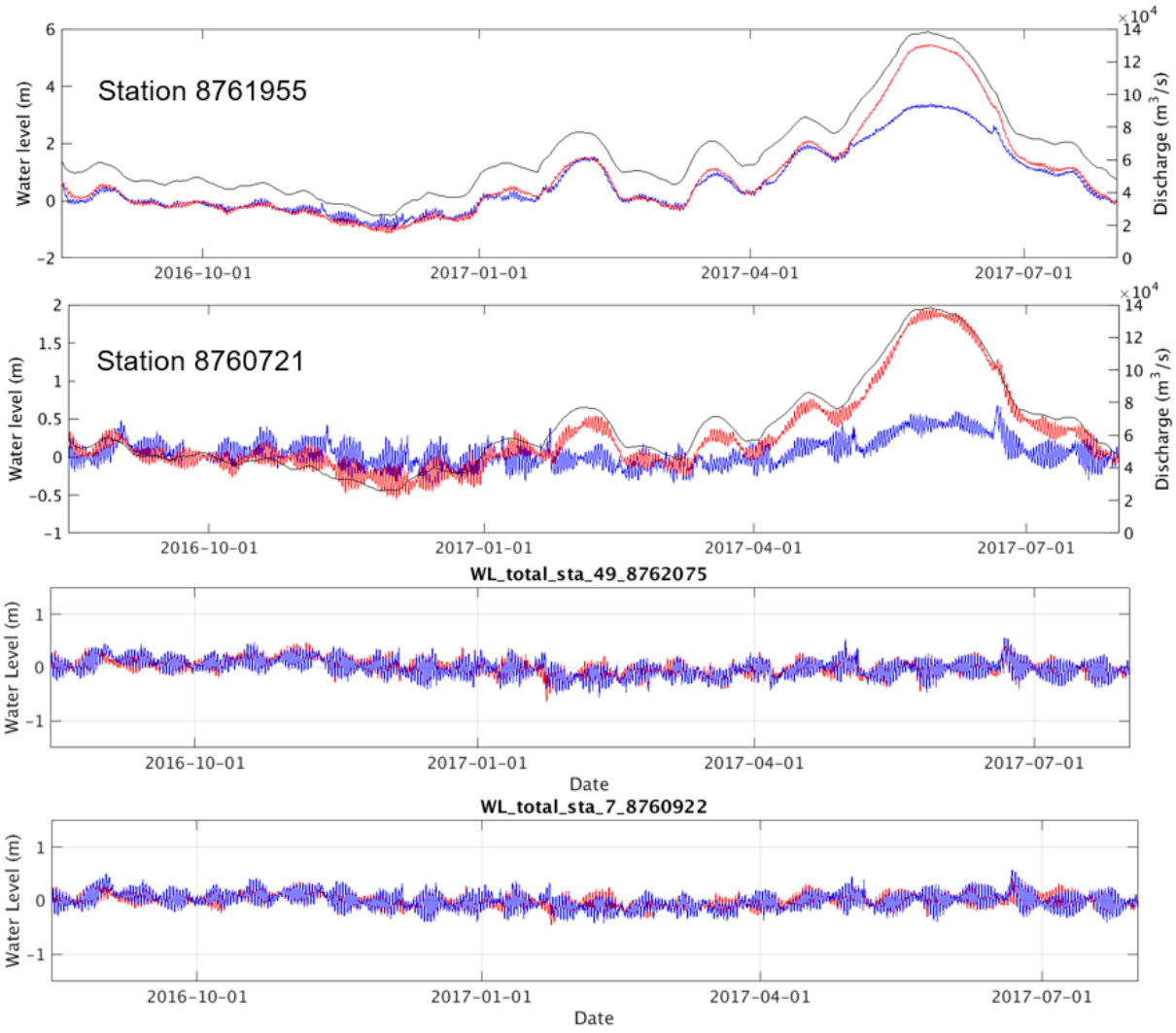

Figure 18. Comparison of hindcast (red line) vs. observed (blue line) water level time series at stations (from top to bottom) 8761955, 8760721, 8762075, and 8760922.

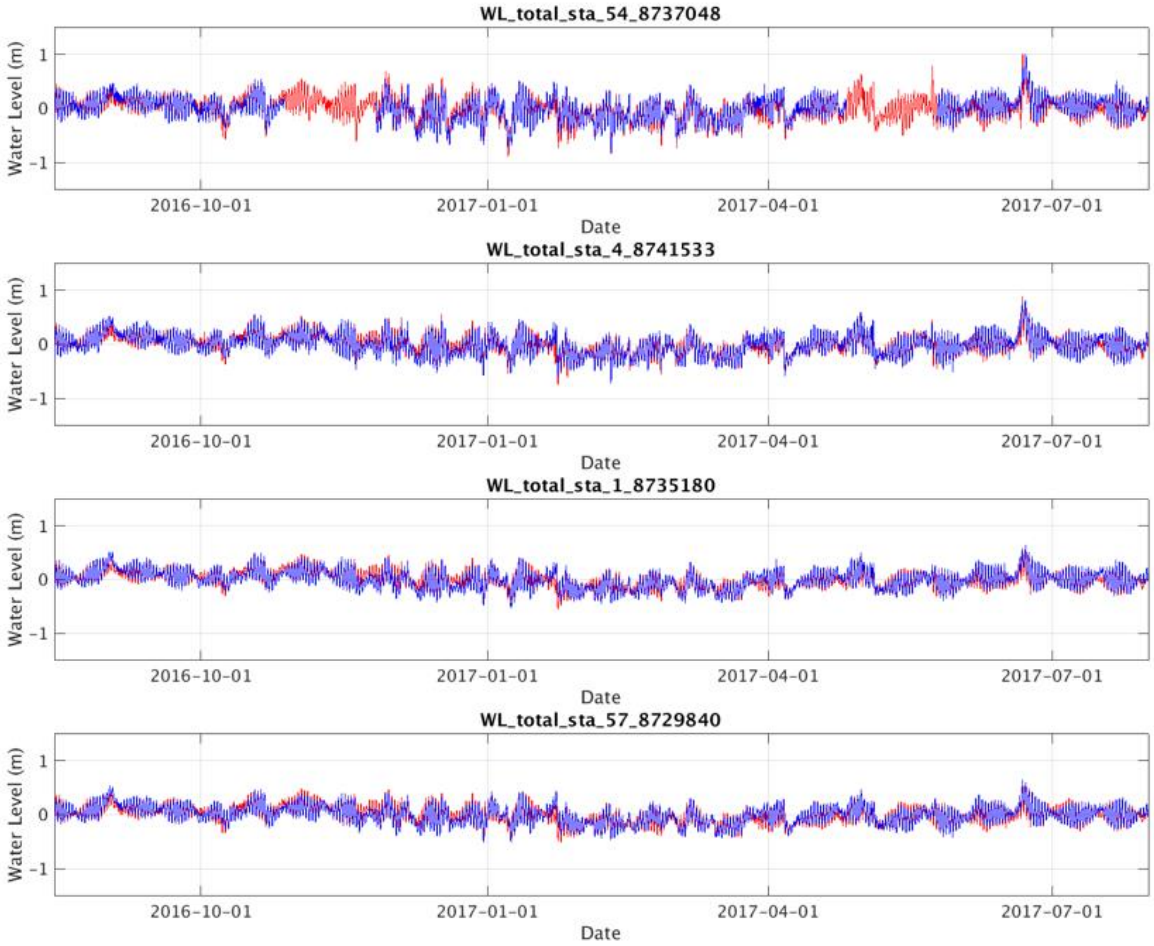

Figure 19. Comparison of hindcast (red line) vs. observed (blue line) water level time series at stations (from top to bottom) 8737048, 8741533, 8735180, and 8729840.

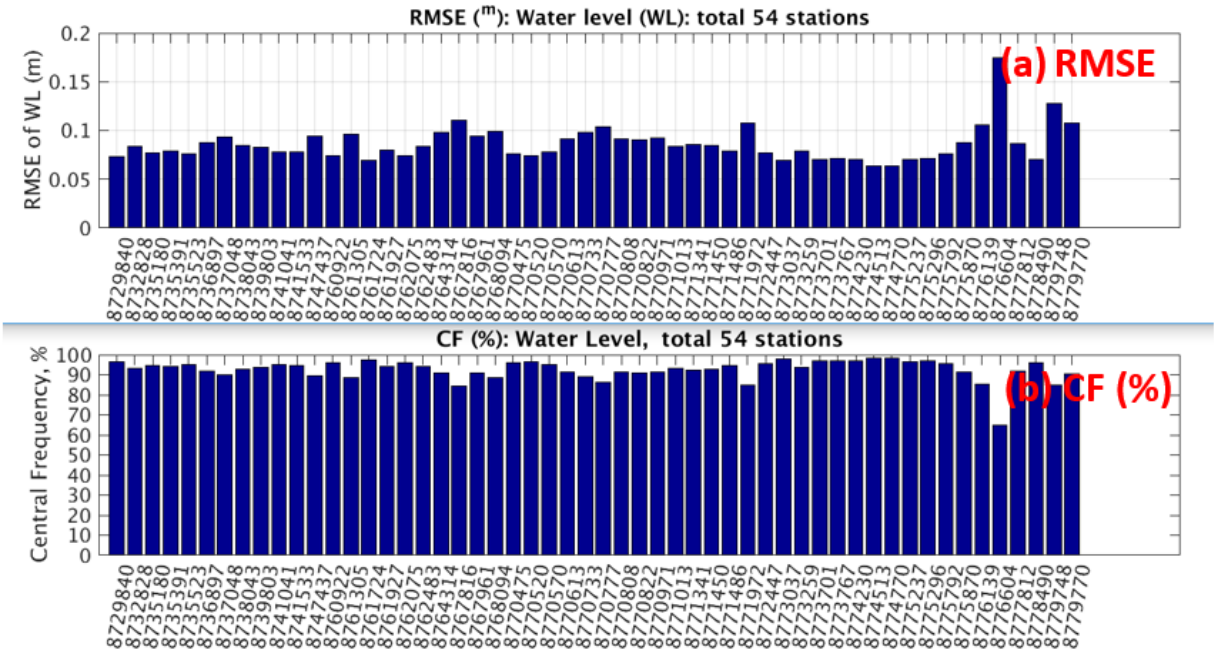

Figure 20. Skill assessment results, (a) RMSE and (b) CF, of the total water level at 54 of the 55 total stations (Table 3). Station 8760721 (Pilot Town) is excluded from display.

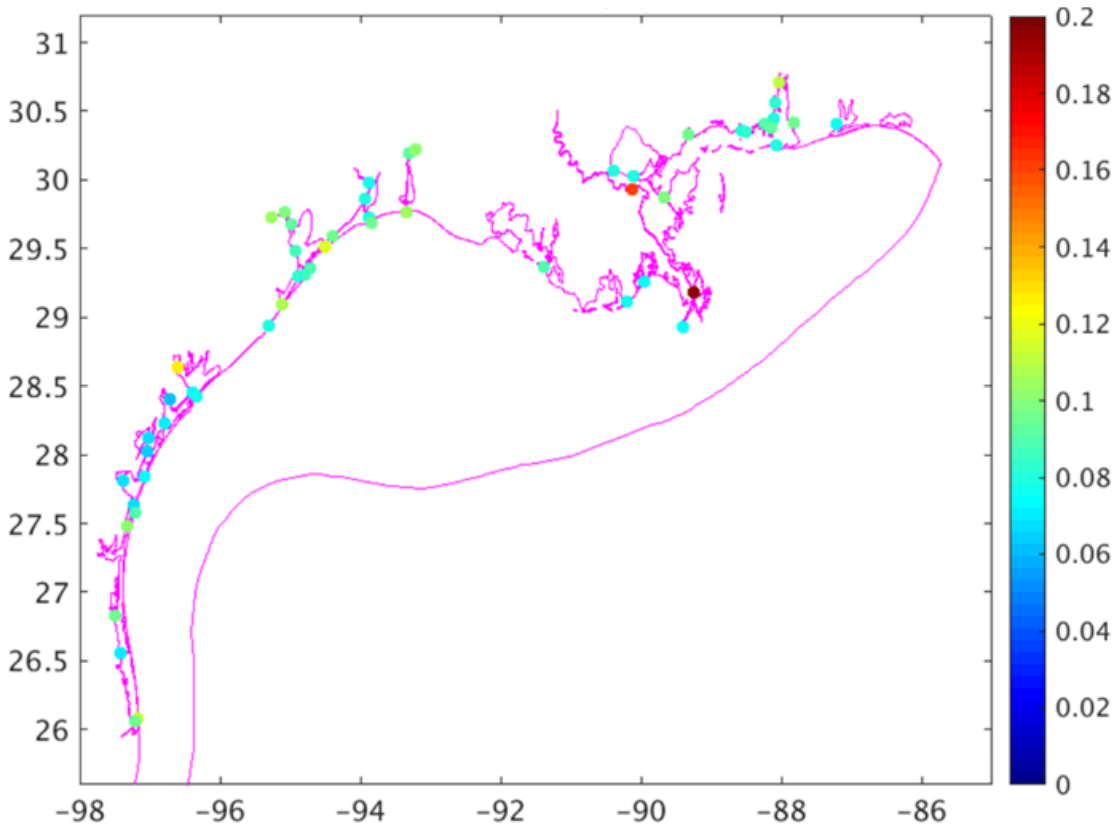

Figure 21. The RMSE of the hindcast total water levels at 55 CO-OPS stations (Table 3).

5.2. Currents

The model current time series and the observed current time series, at 14 CO-OPS CMIST buoys and nine TABS buoys (Section 3.2), were compared. The model outputs at the observation station locations were interpolated onto the corresponding measurement depths at each station.

5.2.1 Time Series

Figures 22-35 show comparisons between the model current time series (red lines) and the observed current time series (blue lines) at 14 stations across the NGOFS2 domain. Shown in these figures are stations located from the southwestern portion of the domain up through the northeastern portion. TABS buoy J (Figure 22) is located in the coastal waters south of Texas. TABS buoy W (Figure 23) is located southeast of Matagorda Bay. CO-OPS CMIST buoy g0601 (Figure 24) is located in the Galveston Bay entrance channel, while TABS buoy F (Figure 25) is located southeast of Galveston Bay. CO-OPS CMIST buoy lc0201 (Figure 27) is located in the entrance to Calcasieu Lake. Buoy lm0201 (Figure 27) is located at Port Allen, near Baton Rouge,

in the lower Mississippi River. CO-OPS CMIST buoy mc0101 (Figure 28) is located in the Atchafalaya Bay Channel, while ps0301 (Figure 29) is located in the Pascagoula River.

The model results display generally favorable agreement with observations in both magnitude and direction. This favorable agreement can be seen in Figures 22 (TABS J), 25 (TABS F), 26 (sn0701), and 27 (lc0201). However, some stations exhibit an appreciable model-data discrepancy. For instance, at station lm0201 (Figure 27), the modeled current amplitude is about 1 m/s greater than the observed current amplitude. In addition, the modeled current, without exception, points in the downstream direction (about 200 degrees from north), whereas the observed direction appears to vary dynamically from about 50 degrees to 250 degrees from north.

At station mb0401 (Figure 28), the model successfully reproduced the subtidal events shown in the current amplitude time series. However, the observed data displayed in the figure demonstrates large current amplitudes at frequencies greater than the tidal frequencies, whereas the model results do not show a similar phenomenon.

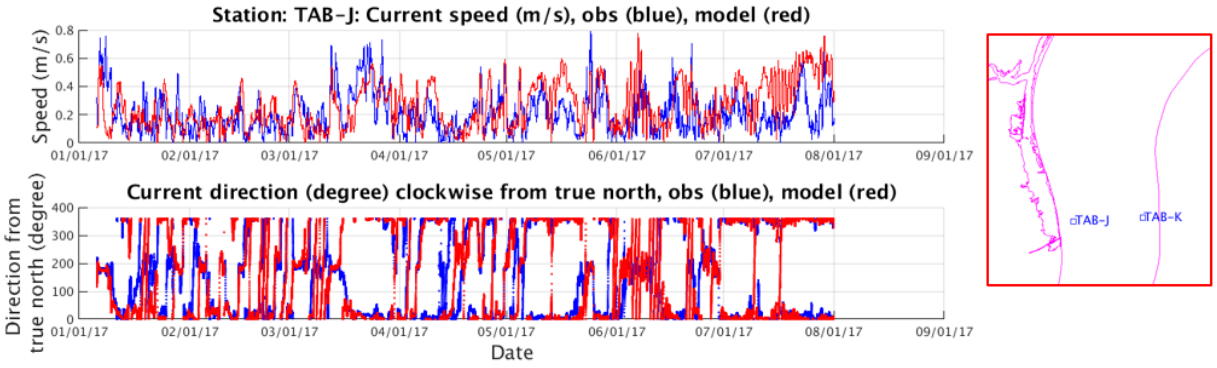

Figure 22. Comparison of modeled (red lines) and observed (blue lines) current amplitude and direction at TABS buoy J.

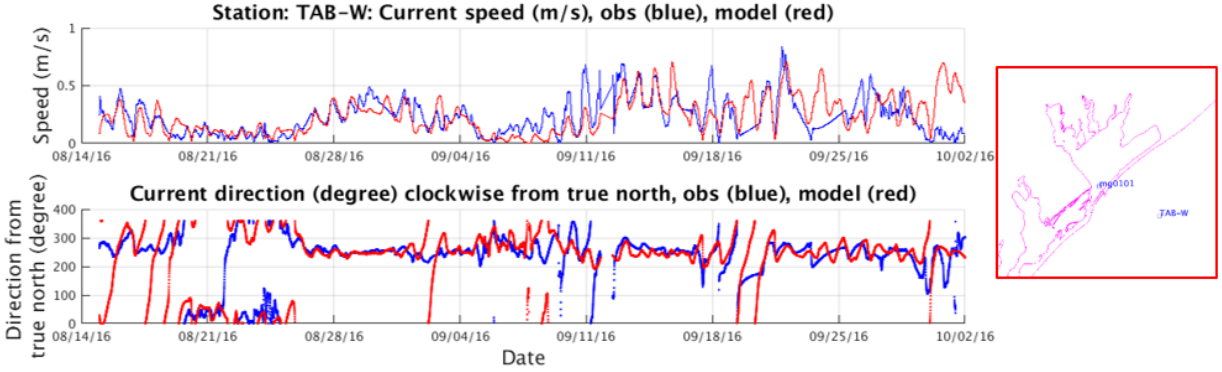

Figure 23. Comparison of modeled (red lines) and observed (blue lines) current amplitude and direction at TABS buoy W.

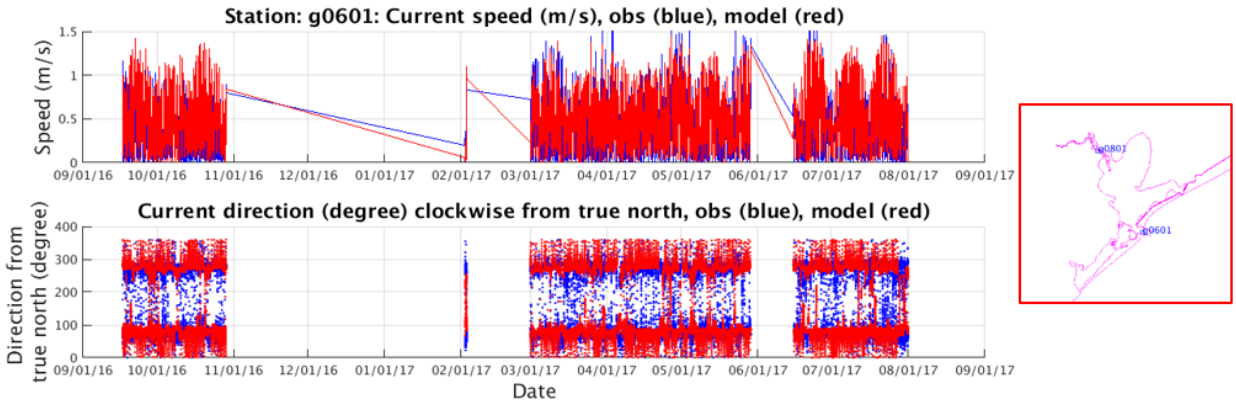

Figure 24. Comparison of modeled (red lines) and observed (blue lines) current amplitude and direction at station g0601. The straight blue lines correspond to periods of observed data gap. Accordingly, the model output for the data gap periods was also displayed as straight lines.

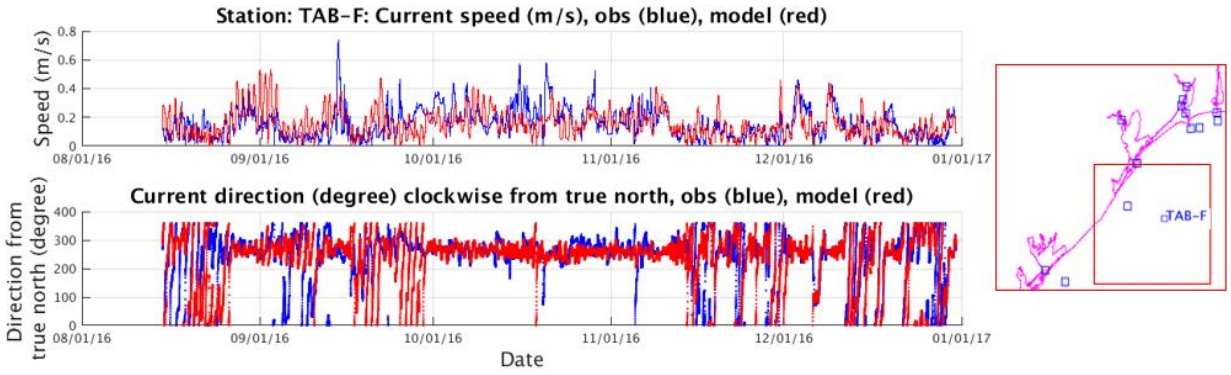

Figure 25. Comparison of modeled (red lines) and observed (blue lines) current amplitude and direction at station F.

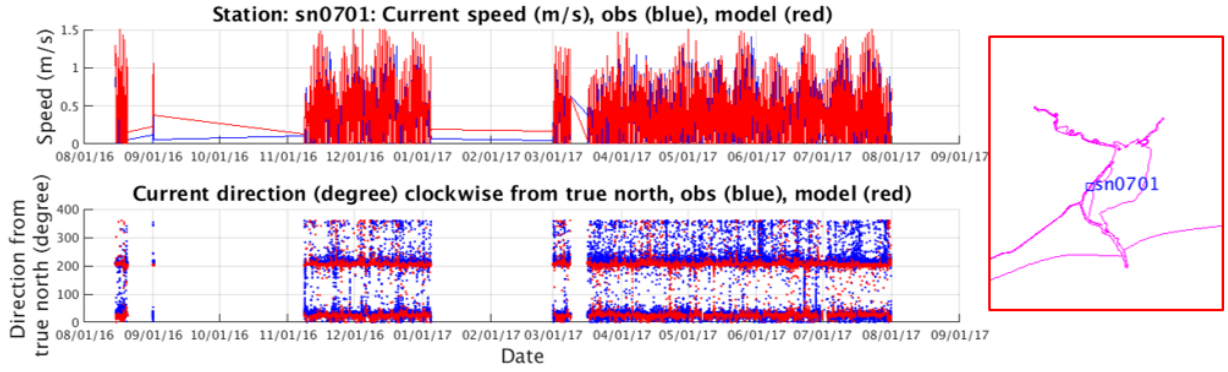

Figure 26. Comparison of modeled (red lines) and observed (blue lines) current amplitude and direction at station sn0701. The straight lines correspond to the periods of data gap. They do not represent the actual data.

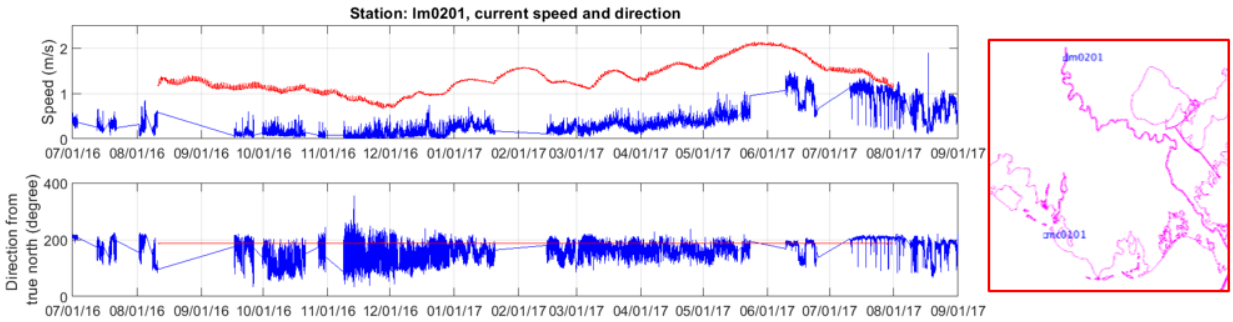

Figure 27. Comparison of modeled (red lines) and observed (blue lines) current amplitude and direction at station lc0201. The straight blue lines correspond to periods of observed data gap. Accordingly, the model output for the data gap periods was also displayed as straight lines.

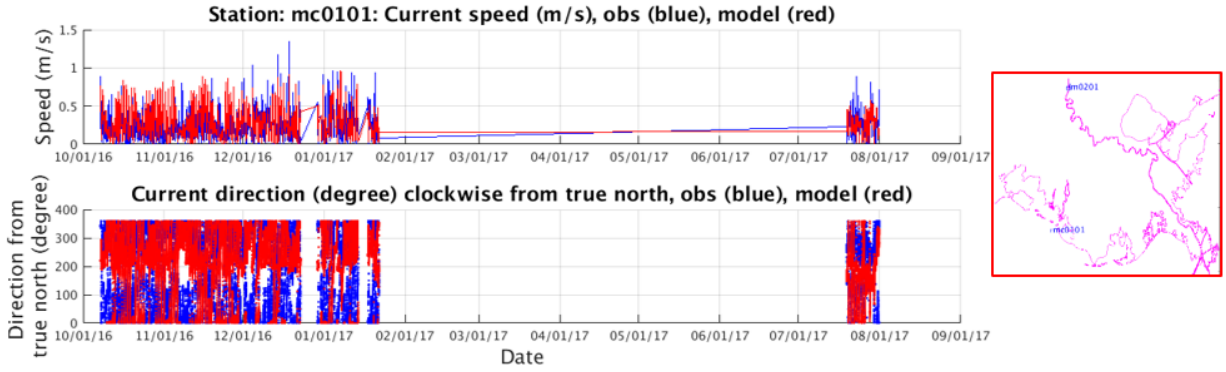

Figure 28. Comparison of modeled (red lines) and observed (blue lines) current amplitude and direction at station mc0101. The straight blue lines correspond to periods of observed data gap. Accordingly, the model output for the data gap periods was also displayed as straight lines.

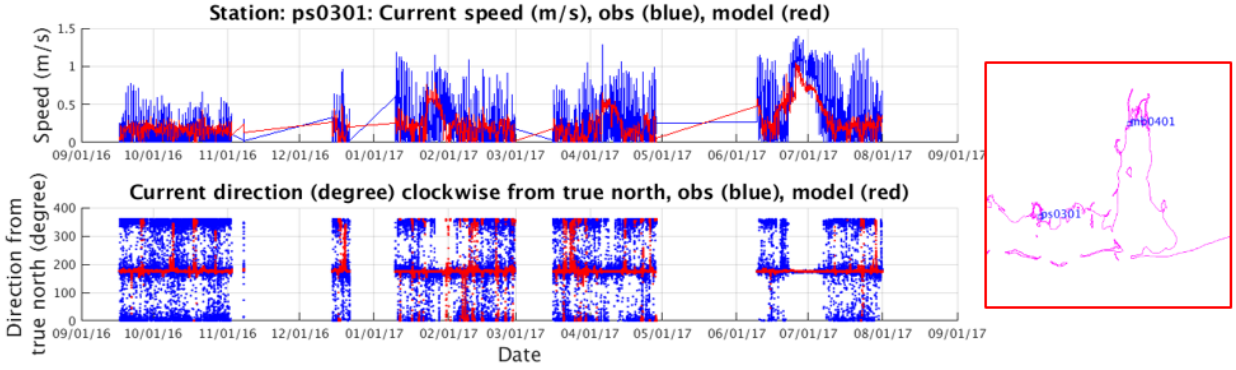

Figure 29. Comparison of modeled (red lines) and observed (blue lines) current amplitude and direction at station ps0301. The straight blue lines correspond to periods of observed data gap. Accordingly, the model output for the data gap periods was also displayed as straight lines.

5.2.2 RMSE and CF

Figures 30 and 31present the model skill assessment results for the current amplitude and current direction, respectively, at 23 stations. In each figure, the bar graphs (a) and (b) display the root-mean-squared error (RMSE) and the central frequency (CF), respectively. For the current amplitude (Figure 30), station lm0201 stands out as an outlier with a very large RMSE of 0.97 m/s and a CF of only 4%. The RMSE and CF, averaged over all 23 stations, are equal to 0.23 m/s and 79.4%, respectively. Excluding station lm0201, over the remaining 22 stations, the average RMSE is 0.19m/s and the average CF is 82.8%.

For current direction, the RMSE and CF over all 23 stations are 12.4 degrees and 95.0%, respectively.

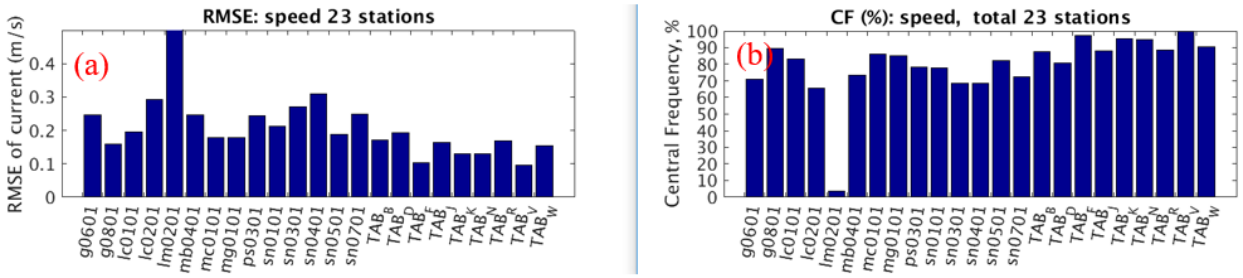

Figure 30. Skill assessment results: (a) RMSE (m/s), and (b) CF (%), of the modeled current amplitudes at 23 stations (Section 3.2).

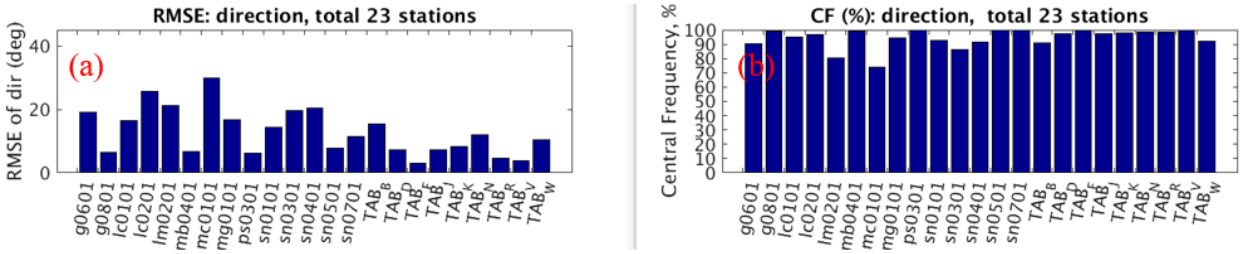

Figure 31. Skill assessment results, (a) RMSE (degrees), and (b) CF (%), of the modeled current direction at 23 stations (Section 3.2).

5.3. Water Temperature

5.3.1 Time Series

Figures 32-35 show both the model (red lines) and the observed (blue lines) sea-surface temperature (SST) time series at 16 stations. The stations in the four figures are located, in (a) the Texas coastal embayments and the adjacent continental shelf waters, (b) Galveston Bay, Sabine

Lake, and Calcasieu Lake, (c) the Lower Mississippi River and adjacent waters, and (d) the Mobile Bay and adjacent waters, respectively. More specifically, stations SDRT2, RCPT2, PMNT2, and 42020 appear in Figure 32; stations BKTL1, PORT2, EPTT2, and 42035 appear in Figure 33; stations CARL1, AMRL1, GISL1, and PILL1 appear in Figure 34; and ULAM6, MCGA1, WBYA1, and PCLF1 appear in (Figure 35). For clarity of display, about ten months (mid-September of 2016 through mid-July of 2017) of the entire one-year comparison are displayed. The model results demonstrate favorable agreement with the observations. The model successfully reproduced both the short term and seasonal variations seen in the observations.

In general, the model and data exhibit more favorable agreement at stations located in the open coastal waters (e.g., stations CARL1 and PILL1 in Figure 34) than those located in nearshore embayments (e.g., stations PMNT2 in Figure 32 and WBYA1 in Figure 35).

5.3.2 RMSE and CF

Figures 36(a) and 36(b) display the skill assessment results of model performance in terms of RMSE and central frequency (CF), respectively. The RMSE values, over all stations, range from around 0.2^{o}C (at station TESL1) to 2.0^{o}C (at station WBYA1). The CF ranges from 89% to 100%. The RMSE and CF, averaged over all 52 stations, are equal to about 1.1^{o}C and 96%, respectively.

Figure 37 displays the color coded RMSE map with 52 stations (Table 5). The figure reveals the spatial variation of model performance across the NGOFS2 domain. In general, the model demonstrates better skill, with RMSE values less than 0.8°C, in the offshore areas as opposed to the nearshore embayments. The embayments generally experience far more complicated ambient conditions, such as large river discharge and significant diurnal cycles in the surface forcing, than do the relatively deeper offshore areas. For this reason, it is far more challenging to accurately reproduce the SST field in coastal embayments than in offshore areas.

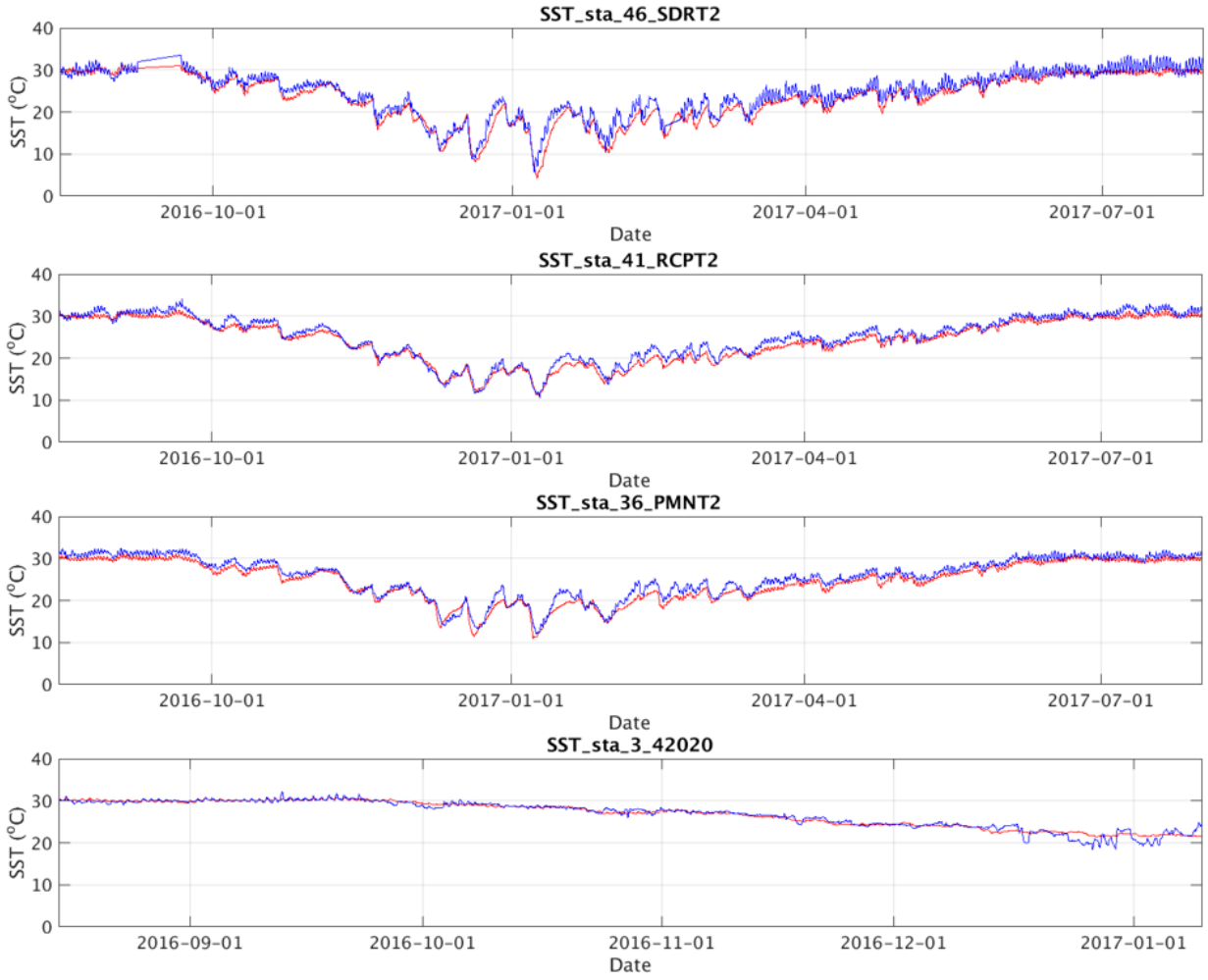

Figure 32. Comparison of hindcast (red line) vs. observed (blue line) sea-surface temperature time series at stations (from top to bottom) SDRT2, RCPT2, PMNT2, and 42020.

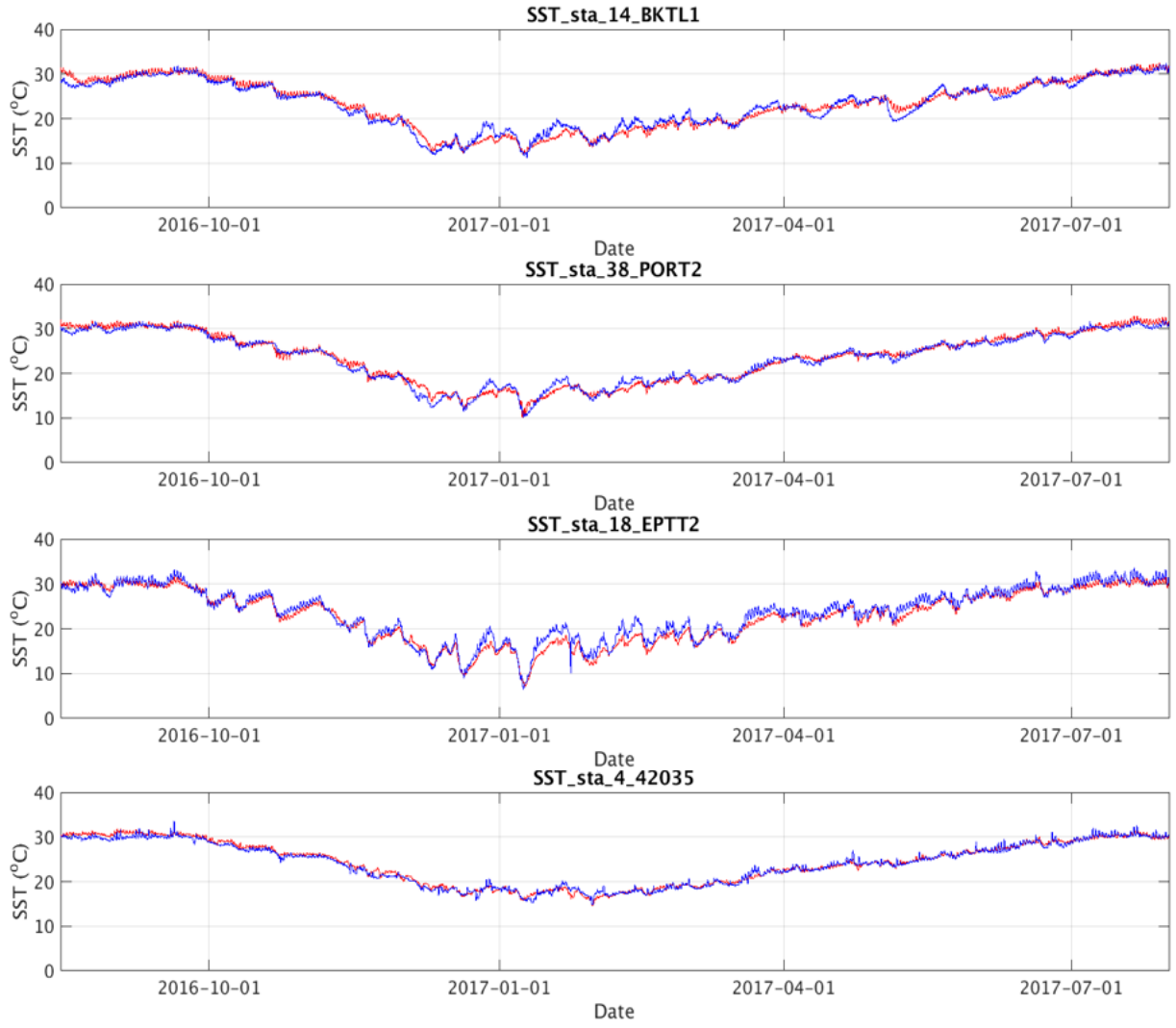

Figure 33. Comparison of hindcast (red line) vs. observed (blue line) sea-surface temperature time series at stations (from top to bottom) BKTL1, PORT2, EPTT2, and 42035.

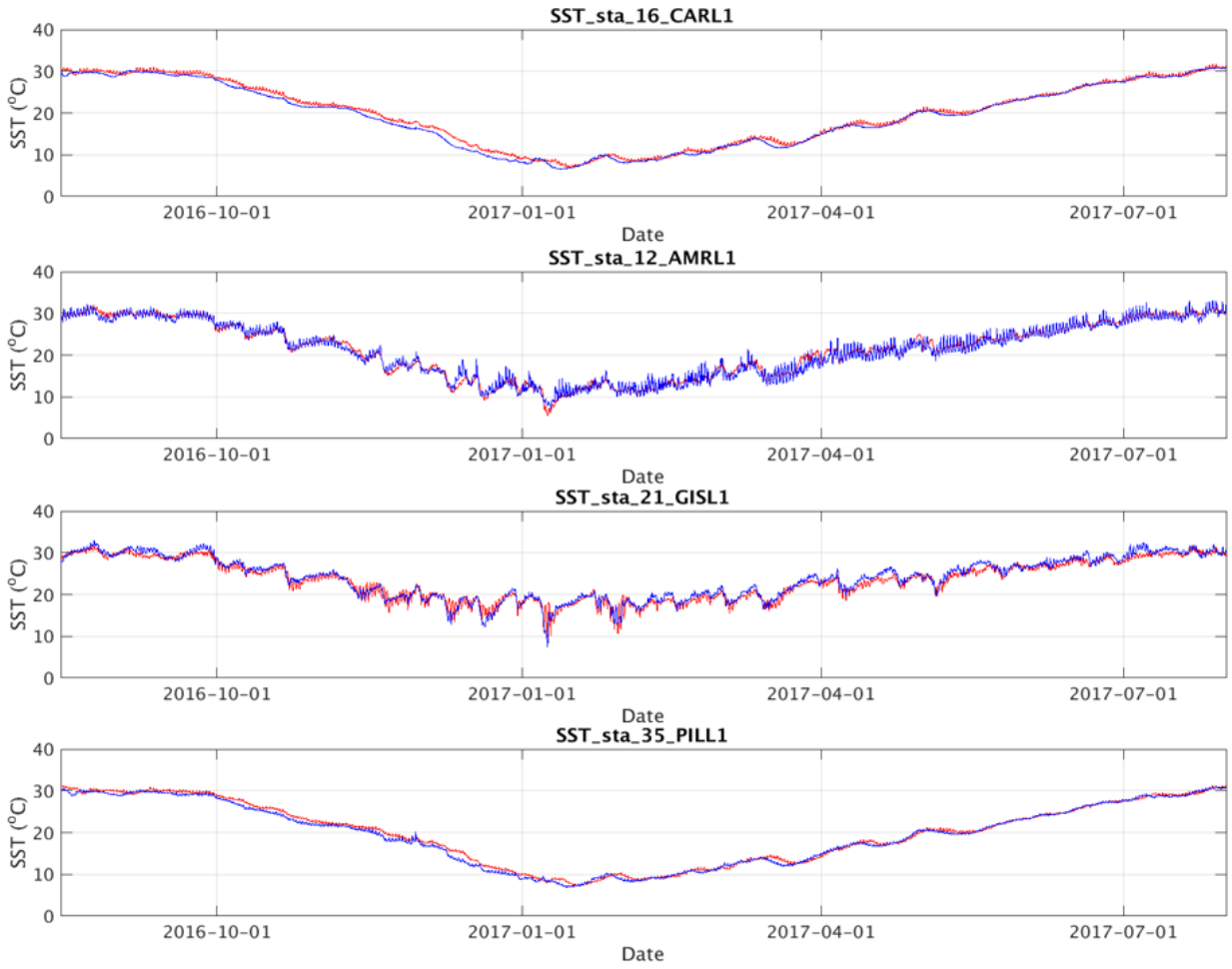

Figure 34. Comparison of hindcast (red line) vs. observed (blue line) sea-surface temperature time series at stations (from top to bottom) CARL1, AMRL1, GISL1, and PILL1.

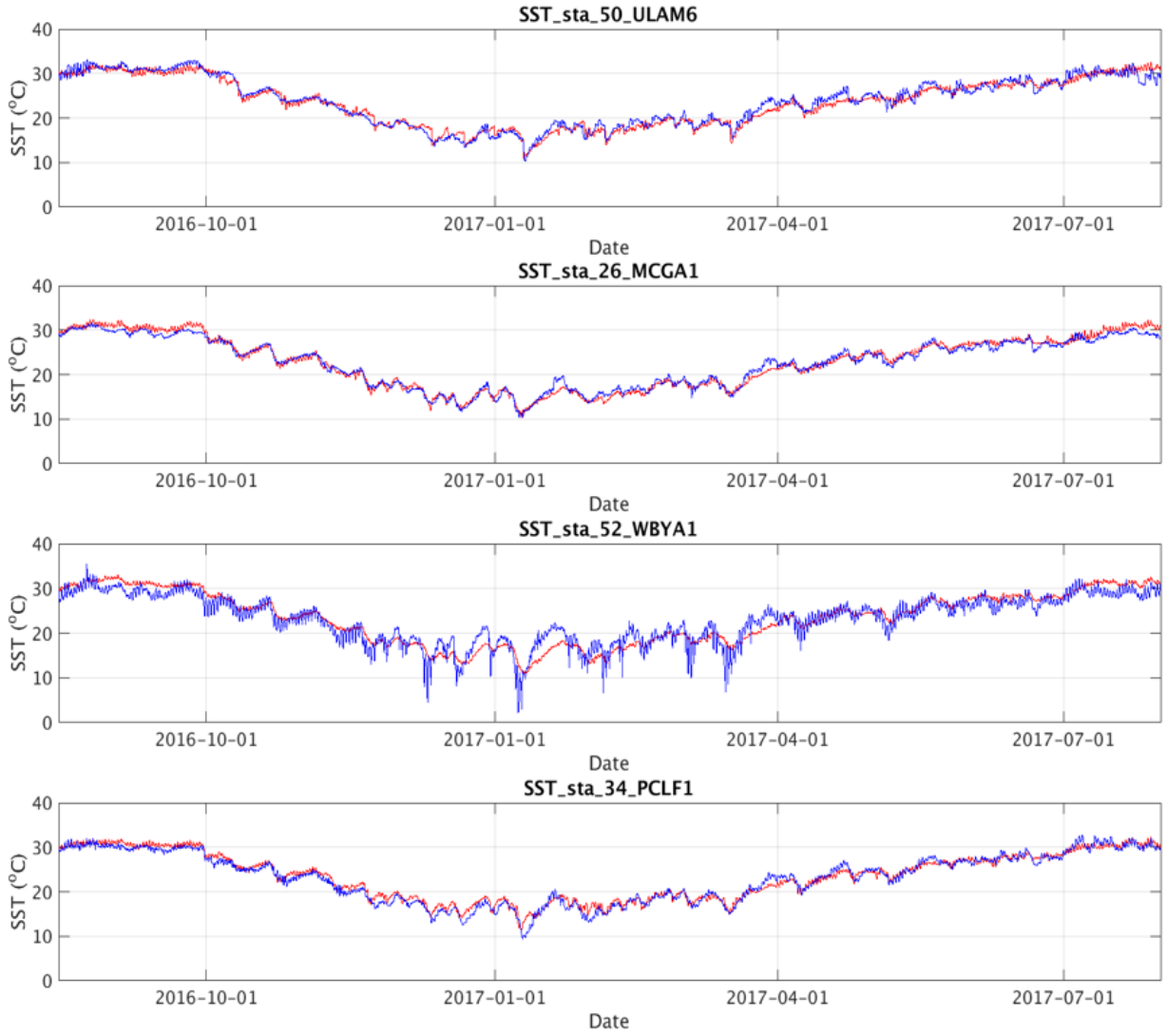

Figure 35. Comparison of hindcast (red line) vs. observed (blue line) sea-surface temperature time series at stations (from top to bottom) ULAM6, MCGA1, WBYA1, and PCLF1.

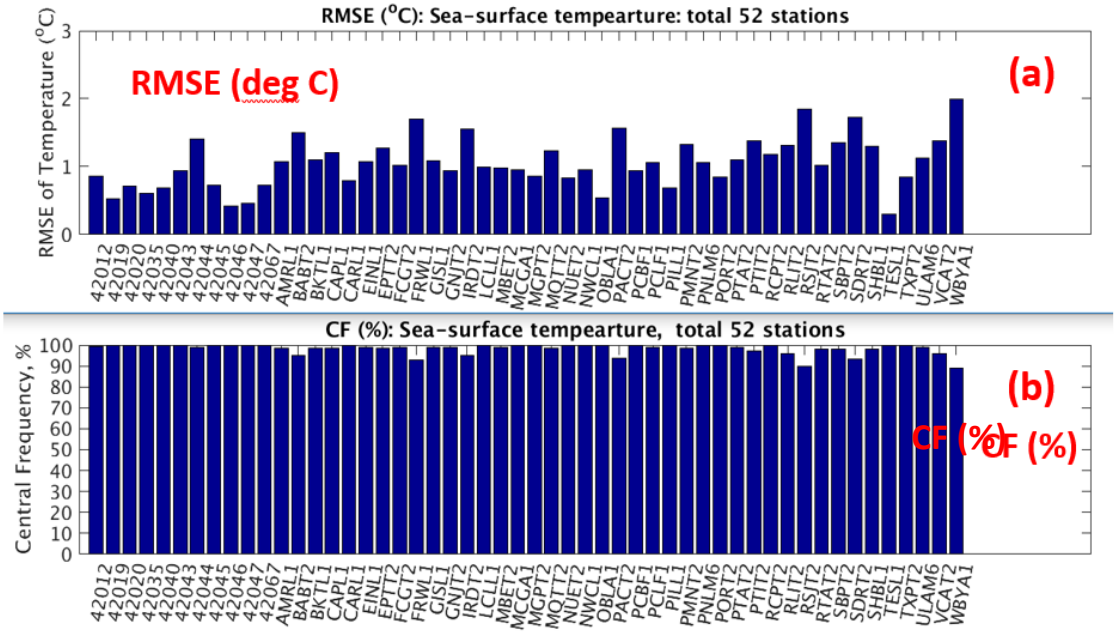

Figure 36. Results from the skill assessment of the sea-surface temperature hindcast, (a) RMSE (°C) and (b) CF (%).

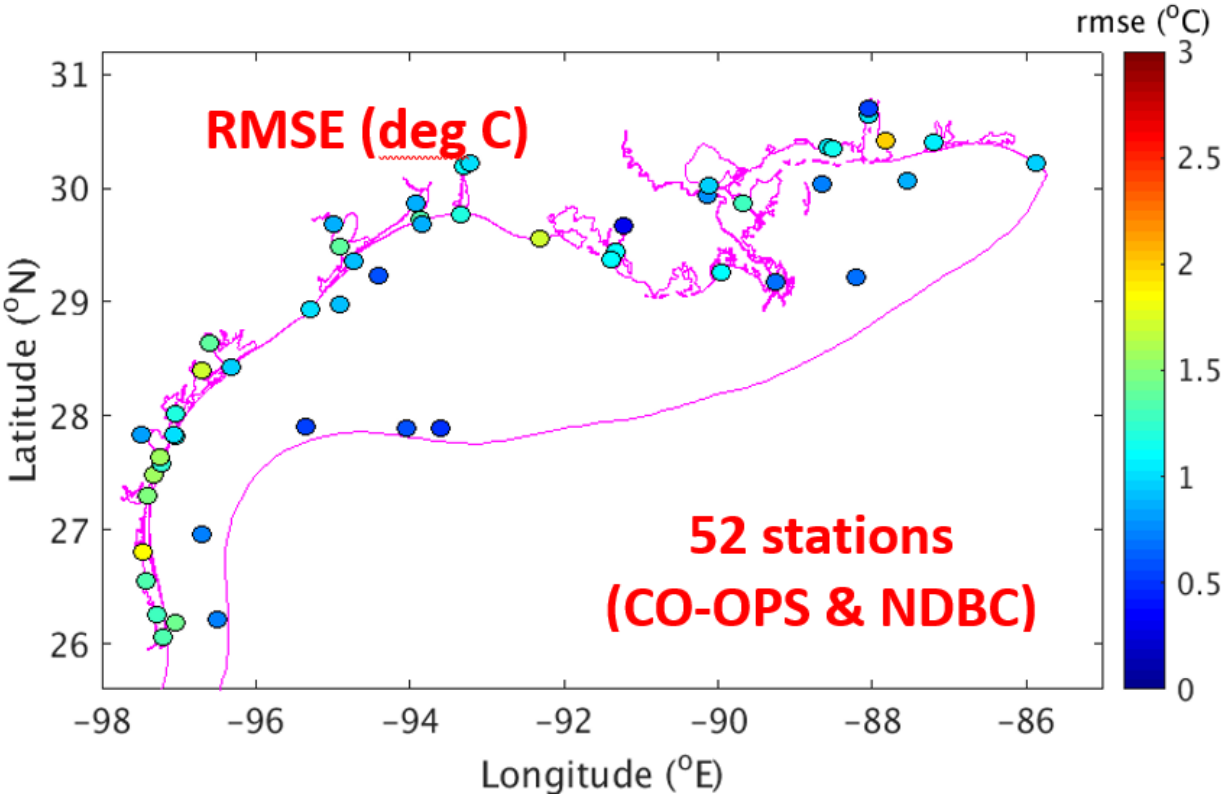

Figure 37. Color coded RMSE of the modeled SST at 52 stations (Table 5).

5.3.3 Monthly Mean

Figures 38(a)-(f) illustrate the monthly model mean and the monthly observed mean SST at stations 42012, MCGA1, NWCL1, PILL1, MGPT2, and EPTT2, respectively. From top to bottom, the stations are located in the open coastal area southeast of Mobile Bay, Lake Pontchartrain, the lower Mississippi River, and the Texas coastal embayment. They were chosen to compare model performance in offshore areas and in embayment areas. In the figure, the left panel depicts the monthly average SST of model (red bars) and observations (blue bars), as well as the standard deviation of each data set. The right panel illustrates the corresponding average model bias (model minus observed) by station for each month.

In general, the hindcast simulation successfully captured seasonal cycles in SST and demonstrates favorable agreement with observations. Both the model and observed SST demonstrate significant seasonal variability ranging from about 9°C in the winter to about 32°C in the summer. The model bias ranges from -1.8 °C (station EPTT2, February) to 1.7°C (station 42012, January). In the summer, the model generally predicted warmer SST with station EPTT2 being the exception. In the winter, the model predicted cooler SST at the open coastal station (42012) and at the lower Mississippi River station (PILL1), and predicted cooler SST at the remaining embayment stations.

Figure 39(a) shows the RMSE averaged over all 52 stations by month. Figure 39(b) shows the absolute average of the model-data differences, averaged over all 52 stations, by month (Table 5). The low value RMSE of 0.7°C occurs first in September of 2016, then again in June of 2017. Both September and June are known to be, in general, quiescent months. The high values of RMSE occur in December 2016 and January 2017, with the January value at 1.5^{o}C. This indicates that the model was least satisfactory in reproducing SST during the winter season. The monthly averaged model bias ranges from -0.3°C to 0.2°C. The bias was positive from August through December of 2016, and negative from January through July of 2017. The model predicted slightly warmer SST during the former period and slightly cooler SST during the latter.

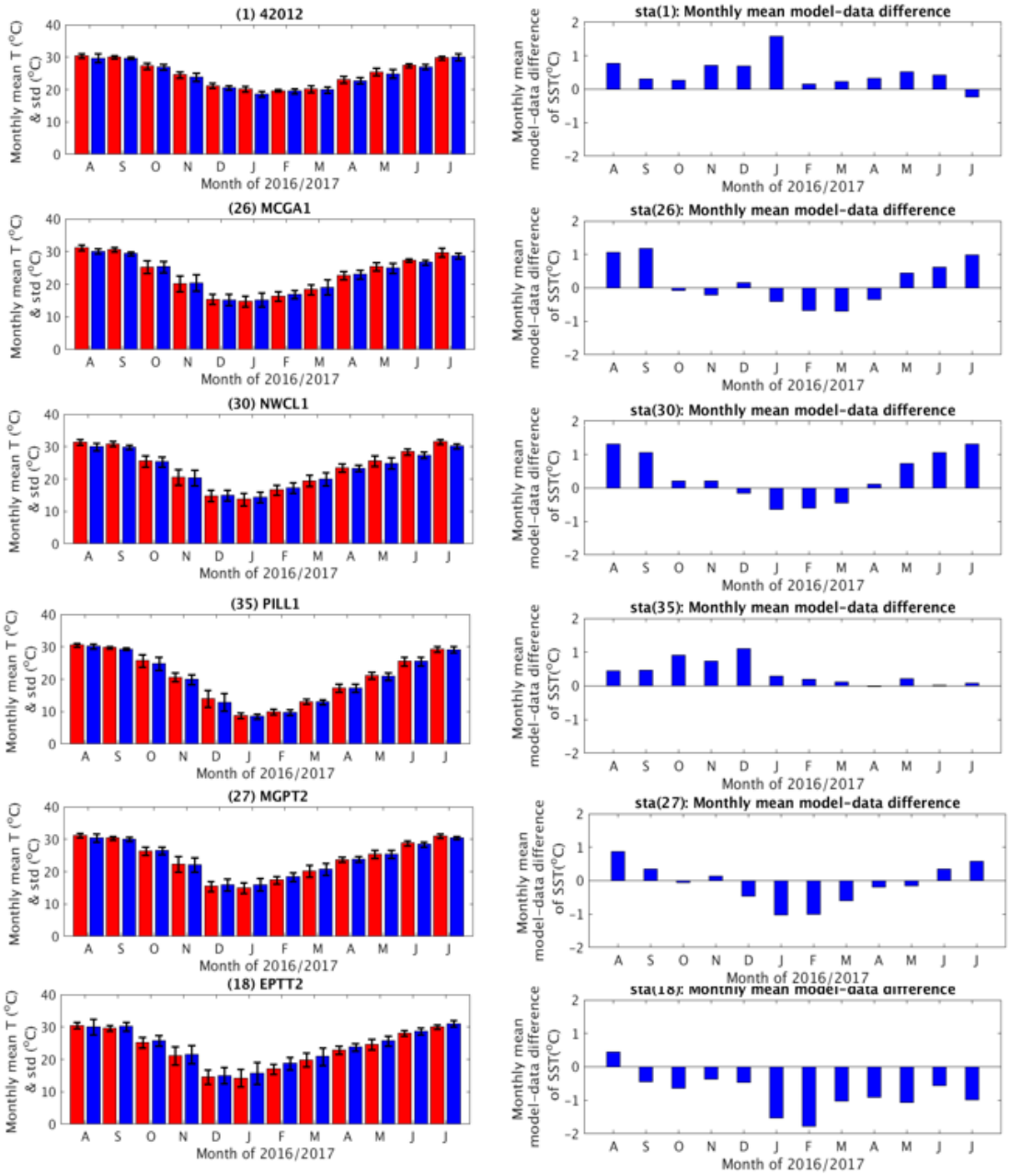

Figure 38. Left panel - Comparison of the monthly model output mean SST (red bars) and the monthly observed mean SST (blue bars). The standard deviation of each data set is also shown. Right panel - monthly mean model bias. The station IDs are shown in the title of each plot.

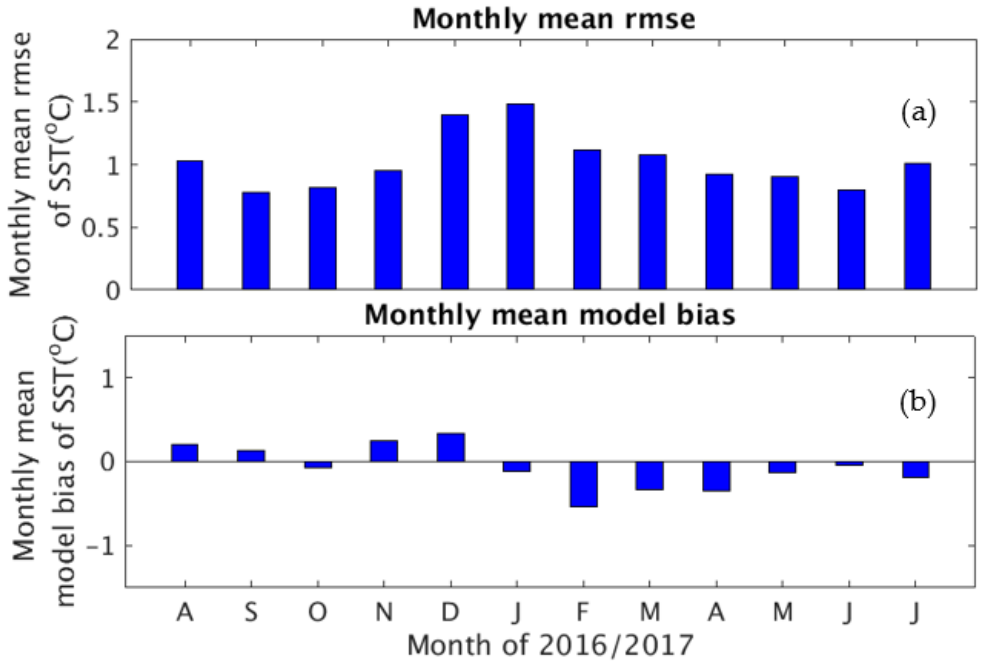

Figure 39. Monthly, averaged over all stations, (a) RMSE and (b) model bias (of the hindcast SST).

5.4. Salinity

During the hindcast period of one year, salinity observations were available at seven buoy stations (Table 3), all of which are situated either inside of or close to Mobile Bay. This area represents a rather small portion of the entire NGOFS2 domain. Buoy 42067 is situated offshore, southwest of Mobile Bay. Buoys BSCA1, CRTA1, DPHA1, and KATA1 are located in the lower portion of Mobile Bay, while buoys MBLA1 and MHPA1 are located in the mid and upper Mobile Bay, respectively.

Malfunction of salinity sensors due to bio-fouling was very common in the coastal areas of the northern Gulf of Mexico (Wei et al., 2014). Some of the observed data was deemed to be false measurements due to instrument malfunction. Figure 40 shows the sea surface salinity (SSS) time series at stations BSCA1 and CRTA1, respectively. To point out several problematic data points, SSS exhibits a nearly 10 psu change within a one-hour period on March 14, 2017 at station BSCA1. Station CRTA1 exhibits a nearly 20 psu daily change on April 10, 2017.

Considering the geographical limitation imposed by station locations and the data quality of the observations, it must be noted that the model-data comparison results presented in this section are far from being an accurate representation of model skill over the entire domain.

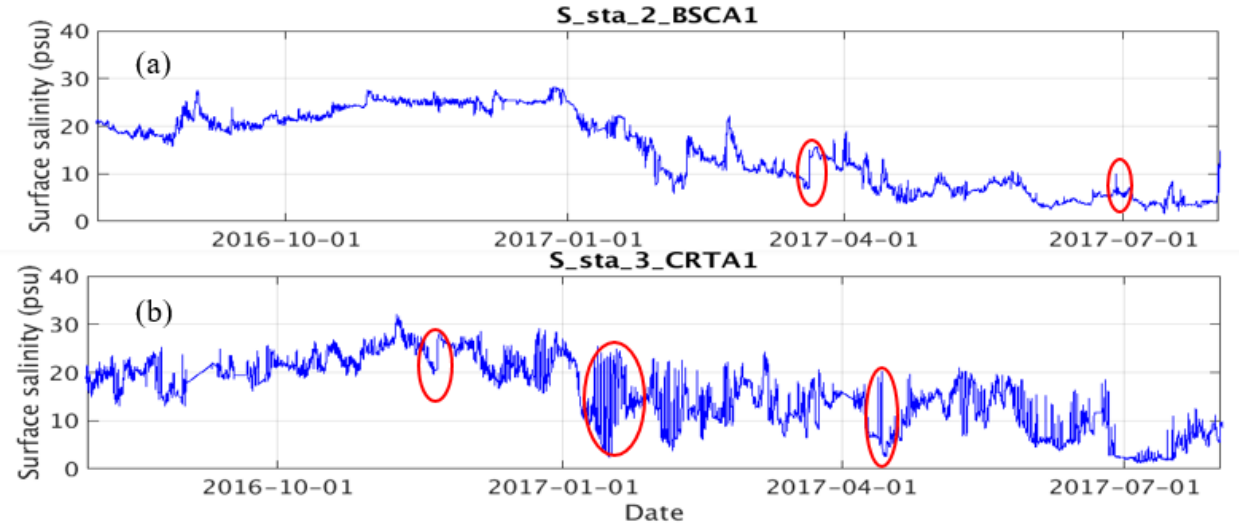

Figure 40. The observed surface salinity time series at stations (a) BSCA1 and (b) CRTA1. Red ellipses mark the occurrences of false sensor measurements.

5.4.1 Time Series

Figure 41 shows both the model (red lines) and the observed (blue lines) sea-surface salinity times series for the one-year hindcast period at the seven stations. The model and data exhibit generally favorable agreement. In general, the hindcast reproduced both the magnitudes and the temporal variations shown in the observations.

However, at some stations, model-data discrepancies are evident. For instance, the observed data at stations CRTA1 and DPHA1 exhibit high-frequency salinity variability of around 10 to 20 psu starting in mid-December 2016 and continuing until July 2017. The hindcast simulation did not produce similar results. At station KATA1, from mid December 2016 and April 2017, the hindcast under predicted salinity, and added some high frequency variation to the signal as well. It over predicted salinity at station BSCA1 from mid-September 2016 through mid-January 2017.

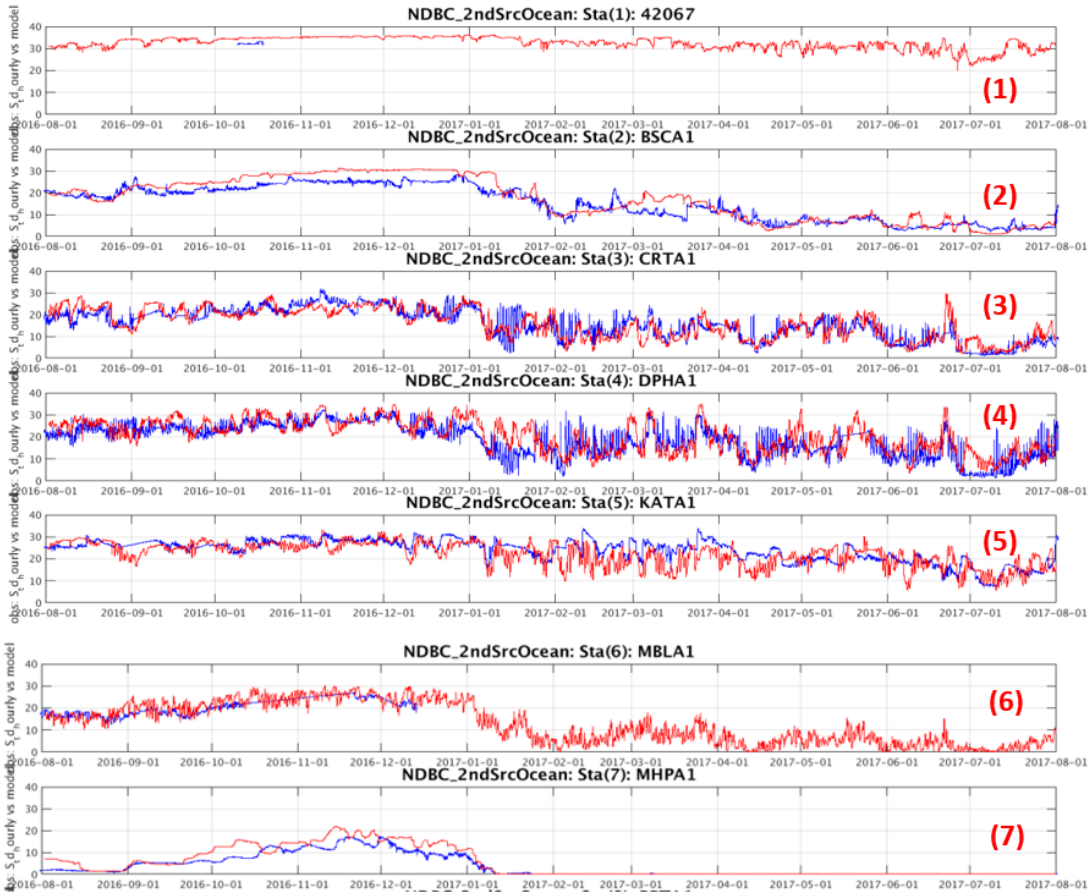

Figure 41. Time series of the modeled (red lines) and the observed (blue lines) sea-surface salinity.

5.4.2 RMSE and CF

Figures 42(a) and 42(b) display the RMSE and the central frequency (CF) from the skill assessment results. The RMSE values range from 2.6 psu at station 42067 to 5.4 psu at station DPHA1. The CF ranges from 50.5% at station DPHA1 to 100% at station 42067. The RMSE and CF, averaged over all seven stations, are equal to about 3.76 psu and 70.6%, respectively.

The RMSE at stations DPHA1 and KATA1 are 5.4 psu and 5.0 psu, respectively. These RMSE values are much greater than those of the other stations. The two stations are located in the vicinity of Dolphin Island (Figure 10 in Chapter 3). Station KATA1 is located north of the island along the western passage into Mobile Bay. Station DPHA1 is located in the eastern passage to Mobile Bay and is situated just off the eastern coast of Dolphin Island. These areas usually experience intense water mass exchanges between the interior of Mobile Bay and the adjacent, open, coastal area. As a result, both the circulation fields and the salinity fields are highly dynamic. This dynamic effect

presents an appreciable challenge for hindcast simulation to realistically reproduce the salinity field of the area, and hence, has produced relatively large RMSEs.

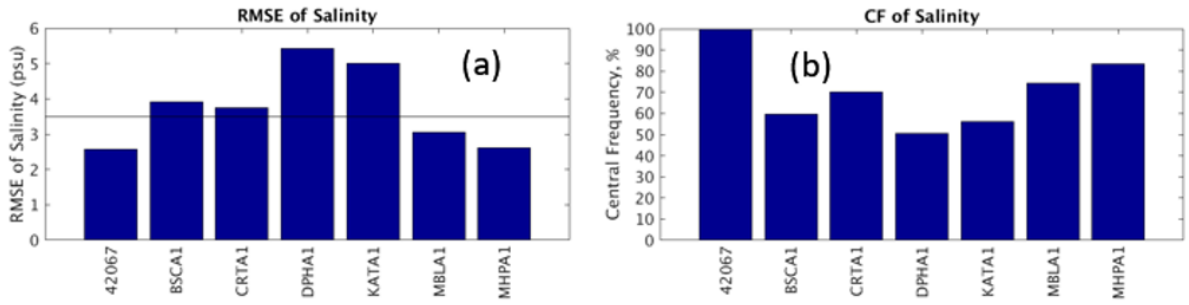

Figure 42. Skill assessment results of the sea-surface salinity hindcast, (a) RMSE (psu) and (b) CF (%).

5.4.3 Monthly Mean

Figure 43 compares the monthly mean SSS, observed vs. model, at the seven stations. The left panel shows the model means (red bars) and the observed means (blue bars), as well as the standard deviations for each month. The right panel shows the mean model bias for each month. The modeled and observed SSS exhibit similar seasonal variability. In general, SSS gradually increases from the summer of 2016 and peaks at nearly 32 psu by December of 2016. Approaching the summer of 2017, SSS drops to around 5-13 psu in the mid-bay area (station MBLA1), and even reaches a near zero value in the upper bay at station MHPA1. The yearly mean model RMSE at each station was 2.6 psu (42067), 3.7 psu (BSCA1), 3.8 psu (CRTA1), 5.4 psu (DPHA1), 4.9 psu (KATA1), 3.0 psu (MBLA1), and 2.7 psu (MHPA1).

The right panel shows the monthly mean of absolute model-data difference. For all stations, the monthly averaged model bias ranges from -6 psu to 6 psu. Model skill was least satisfactory in the winter season of the year. The model bias ranges from about 2 psu in February 2017 to 2.1 psu in January 2017 with a yearly average of 0.7 psu at all stations. The model overpredicted SSS between February and April of 2017 and over predicted SSS in the remaining hindcast period.

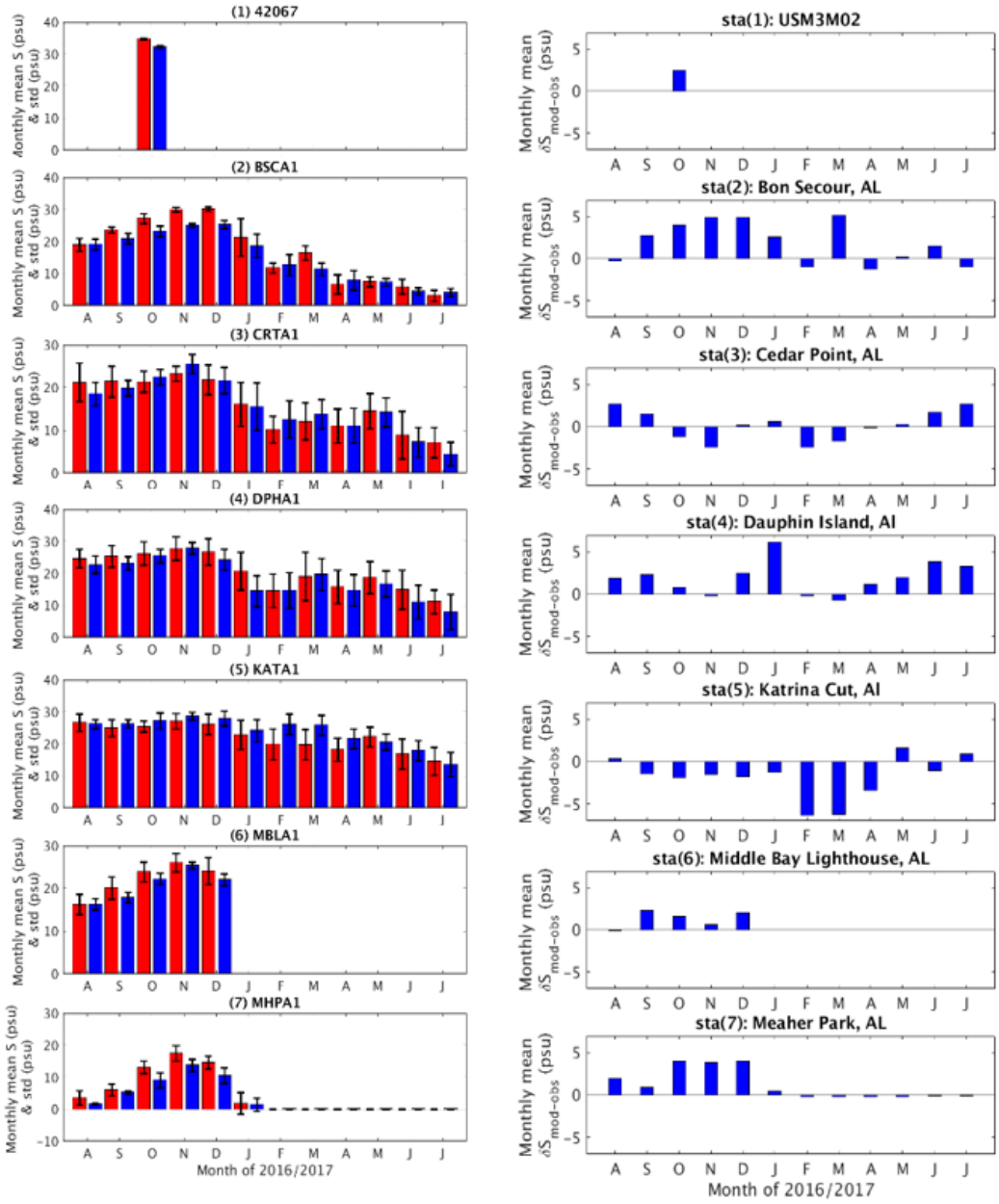

Figure 43. Comparison of the monthly mean hindcast SSS and the monthly mean observed SSS. The left panel shows the monthly mean SSS of the model (red bars) and the monthly mean SSS of the observations (blue bars), along with the standard deviation. The right panel shows the monthly mean model bias. The station IDs are shown in the title of each plot.

5.4.4 Impact of Initial Conditions

The initial salinity conditions for the hindcast runs (presented in Section 5.4.1) were interpolated using the combined NGOFS and NWGOFS/NEGOFS outputs. As a test, we ran an additional hindcast simulation using the initial conditions populated with the G-RTOFS salinity field. The G-RTOFS domain does not cover small coastal embayments such as Mobile Bay, Galveston Bay, etc. Hence, the NGOFS2 salinity field in these areas was extrapolated from the nearest G-RTOFS offshore model grid points outside of the embayments. As a result, the NGOFS2 initial salinity fields, in the embayments, are much more saline than are the observations and may produce a large model-data discrepancy.

The model time series, from the two different sets of initial conditions, were compared with observations at six stations in the Mobile Bay area (Table 6). Figure 44 shows the surface salinity time series at the upper bay station MHPA1, at mid-bay stations MBLA1 and BSCA1, and at the offshore station 42067. They represent the upper bay, the mid-bay, and the offshore station, respectively. It was found that the impact of initial conditions may persist for as long as two and a half months (until mid-October 2016) in the upper and lower bay region, for nearly three months (until the beginning of November 2016) at the mid-bay station, and for about one and a half months at the offshore station. After the first one to two months, the two salinity time series gradually converge, and the impact of the difference in initial conditions becomes nearly indiscernible.

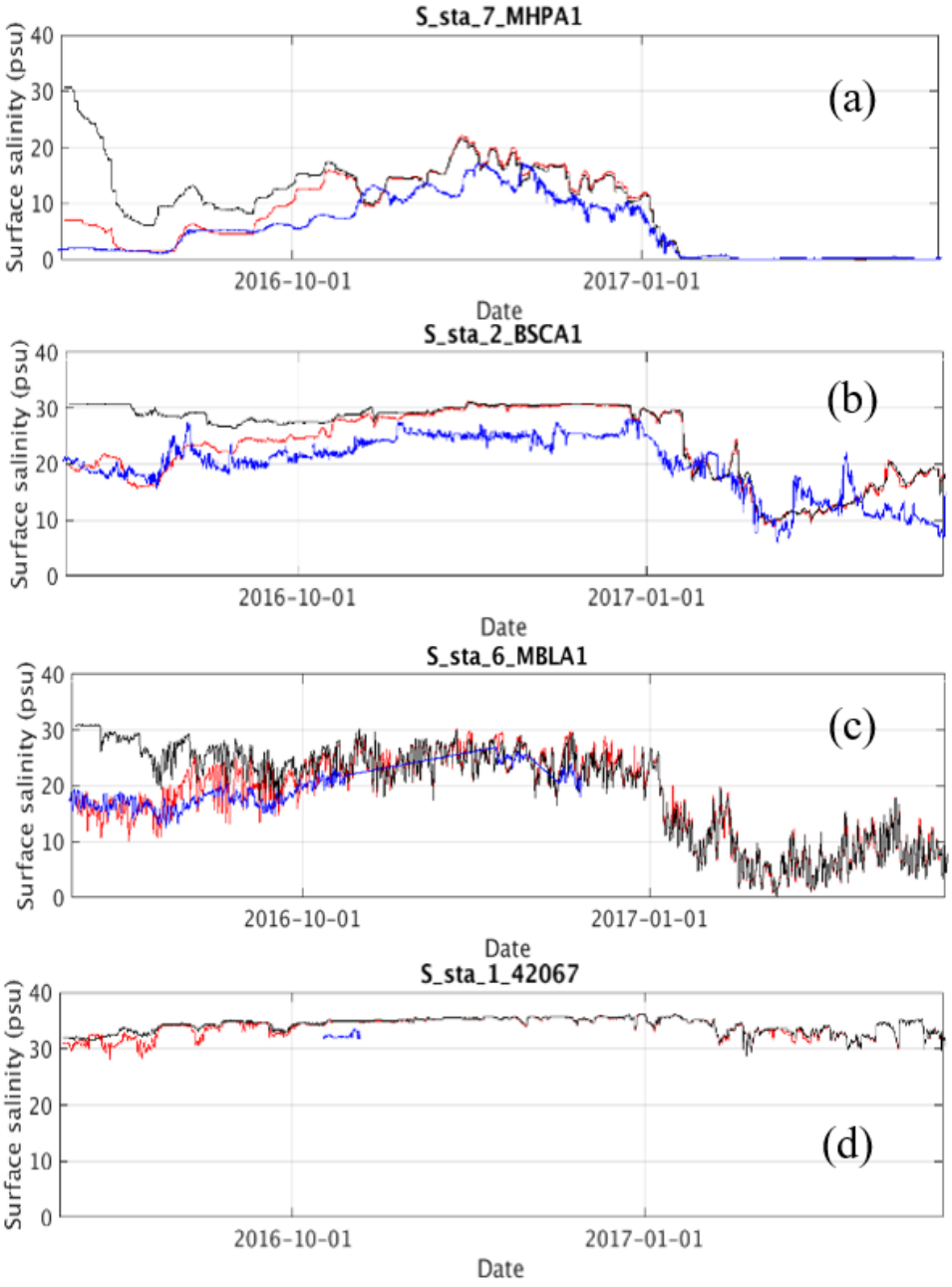

Figure 44. Comparison of the observed (blue lines) and the hindcast (black and red lines) surface salinity time series at stations (a) MHPA1, (b) MBLA1, (c) BSCA1, and (d) 42067. The two model time series correspond to initial salinity conditions populated with G-RTOFS (black lines) and NGOFS (red lines), respectively.

6. IMPACT OF MODEL CONFIGURATIONS ON WATER LEVELS

6.1. River Discharge on Model Grid Nodes vs. Element Edges

This section compares the model generated water levels when using two different approaches to specify the river forcing from discharge data. The FVCOM model allows for two methods to specify the river discharge forcing: the first is to apply the discharge values to the model grid nodes and the second is to apply the discharge values to the model grid elements. The former method distributes the total river discharge across the nodes on the river boundary; the latter method distributes the river discharge across the boundary elements. The FVCOM user manual describes the underlying numerical algorithm.

The two approaches introduce the same volume of river discharge into the river course and hence, in principle, should produce very similar results. However, in practice, the FVCOM community has reported cases in which the method of applying river discharge to the elements may produce lower water levels than the alternative method of applying discharge to the nodes. To assess actual results in the case of the lower Mississippi River, we conducted separate model runs using both approaches. Both runs share the same model setup as the hindcast runs (Chapter 5), and share the same one year simulation period. The only difference between the two runs is the method used to specify river forcing.

When we distribute the river discharge across the river boundary nodes, the nodes include numbers 303711, 303712, 303713, and 303714 (Figure 45). When the river discharge was distributed across the boundary elements, the affected elements include numbers 569401, 568402, and 569404. Figure 46 shows the time series of river discharge from the Mississippi River across node 303712 (USGS river gauge station 07374000). Figures 46 and 47 show the time series of river discharge allocated to node 303711 and to element 569401, respectively.

We calculated the average water level (WL_{avg}) for each model node, over the entire model domain, for the one year simulation period. The mean water level using the node river discharge approach, $WL_{avg\text{-}node}$, ranges between -0.16 m and 5.24 m. The mean water level using the element river discharge approach, $WL_{avg\text{-}ele}$, ranges between -0.16 m and 5.15 m. Figures 46(a) and 46(b) show the water level average in the lower Mississippi River area using the node river forcing approach and the water level average using the element river forcing approach, respectively. Not surprisingly, $WL_{avg\text{-}node}$ and $WL_{avg\text{-}ele}$ exhibit results that are nearly equal.

Figure 49(a) displays the difference of the averaged water level values, $\Delta WL = WL_{avg\text{-}node} - WL_{avg\text{-}ele}$, over the entire NGOFS2 model domain. Figure 49(b) provides a close up view of Figure 49(a) in the lower Mississippi River area. Along the lower Mississippi River, the magnitude of difference appears to be greatest near the upstream boundary of the river grid and to be nearly zero in the broad coastal area of the lower Mississippi sound.

Figure 50(a) shows WL_{avg} along the lower Mississippi River from both the node and element river discharge forcing cases. Figure 50(b) shows $WL_{avg\text{-}node}$ - $WL_{avg\text{-}ele}$ along the same path as that of the above. The inset of Figure 50(b) illustrates the path along which the water level plots were made. The inset of Figure 50(b) provides a magnified view of $WL_{avg\text{-}node}$ - $WL_{avg\text{-}ele}$, for points one through 100, near the upper stream boundary of the river grid.

Both $WL_{avg\text{-}node}$ and $WL_{avg\text{-}ele}$ decrease monotonically from about 5.1 m near Baton Rouge to near zero at the river entrance to coastal waters. The water level difference, $WL_{avg\text{-}node}$ - $WL_{avg\text{-}ele}$, increases monotonically from about -5 cm to zero cm along the path, except for the initial seven nodes on the very northern boundary where some oscillations were revealed. The oscillations range between about -13 cm and -3 cm.

The mean magnitude of $WL_{avg\text{-}node}$ - $WL_{avg\text{-}ele}$ is less than one percent of the mean of either $WL_{avg\text{-}node}$ or $WL_{avg\text{-}ele}$. It is therefore concluded that along the lower Mississippi River course, the differences in yearly averaged water levels between the node river discharge approach and the element river discharge approach are statistically insignificant.

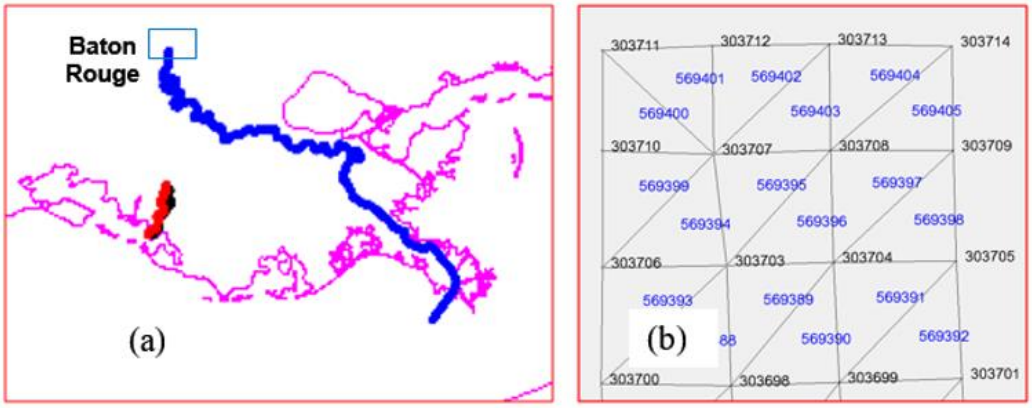

Figure 45. (a) The blue line depicts the location of a series of model grid nodes from Baton Rouge to the end of the southeast branch of the lower Mississippi River entrance to coastal waters. The blue rectangle near Baton Rouge illustrates the location of the model grid shown in (b). (b) List of node numbers (black) and element numbers (blue) on the upstream end of the river model grid.

Figure 46. Time series of river discharge specified on node ID 303712 of the model grid.

Figure 47. Time series of river discharge specified on element ID 569403 of the model grid.

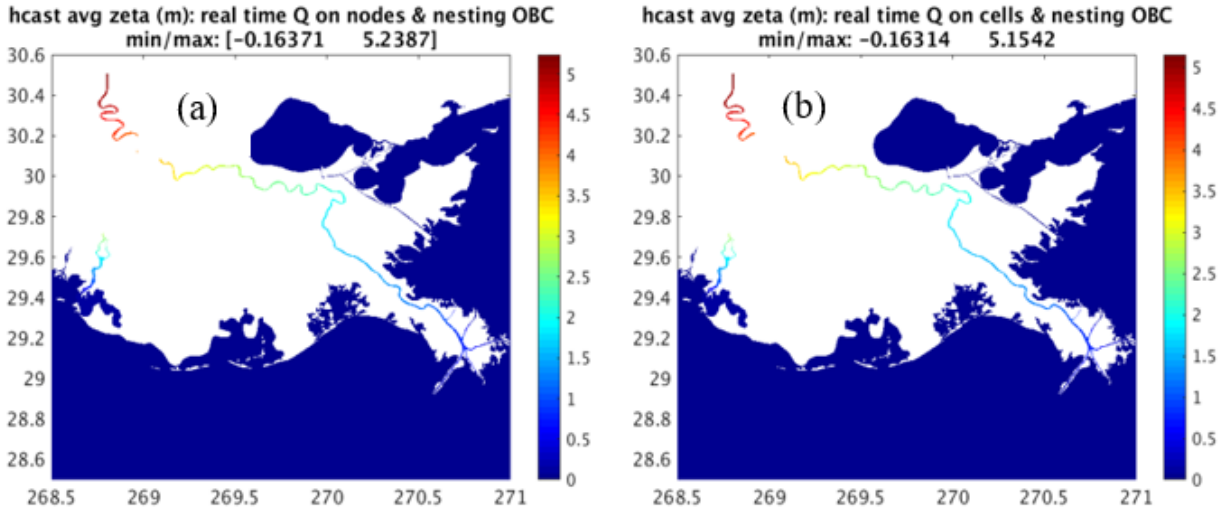

Figure 48. One-year average of water level in the lower Mississippi River area. (a) Forcing on nodes and (b) Forcing on elements.

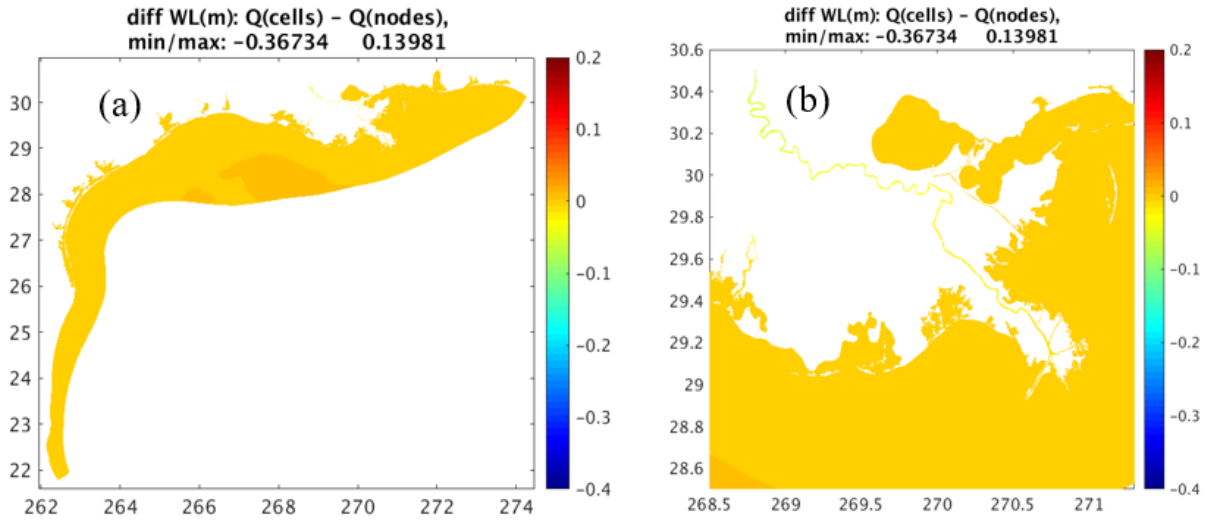

Figure 49. Difference (ΔWL) of the yearly averaged water levels from the two different river discharge approaches, the node approach and the element approach. (a) The entire model domain and (b) the lower Mississippi River area.

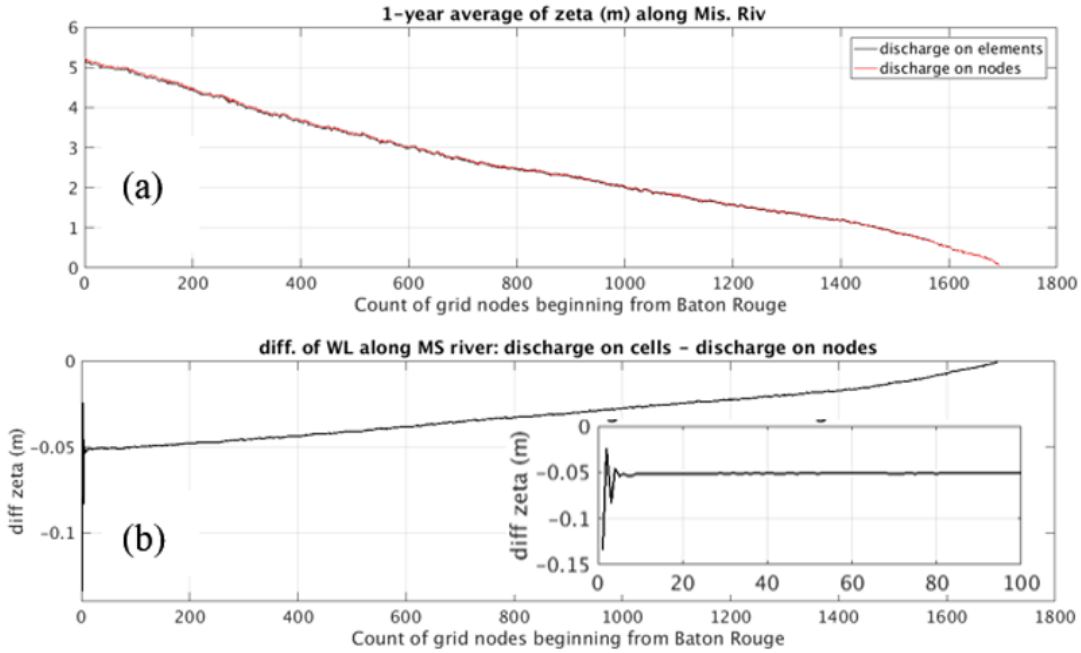

Figure 50. One-year averaged water level along the lower Mississippi River. (a) Water levels from the node (red) and element (blue) forcing and (b) WLavg-node - WLavg-ele . The inset of (b) shows a close up view near the head of river (between nodes 1 and 100) of the plot in (b).

6.2. Impact of Surface Meteorological Forcing and Baroclinic Effect

This section discusses the impact of the combined baroclinic and surface forcing effect on the water level in the lower Mississippi River course. We want to investigate the impact of the meteorological surface forcing on the water level in the Mississippi River throughout the river course. We compared the model generated one-year mean water levels from two different model configurations: (1) a barotropic mode simulation without surface meteorological forcing and (2) a baroclinic mode simulation with a full suite of surface meteorological forcing. The open ocean boundary forcing for (1) is the same as the tidal only simulation of Chapter 4. Being run in barotropic mode, the water temperature and salinity for both the river and in-domain water body were specified to be constant at 15 ^{o}C for temperature and 35 psu for salinity. The configuration of (2) is the same as that used for the hindcast simulation of Chapter 2. Both (1) and (2) make use of 20 sigma layers. The gauge height time series was used as river forcing for both simulations, rather than the river discharge data used for the hindcast simulation. The baroclinic mode simulation used the same surface forcings as those used in the hindcast simulation.

In both cases, we calculated the mean water level (WL_{avg}) for each model node over the one year simulation period. WL_{avg} for the barotropic and baroclinic runs are referred to as $WL_{avg\text{-}BT}$ and $WL_{avg\text{-}BC}$, respectively.

Over the entire model domain, $WL_{avg\text{-}BT}$ ranges between -0.08 m and 6.16 m, whereas $WL_{avg\text{-}BC}$ ranges between -0.16 m and 6.11 m. Figures 51(a) and 51(b) show $WL_{avg\text{-}BT}$ and $WL_{avg\text{-}BC}$ in the lower Mississippi River area. In both figures, the mean water level values demonstrate a similar pattern of spatial variation. In both cases, the decrease in mean water level is from about six meters at Baton Rouge to zero m at the river entrance.

Figure 52(a) displays the difference of the mean water level values, $\Delta WL = WL_{avg\text{-}BC} - WL_{avg\text{-}BT}$, over the entire NGOFS2 model domain. The figure displays two broad bands in contrasting colors: there is a greenish nearshore band along the US coast from the Texas embayments in the west to the Mobile Bay area in the east; there is also a reddish band farther offshore that is nearly parallel to the green band. The green band represents the interval of $-0.2 \text{ m} < \Delta WL < 0$ m; the red band represents the interval of $0 < \Delta WL < 0.15$ m. The band of positive ΔWL values (red band) corresponds to deeper waters compared with the band of negative ΔWL values (greenish band) which corresponds to shallow, near shore, waters. Figure 52(b) is a close up view of the lower Mississippi River area of Figure 52(a). ΔWL decreases from about 5 cm at Baton Rouge to near zero at New Orleans, and drops further to about -15 cm near the river entrance.

Figure 53(a) shows WL_{avg} along the lower Mississippi River course for both the barotropic and the baroclinic mode runs. The two curves demonstrate a very similar trend of variation; both curves decrease monotonically from about 6 m near Baton Rouge to zero m at the river mouth. Figure 53(b) shows $\Delta WL = WL_{avg\text{-}BC} - WL_{avg\text{-}BT}$ along the same path as that of the above. Detailed quantitative review of ΔWL revealed that ΔWL gradually decreases from about 3 cm near Baton

Rouge to -7 cm around node 1500. It then drops drastically to -18 cm at node 1670, and finally shoots up to -7 cm at the river entrance. The behavior of ΔWL from node 1670 to the end of the river course is due to the interaction between the relatively fresh river water and the saline coastal water. The rising water level near the coast reflects the impact of the Mississippi River fresh water outflow.

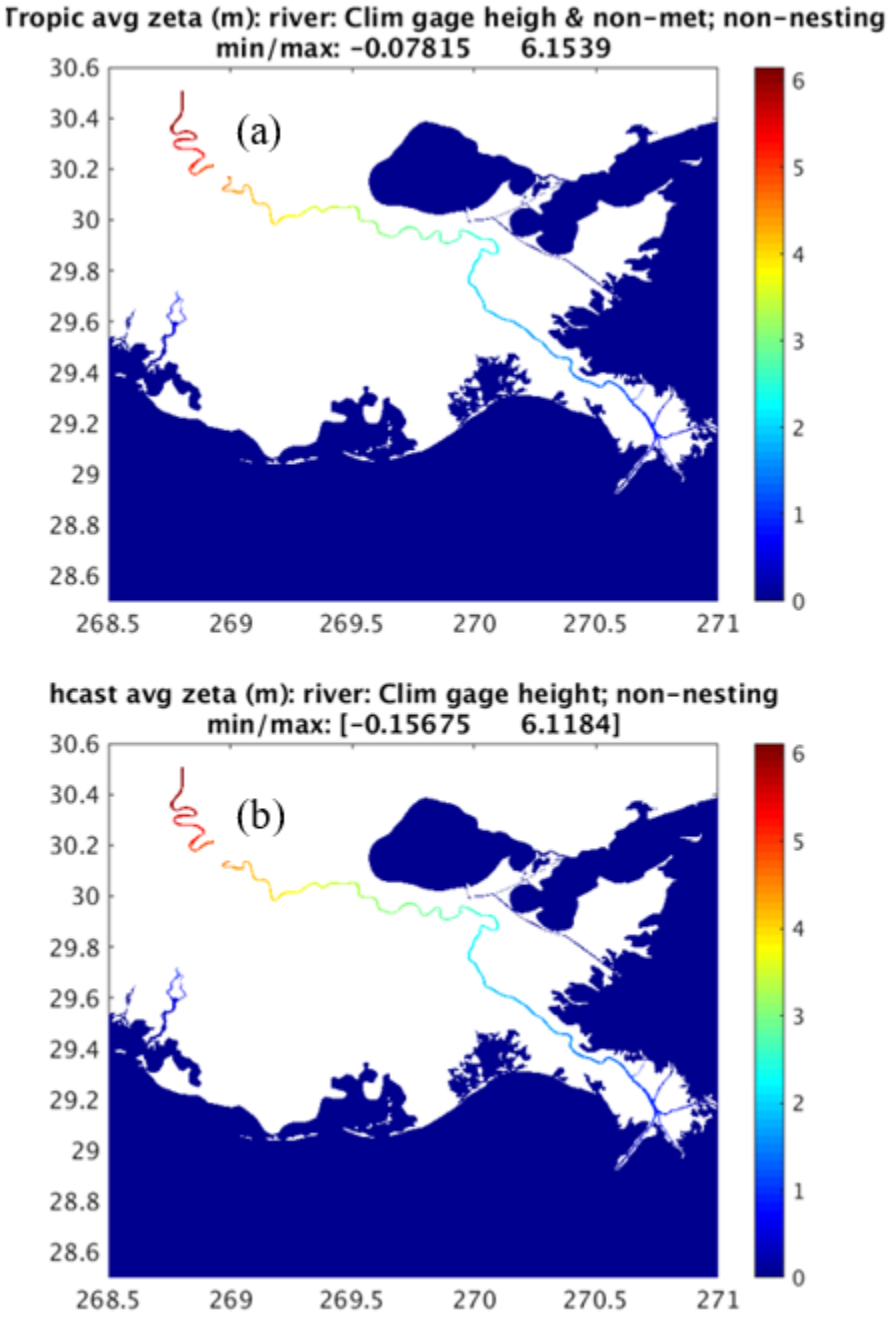

Figure 51. One-year mean water level values from two different model configurations: (a) barotropic mode without surface forcing and (b) baroclinic mode with surface forcing.

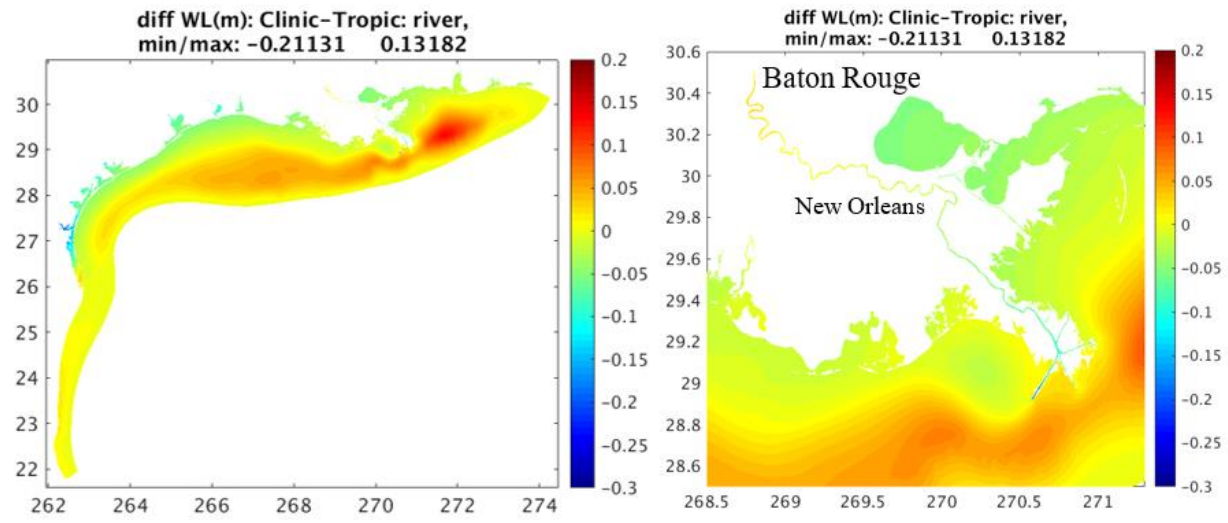

Figure 52. The difference of average one-year water level values baroclinic mode - barotropic mode

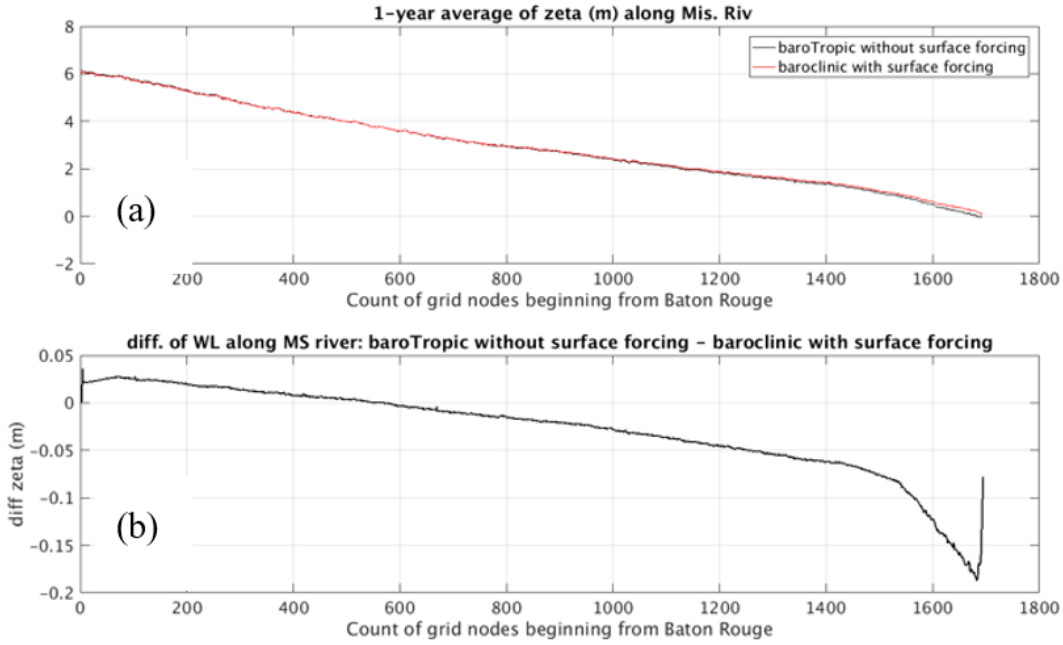

Figure 53. One-year averaged water level along the lower Mississippi River. (a) Water levels from the barotropic mode (red) and from the baroclinc mode (blue) runs and (b) ΔWL = WLavg-BC - WLavg-BT. The inset of (b) shows a close up view, from nodes 1 to 100 (near the upstream boundary of the river), of the plot in (b).

6.3. Nesting vs. Non-Nesting Approaches to Open Ocean Boundary Forcings

This section discusses the impact of two differing types of open ocean boundary (OOB) forcing on the model generated water levels. The two types of forcing used were the nesting (NT) and the non-nesting (NNT) forcing. The nesting type of forcing applies to both water levels and 3-dimensional currents on the OOB. The non-nesting type of forcing applies only to the water levels on the OOB and allows the model algorithm to calculate the current on the OOB.

The model water level time series generated by the NT run and by the NNT run were compared. The simulation period for both model runs was September 2019. Both the NT and the NNT runs use 40 sigma layers in the baroclinic mode, and both runs made use of real time surface meteorological forcing and river discharge forcing.

We calculated the time averaged water level (WL_{AVG}) and the average surface current speed (U_{AVG}) from both the NT and NNT model runs. Figure 54(a) displays the WL_{AVG} difference, ΔWL_{AVG}, of the mean WL value from the NT approach minus the mean WL value from the NNT approach. Figure 54(b) displays the U_{AVG} difference of the mean U value from the NT approach minus the mean U value from the NNT approach.

For both runs, we examined the water level time series at the 128 stations (see the station locations in Figure 59). At some open coast stations in the eastern model domain, WL_{NNC} demonstrates spurious, high-frequency oscillations throughout the one month period. WL_{NC} does not give evidence of this type of signal. The oscillations are evidently numerical noise with amplitudes of less than 5 cm. These high frequency oscillations occur east of the Mississippi Valley only; to the west, the signal is free of this numerical noise.

Figure 55 shows the water level time series from both the NNC and NC runs at six stations. In each plot, the red lines and the blue lines represent results from the NNC and NC runs, respectively. Figures 55(a)-(c) correspond to the eastern domain stations: 8735180, 8760922, and 8736896. Figures 55(d)-(f) correspond to three western domain stations: 8766072, TABSV_B, and 8779748. In general, the two runs agree well in both tidal and subtidal frequencies. However, as depicted in Figures 55(a) and 55(b), two of the eastern stations display the spurious high frequency numerical noise in the NNC run, whereas the three western domain stations (Figures 55(d)-(f)) do not. Station 8736897 is located in the upper Mobile Bay, and the water level time series from this station is depicted in Figure 55(c). There is no evidence of the high frequency numerical noise even though this station is located in the eastern domain. This indicates that the appearance of numerical noise is limited to the open coast region of the eastern model domain.

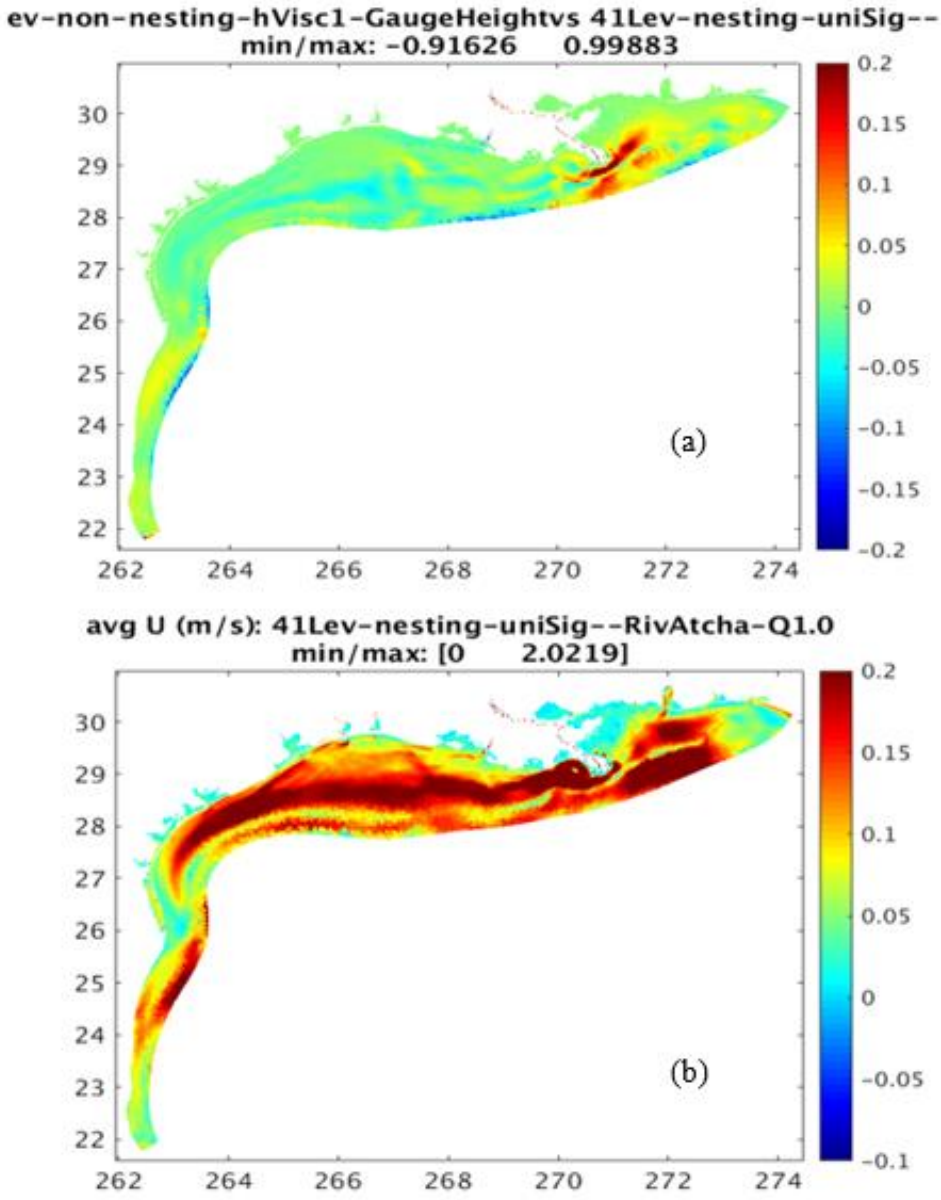

Figure 54. The difference (ΔWL_{AVG}) of the mean WL value from the NT approach minus the mean WL value from the NNT approach. (b) The difference of the mean surface value of U speed (NT) minus the mean surface value of U speed (NNT).

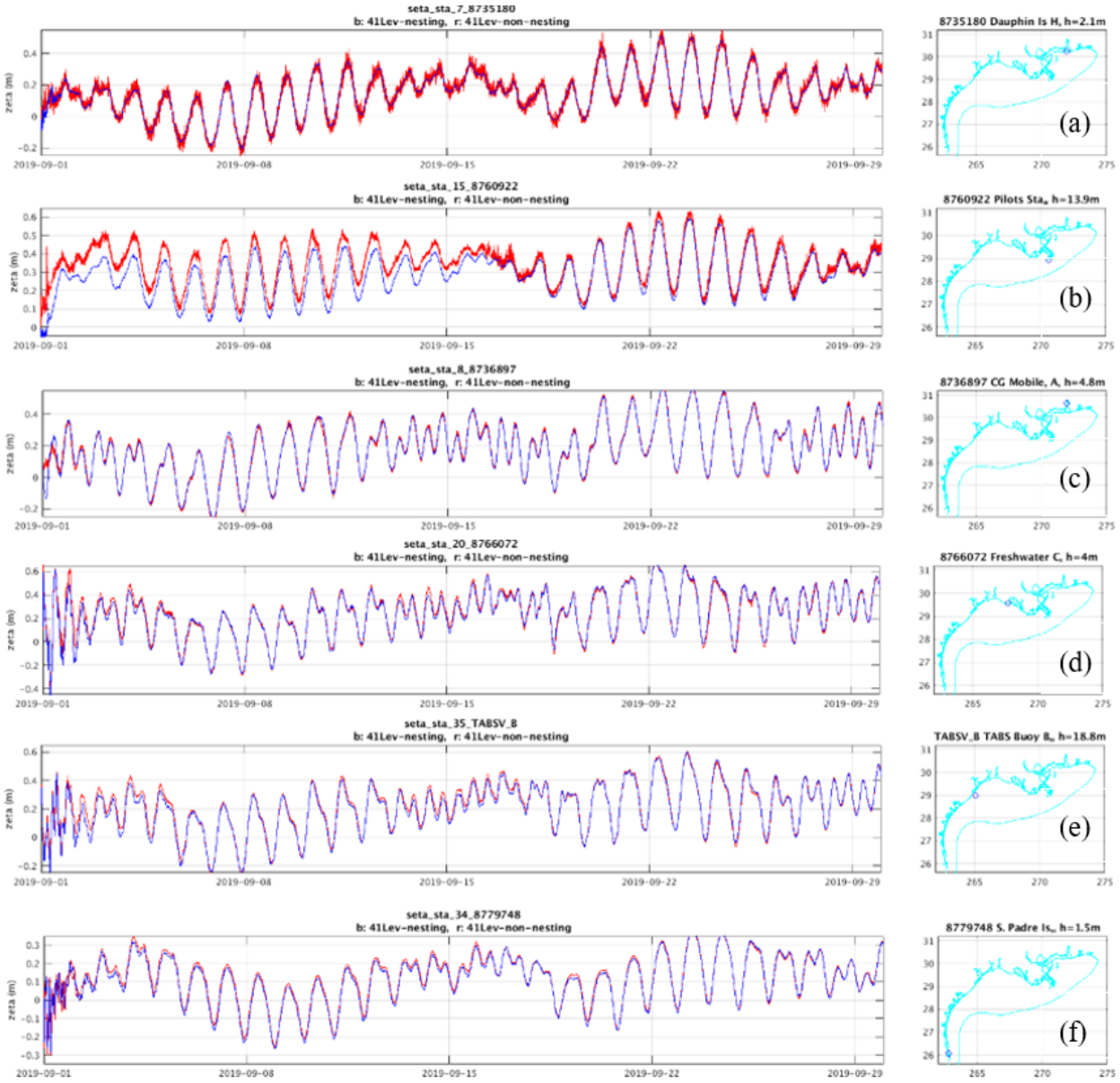

Figure 55. Time series of water levels (left column) from September 2019 and the corresponding station locations (right column). Plots (a)-(f) correspond to stations 8735180, 8760922, 8736897, 8766072, TABSV_B, and 8779748, respectively. In each plot, the blue and red lines represent water levels from the nesting approach and from the non-nesting approach to boundary forcing, respectively.

6.4. River Forcings: Discharge vs. Gauge Height

This section investigates the impact of two types of river forcing, river discharge and gauge height, on the model generated water levels. With FVCOM, the normal way to specify river forcing is to apply the river discharge time series on either the nodes or the elements at the upstream boundary

of the river grid (Section 6.1). If the discharge data are not available, a less traditional approach is to use the river gauge height (GH) data instead. It should be noted that the GH data method is not described in the FVCOM user manual, and is not recommended by the model developer. However, it has been used in practice when river discharge data are not available (Peng et al., 2010).

The USGS river discharge data are estimated by converting the continuously measured gauge height into discharge using the gauge height-discharge (GH-Q) relations: (https://www.usgs.gov/special-topic/water-science-school/science/how-streamflow-measured?qt-science_center_objects=0#qt-science_center_objects). The relations would not necessarily be the same as the algorithm FVCOM employs to make the conversion. Hence, it is not anticipated that the model generated water levels using the gauge height and the river discharge data would be the same. It is worthwhile to investigate the discrepancy between the two cases.

For this comparison, we conducted two one-year hindcast period (August 2016 - July 2017) simulations. The setup of the two model runs of this section are similar to that of the hindcast simulation of chapter 2, except that here we use the daily climatological river discharge and gauge height time series. The data were from the archive of the USGS river database (Chapter 3).

In both cases, we calculated the average water level (WL_{avg}) for each model node over the one year simulation period. WL_{avg} for the gauge height simulation is referred to as $WL_{avg\text{-}GH}$ and WL_{avg} for the discharge simulation is referred to as $WL_{avg\text{-}Q}$. Over the entire model domain, $WL_{avg\text{-}GH}$ ranges between -0.16 m and 6.12 m, whereas $WL_{avg\text{-}Q}$ ranges between -0.16 m and 5.09 m. Figures 56(a) and 56(b) show $WL_{avg\text{-}GH}$ and $WL_{avg\text{-}Q}$ in the lower Mississippi River area. In both cases, WL_{avg} demonstrates a similar pattern of spatial variation. The water level decreases from about 5-6 m at Baton Rouge to nearly zero m in the Mississippi sound.

Figure 57(a) displays the difference of the averaged water level, $\Delta WL = WL_{avg\text{-}Q} - WL_{avg\text{-}GH}$, over the entire NGOFS2 model domain. It shows that the region of evident impact is restricted to the lower Mississippi River course. Figure 57(b) shows a close up view of Figure 57(a) in the lower Mississippi River area. The difference, ΔWL, decreases from about 1 m at Baton Rouge to near zero m near the river entrance to coastal waters.

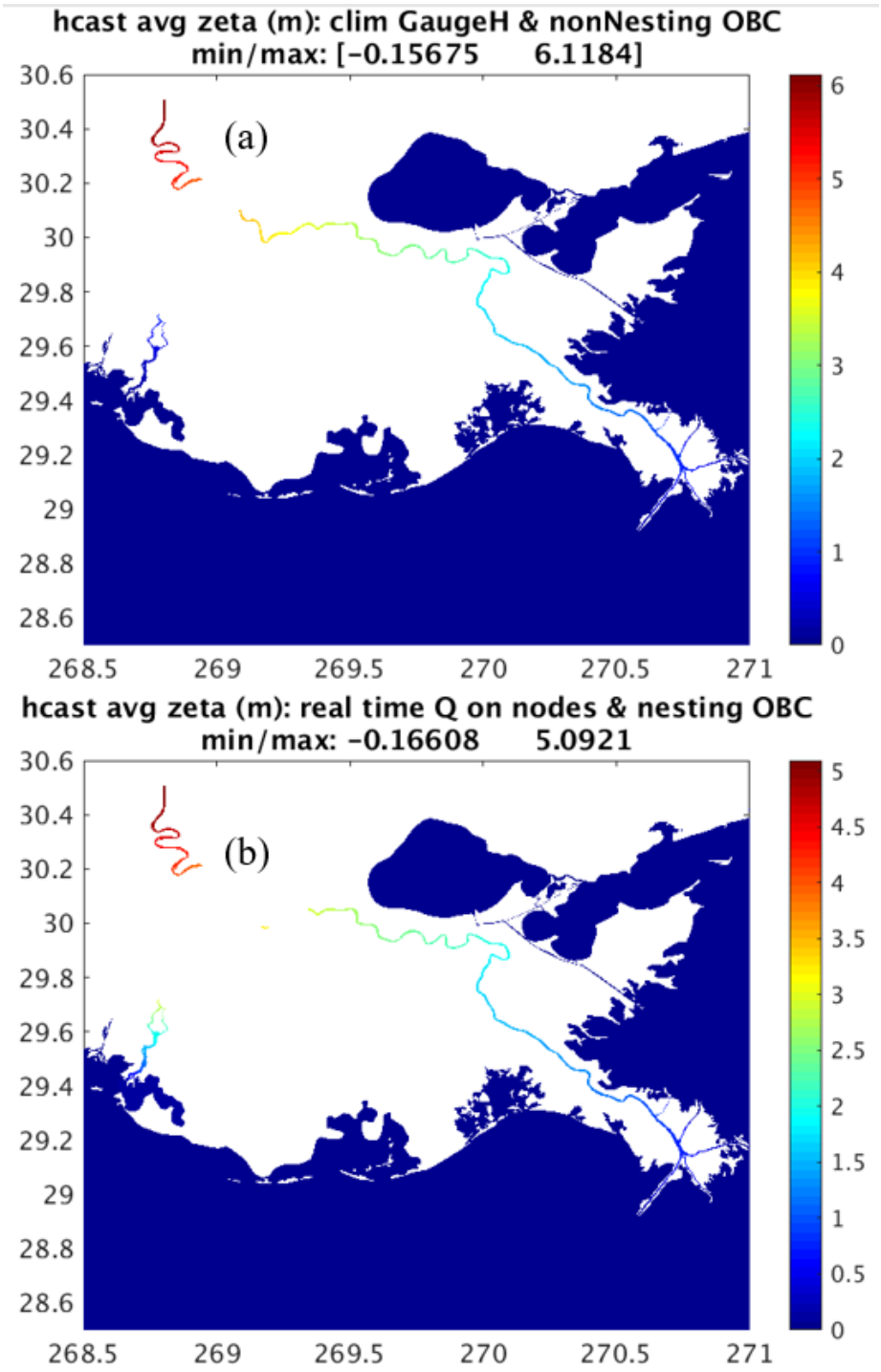

Figure 56. Averaged water level over one year simulation period in the lower Mississippi River area. (a) The model run was forced with climatological gauge height time series and (b) The model run was forced with climatological river discharge time series.

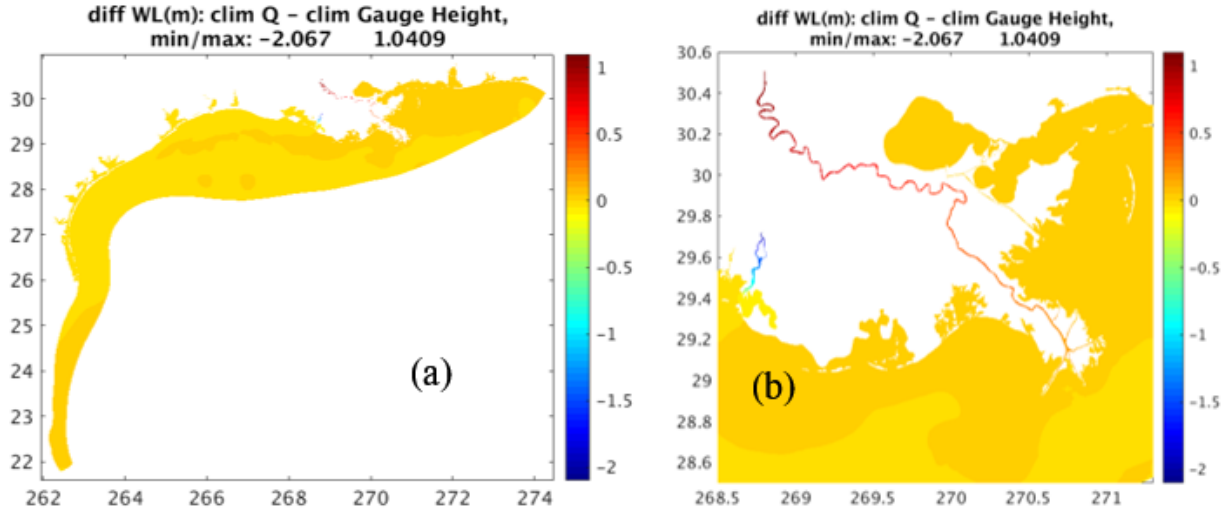

Figure 57. The difference of the one-year averaged water level values from simulations using two different types of river forcings on the lower Mississippi River: river gauge height and river discharge.

Figure 58(a) shows both the $WL_{avg\text{-}GH}$ (black line) and $WL_{avg\text{-}Q}$ (red line) along the lower Mississippi River course. The location of the river course data points is illustrated in Figure 45(a). Figure 58(b) shows ΔWL along the same path as that in Figure 58(a). The inset of Figure 58(b) is a close up view of ΔWL near the upper stream boundary of the river grid. Figure 58 reveals more quantitative water level information than do Figures 56 and 57. The $WL_{avg\text{-}GH}$ and $WL_{avg\text{-}Q}$ both drop monotonically from high values of 6.1 m and 5.1 m, respectively, at Baton Rouge to near zero m near the river entrance to the coastal waters of the Gulf. The WL difference, ΔWL, decreases monotonically from about 1 m at Baton Rouge to near zero meters at the downstream end of the river course. Shown in the inset of Figure 58(b), ΔWL first increases drastically from 0.95 m to 1 m near the upstream river boundary and then behaves more normally as it gradually drops to a near zero value. The dramatic variation of ΔWL near the upper stream boundary can be attributed to the model numerics, rather than to a realistic physical representation of the river's hydrodynamics.

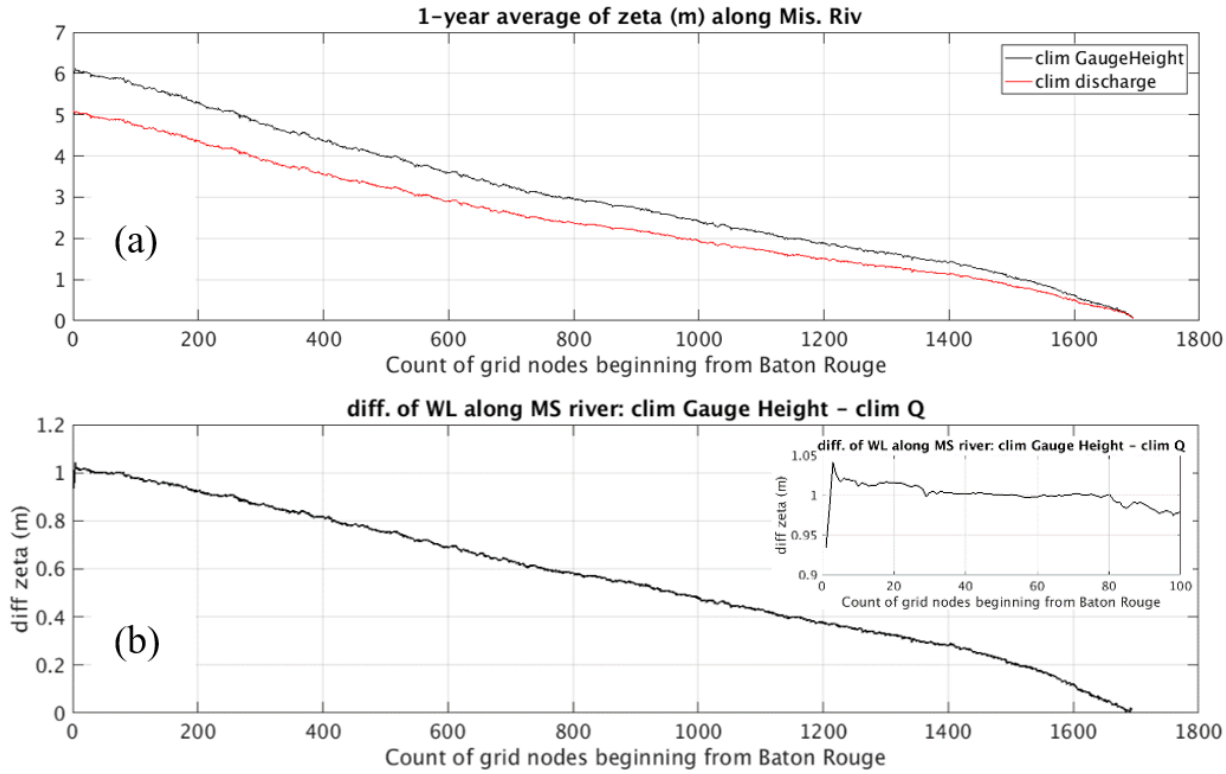

Figure 58. One-year averaged water level along the lower Mississippi River: (a) water levels forced with the river discharge data (red line) and forced with gauge height data (black line) and (b) WLavg-GH - WLavg-Q. The inset of (b) shows a close up view (from nodes 1 to 100) of the plot in (b) in the very upstream portion of the model grid.

6.5. Impacts of vertical Prandtl Number

In the FVCOM, the vertical Prandtl number (vPr) is defined as the ratio of thermal diffusivity to momentum diffusivity (kinematic viscosity). Small values of vPr (e.g., vPr << 1.0) mean that the momentum diffusivity dominates, whereas large values (e.g., vPr >> 1.0) indicate that the thermal diffusivity dominates.

The water level outputs from model runs using vPr = 0.1 and vPr = 1.0 were compared. The two model simulations were conducted for the one-month period of September 2019. The model was configured with 40 uniform vertical layers. The runs were driven with the full suite of forcing parameters including the sea surface wind, heat flux, river discharge, and water levels and currents on the open ocean boundary. The water level time series at 128 stations (see the station map in Figure 59) were analyzed over the final 24 days of the one-month simulations. The initial six days are regarded as the model ramping up period. For this reason, water level results from the first six days were excluded from the analysis.

At each station, we calculated, separately, the mean water level value from the time series of the model run with vPr = 1.0 ($WL_{mean\text{-}vPr1}$) and with vPr = 0.1 ($WL_{mean\text{-}vPr01}$). The difference of the averaged water level values at each station, $\Delta WL = WL_{mean\text{-}vPr1} - WL_{mean\text{-}vPr01}$, was then calculated. Using the time series data, we estimated the root-mean-squared difference (RMSD) between the two runs.

Figures 59(a) shows the color coded map of the mean water level difference (ΔWL_{mean}) by station. ΔWL_{mean} ranges between -0.9 cm and 1.4 cm. The magnitudes of difference are small. At both the offshore stations across the entire model domain and those nearshore stations to the east of Mobile Bay, the values of ΔWL_{mean} appear to be near zero. At the stations along the coastline to the west of Mobile Bay, ΔWL_{mean} ranges between -0.9 cm and -0.1 cm. This indicates that the average water level with vPr=1.0 is lower than that with vPr=0.1. Four outlier stations with ΔWL_{mean} greater than 1.0 are located in the lower Mississippi River course and near the entrance to the Atchafalaya River.

Figures 59(b) shows the color coded map of the root-mean-squared difference (RMSD) of water levels by station. The RMSD ranges from 0 cm to 2.2 cm. The RMSD values demonstrate a similar spatial pattern to that of the ΔWL_{mean}. The largest RMSD values (greater than 1.5 cm) occur at the same four stations as those with the largest ΔWL_{mean}.

Figure 60 shows the water level time series from model runs with vPr=1.0 (blue lines) and vPr=0.1 (red lines) at six stations. Figures 60(a)-(c) correspond to three eastern domain stations: 8735180, 8760922, and 8736896. Figures 60(d)-(f) correspond to three western domain stations: 8766072, TABSV_B, and 8779748. The two model runs produced nearly the same results. At each station from Figures 60(a)-(f), the corresponding $\Delta WLmean$ values are 0.4 cm, 0.3 cm, 0.3 cm, -0.1 cm, -0.2, and -0.6 cm. The corresponding RMSD values are 1.0 cm, 0.7 cm, 1.2 cm, 0.6 cm, 0.5 cm, and 0.8 cm. Results from the two model runs are nearly equal in both the tidal and the subtidal bands. Modeled water levels are not sensitive to differing values of the vertical Prandtl number.

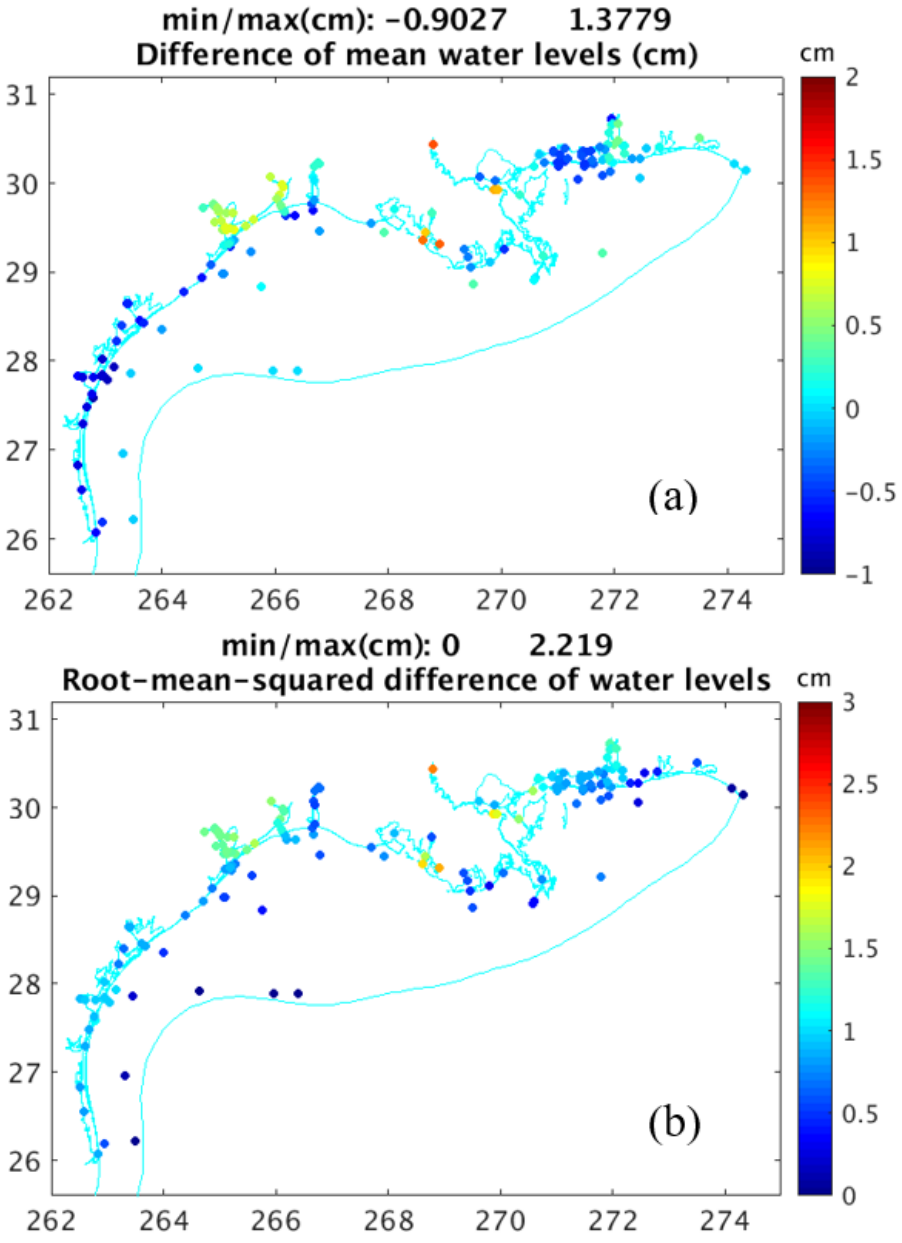

Figure 59. (a) Difference of monthly averaged water level and (b) root-mean-squared water level differences between the model run with vPr = 1.0 and the model run with vPr = 0.1.

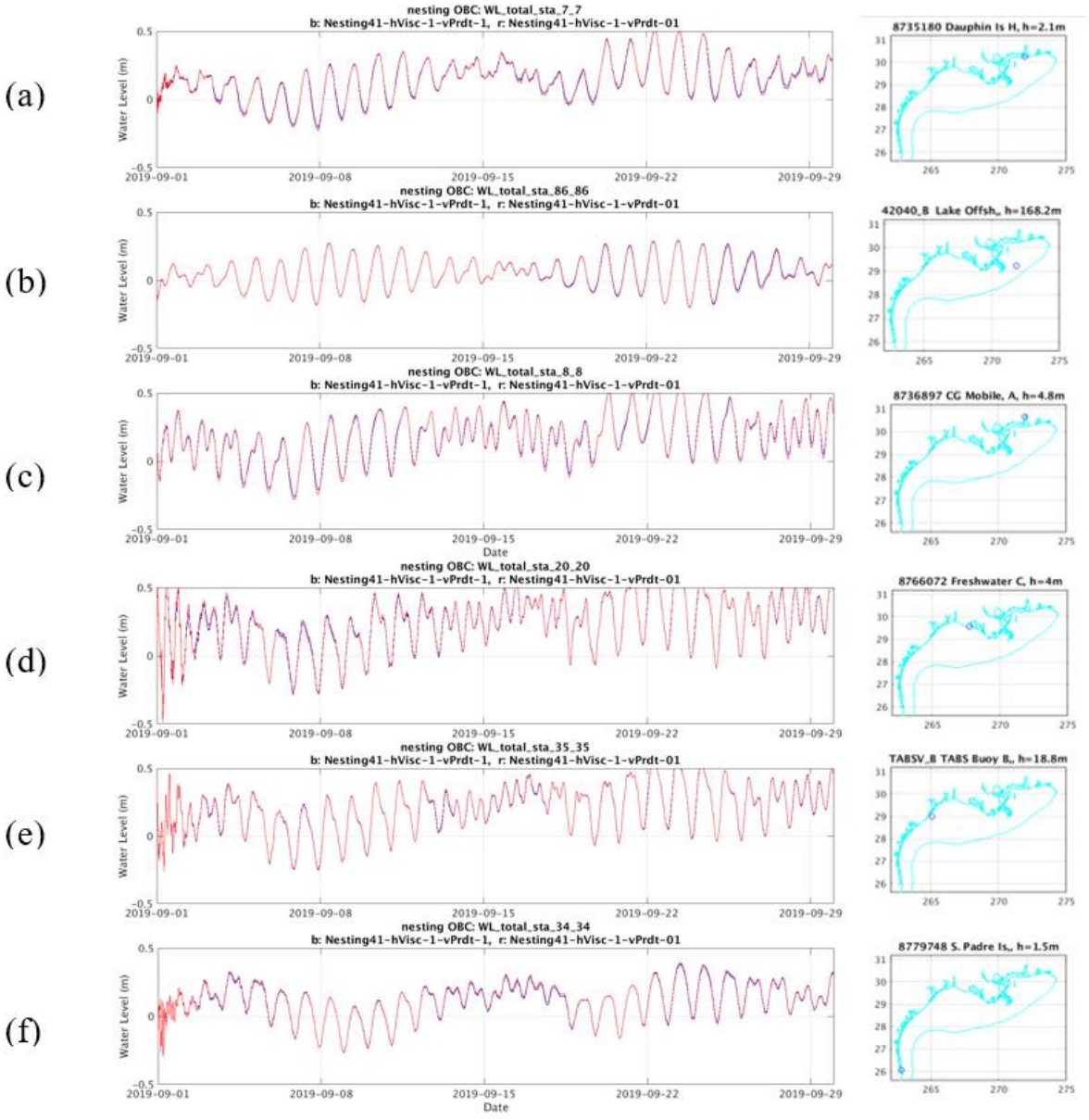

Figure 60. Water level time series (left column) from September 2019 and the corresponding station locations (right column). Plots (a - f) correspond to stations 8735180, 42040B, 8736897, 8766072, TABSV_B, and 8779748, respectively. In each plot, the blue and red lines represent water levels from using vPr equal to 0.1 and 1.0, respectively.

6.6. Vertical Configurations: Uniform vs. non-Uniform Coordinates

This section investigates the sensitivity of model generated water levels to the configuration of the model vertical coordinate. The focus here is to assess the water level discrepancy between the uniform and non-uniform sigma layer specifications. In theory, the Mellor and Yamada Level 2.5 (MY25) turbulence closure scheme (Mellor and Yamada, 1982) will work only in places near the surface and bottom where the surface and boundary layers are resolved. So the main impact will be in deep water, where dynamics are mostly controlled by the boundary conditions (including those for the sea level). In both cases, 40 sigma layers were used.

The FVCOM specifies the vertical coordinates through a suite of parameters defined in the sigma.dat file. The FVCOM user manual explains the details of the file. Table 8 lists the parameter values included in the file for the present uniform and non-uniform configurations. Figures 61(a) and 61(b) illustrate the sigma co-ordinates on the NGOFS2 open ocean boundary nodes, node IDs 1-220.

Table 8. Configurations of the uniform and non-uniform sigma coordinates

Uniform	Non-uniform
NUMBER OF SIGMA LEVELS = 41 SIGMA COORDINATE TYPE = UNIFORM	NUMBER OF SIGMA LEVELS = 41 SIGMA COORDINATE TYPE = GENERALIZED DU = 25.0 DL = 25.0 MIN CONSTANT DEPTH = 200.0 KU = 5 KL = 5 ZKU = 5.0 5.0 5.0 5.0 5.0 ZKL = 5.0 5.0 5.0 5.0 5.0

We conducted a one-month time period (September 2019) simulation using both the uniform and the non-uniform sigma coordinate configurations. The water level time series at 128 stations (see the station map in Figure 59) were analyzed using of the final 24 days of the one month run results. The initial six days are viewed as the model ramping up period. Hence, results in this period were excluded from consideration. At each station, we estimated the mean water level, WL_{U_mean} and WL_{NU_mean}, for the uniform and non-uniform sigma level configurations, respectively.

Figure 62(a) shows the color coded map of water level difference, $\Delta WL_{mean} = WL_{NU\_mean} - WL_{U\_mean}$. ΔWL_{mean} ranges between 0 cm and 3 cm. This indicates that the non-uniform sigma layer configuration produced higher monthly averaged water level values than the uniform sigma level setup. In the eastern domain, WL_{NU_mean} and WL_{U_mean} are nearly the same. In the western domain, WL_{NU_mean} appears to be greater than WL_{U_mean}. Figure 62(b) shows the root-mean-squared difference (RMSD) of water levels between the two runs. RMSD ranges between 0 cm and 4 cm. The spatial pattern is strikingly similar to that of ΔWL_{mean}. RMSD is less than 0.3 cm in

the eastern domain and about 2 - 2.8 cm in the western domain. An outlier value of 3.9 cm occurs at station 42040_B. It is located at -88.21 ^{o}E, 29.21 ^{o}W, offshore from the Mississippi River delta and close to the open ocean boundary of the model grid. The station depth of 168.2 m is the deepest of all stations shown in the plot. The large RMSD value can be attributed to the impact of the deep local bathymetry and the open ocean boundary conditions.

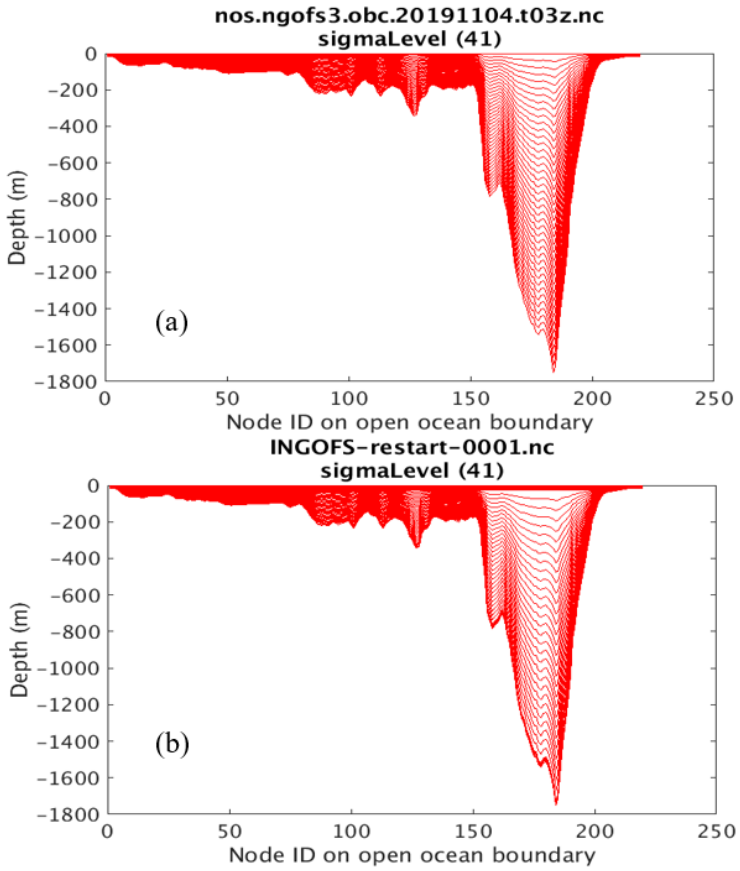

Figure 61. (a) Uniform and (b) non-uniform sigma coordinates.

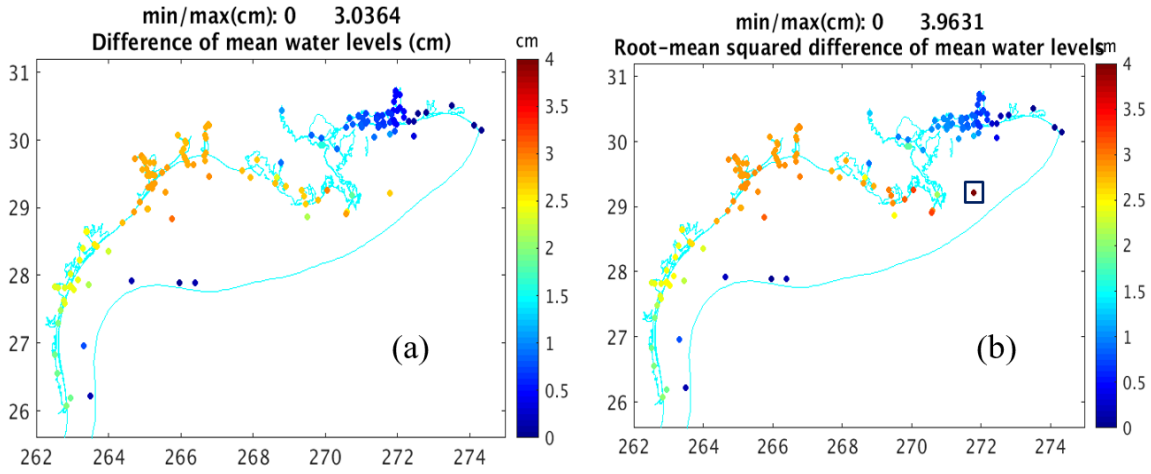

Figure 62. (a) Difference of monthly averaged water level and (b) root-mean-squared water level differences between the uniform and non-uniform sigma coordinate configurations. In plot (b), the station marked with the black square is 42040_B, Lake Offsh.

Figure 63 shows the water level time series of both the uniform (blue lines) and the non-uniform (red lines) coordinate runs at six stations. Figures 63(a)-(c) correspond to three eastern domain stations, namely, 8735180, 8760922, and 8736896. Figures 63(d)-(f) correspond to three western domain stations, namely, 8766072, TABSV_B, and 8779748. In general, the two runs produced very similar results. ΔWL_{mean} at each station from Figures 63(a) to 63(e) are 0.4 cm, 2.6 cm, 0.4 cm, 2.6 cm, 2.7 cm, and 1.9 cm, respectively. The RMSE at these same stations are 0.6 cm, 3.9 cm, 0.7 cm, 2.7 cm, 2.8 cm, and 2.0 cm, respectively. The plots clearly demonstrate that water level time series from the uniform and non-uniform sigma coordinate configurations agree well in both the tidal and nontidal components.

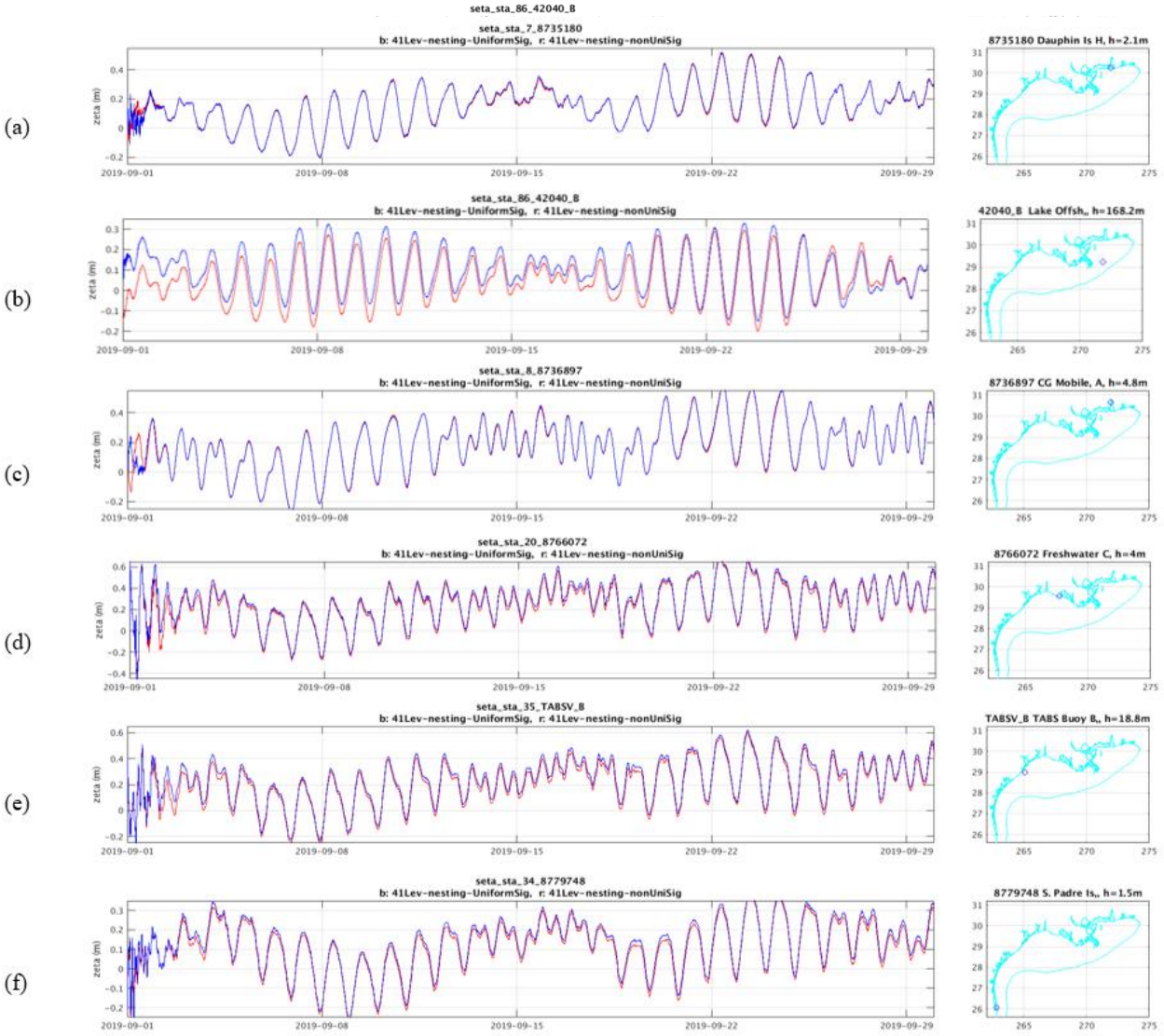

Figure 63. Water level time series (left column) in September 2019 and the corresponding station locations (right column). Plots (a)-(f) correspond to stations 8735180, 8760922, 8736897, 8766072, TABSV_B, and 8779748, respectively. In each plot, the blue and red lines represent water levels from the uniform and non-uniform sigma coordinate configurations, respectively.

7. SUMMARY AND CONCLUSION

This report describes the development of the NOAA/NOS' Upgraded Northern Gulf of Mexico Operational Nowcast and Forecast System (NGOFS2). The NGOFS2 domain encompasses the broad coastal regions spanning from the coast of Mexico in the west to the U.S. Gulf Coast in the northwest, north, and northeast. It was developed to generate operational six-hour nowcast and up to 48-hour forecast guidance of water levels, three-dimensional (3-D) currents, temperatures, and salinity fields. It will support marine navigation, emergency response, search and rescue, offshore oil/gas platform operations, and the environmental management communities.

The NOAA NOS currently operates three OFS, namely Northern Gulf of Mexico OFS (NGOFS), the nested northwest Gulf of Mexico OFS (NWGOFS), and the nested northeast OFS (NEGOFS) in northern Gulf of Mexico (NGOM). In addition to encompassing the combined NGOFS, NWGOFS, and NEGOFS domains, the NGOFS2 domain also covers the Lower Mississippi River course, Lake Pontchartrain, Barataria Bay, the lower Atchafalaya River, Texas coastal inlets, and a portion of the Mexican coastal waters.

This report presents the NGOFS2 configuration, the hindcast setup, and the verification. The NGOFS2 uses the Finite Volume Community Ocean Model (FVCOM) as the core hydrodynamic model. Its model grid is composed of 303,714 nodes and 569,405 elements. The element size ranges from about 45 m in the nearshore area to 11 km on the open ocean boundary. The fine elements favorably resolve the complex coastline and bathymetric features. The vertical coordinate was configured with 20 non-uniform sigma layers for the hindcast simulation.

We performed both a constant density, tidal forcing only simulation (Chapter 4) and a one year (August 2, 2012 – August 1, 2017) period hindcast simulation (Chapter 5). The hindcast simulation included the full suite of forcing factors including tidal and non-tidal water level, current, temperature, and salinity on the open ocean boundary, meteorological forcing on the surface, and river discharge. The tidal forcing data was based on the tidal database of the Advanced Circulation model (ADCIRC). The other forcing data included the G-RTOFS subtidal water level, current, water temperature, and salinity and the NCEP/NAM's surface wind, mean sea level pressure, air temperature, relative humidity, and the USGS river discharge.

The modeled water levels, current, surface temperature, and salinity demonstrated favorably well agreement with in situ observations. For the constant density tidal simulation (Chapter 4), over the 100 stations the average of the absolute model-data difference of the tidal amplitude are 1.5, 1.5, 1.1, and 1.76 cm for K_1, O_1, P_1, and M_2, respectively. The corresponding quantities for tide phase are 10.4, 9.5, 15.0, 20.8 degrees, respectively. For the hindcast results (Chapter 5), the root-mean-squared errors are about 7.4 cm for water levels, about 0.19 cm/s for the current speed, about 12.4 degrees for the current direction, about 1.1 °C for water temperatures, and about 3.8 psu for salinity. The corresponding central frequency (CF) are around 90%, 82.8%, 95.0%, 96.0%, and 70.6 psu, respectively.

In addition to the hindcast simulations, we conducted multiple model runs to investigate impacts of differing model configurations on the model generated water levels in the lower Mississippi

River course (Chapter 6). The discussions covered such topics as (1) river discharge on the model grid nodes vs. elements, (2) impact of surface meteorological forcing and baroclinity, (3) nesting vs. non-nesting approaches of the open ocean boundary (OOB) forcings, (4) differences between the discharge type and gauge height type river forcings, (5) impact of the vertical Prandtl number, and (6) vertical configurations using uniform vs. non-uniform coordinates. The study indicates that the model generated water level, in general, is not sensitive to the configuration types, such as the forcing locations (nodes or elements) of the river discharge, or being with or without surface forcing, or water baroclinity, or vertical Prandtl number, or the uniformity of the vertical coordinate. However, the study unraveled appreciable differences between the nesting and nonnesting type OOB of and between the discharge and gauge height type river forcings. It is noted that in the hindcast setup, NGOFS2 used the nesting type OOB and the discharge type river forcing.

At of the writing of this report, the NOS has implemented the hindcast setup in the NOS standard HPC-COMF environment and completed a one-year period Nowcast/Forecast (N/F) test runs and the associated skill assessment. The model skills fully satisfied the NOS skill assessment criteria. The NGOFS2 will be transitioned into operational productions in fiscal year 2021.

ACKNOWLEDGEMENTS

The authors would like to express sincere gratitude to Drs. Changsheng Chen and Jianhua Qi at the University of Massachusetts for their valuable comments on the system development and hands-on help on the hindcast FVCOM model configurations. Three coleagues at the Coast Survey Development Laboratory of the NOS/OCS, Drs. John Kelley, Lei Shi, and Alexander Kuropov kindly reviewed the manuscript and provided insightful comments and suggestions that substantially improved this report. The authors would like to express our sincere gratitude for their help.

REFERENCES

Burchard, H.; Hetland, R. Quantifying the Contributions of Tidal Straining and Gravitational Circulation to Residual Circulation in Periodically Stratified Tidal Estuaries. *J. Phys. Oceanogr.* **2010**, *40*, 1243–1262.

Center for Operational Oceanographic Products and Services (CO-OP). Water Levels—Station Selection. Available online: http://tidesandcurrents.noaa.gov/stations.html?type=Water+Levels (accessed on 18 March 2018).

Chen, C.; Gao, G.; Zhang, Y.; Beardsley, R.C.; Lai, Z.; Qi, J.; Lin, H. Circulation in the Arctic Ocean: Results from a high-resolution coupled ice-sea nested Global-FVCOM and Arctic-FVCOM system. *Prog. Oceanogr.* **2015**, *141*, 60–80.

Chen, C.; Liu, H.; Beardsley, R. An unstructured grid, finite-volume, three dimensional primitive equations ocean model: Application to coastal ocean and estuaries. *J. Atmos. Oceanic Technol.* **2003**, *20*, 159–186.

Cowles, G.W.; Lentz, S.J.; Chen, C.; Xu, Q.; Beardsley, R.C. Comparison of observed and model-computed low frequency circulation and hydrography on the New England Shelf. *J. Geophys. Res.* **2008**, *113*, C09015, doi:10.1029/2007JC004394.

Dawson, C.W. Abrahart, R.J.; See, L.M. HydroTest: A web-based toolbox of evaluation metrics for the standardized assessment of hydrological forecasts. *Environ. Mode. Softw.* **2007**, *22*, 1034–1052.

Dawson, C.W.; Wilby, R.L. Hydrological modelling using artificial neural networks. *Prog. Phys. Geogr.* **2001**, *25*, 80–108.

DiMarco, S.F.; Howard, M. K.; Reid, R.O. Seasonal variation of wind-driven diurnal current cycling on the Texas-Louisiana Continental Shelf. *Geophys. Res. Lett.* **2000**, *27*, 1017–1020, doi:10.1029/1999GL010491.

Dinnel, S.P.; Wiseman, W.J. Freshwater on the west Louisiana and Texas shelf. *Cont. Shelf Res.* **1986**, *6*, 765–784.

Dzwonkowski, B.; Park, K. Subtidal circulation on the Alabama shelf during the Deepwater Horizon oil spill. *J. Geophys. Res.* **2012**, *117*, C03027, doi:10.1029/2011JC007664.

Elliott, B.A. Anticyclonic rings in the Gulf of Mexico. *J. Phys. Oceanogr.* **1982**, *12*, 1292–1309.

Etter, P.C.; Ulm, W.F.; Cochrane, J.D. The relationship of the wind stress to heat flux divergence of Texas-Louisiana shelf waters. *Cont. Shelf Res.* **1986**, *4*, 547–552.

Garaffo, Z.D.; Kim, H.C.; Mehra, A.; Spindler, T.; Rivin, I.; Tolman, H.L. Modeling of 137Cs as a tracer in a regional model for the Western Pacific, after the Fukushina-Daiichi Nuclear power plant accident of March 2011. *Weather Forecast.* **2016**, *21*, 553–579.

Gough, M. K., A. J. H. M. Reniers,J. H. MacMahan, and S. D. Howden (2016), Resonant near-surface inertialoscillations in the northeastern Gulf ofMexico, J. Geophys. Res. Oceans, 121,2163–2182, doi:10.1002/2015JC011372

Jain, A.; Srinivasulu, S. Development of effective and efficient rainfall-runoff models using integration of deterministic, real-coded genetic algorithms and artificial neural network techniques. *Water Resour. Res.* **2004**, *40*.

Kelly, F.J. Physical oceanography/water mass characterization. In *Mississippi-Alabama Continental Shelf Ecosystem Study: Data Summary and Synthesis. Volume II: Technical Narrative;* Brooks, J.M., Giammona, C.P., Eds.; U.S . Dept. of the Interior, Minerals Mgmt. Service, Gulf of Mexico OCS Region: New Orleans, LA, USA, **1991**.

Longley W.L. Freshwater inflows to Texas Bays and Estuaries, *Ecological Relationships and Methods for Determination of Needs*. Austin, TX: Texas Water Development Board and Texas Parks and Wildlife Department. **1994**, 386pp.

Maksimova, E. V. (2017), On theobserved synoptic signal in theMississippi-Alabama slope flow, J.Geophys. Res. Oceans, 122, 185–192, doi:10.1002/2016JC012320.

Mehra, A.; Rivin, I.; Garraffo, Z.; Rajan, B. Upgrade of the Operational Global Real Time Ocean Forecast System. Available online: https://www.wcrp-climate.org/WGNE/BlueBook/2015/individual-articles/08_Mehra_Avichal_etal_RTOFS_Upgrade.pdf (accessed on 29 October 2016).

Mellor, G.L.; Yamada, T. Development of a turbulence closure model for geophysical fluid problems. *Rev. Geophys.* 1982, 20, 851–875.

Morey, S.; Zavala-Hidalgo, J.; O'Brien, J.J. The seasonal variability of continental shelf circulation in the Northern and Western Gulf of Mexico from a high-resolution numerical model. In *Circulation in the Gulf of Mexico: Observations and Models;* Sturges, M., Lugo-Fernandez, A., Eds.; American Geophysical Union: Washington, DC, USA, **2005**; pp. 203–218.

National Center for Atmospheric Research Staff (Eds). "The Climate Data Guide: Taylor Diagrams." Available online: https://climatedataguide.ucar.edu/climate-data-tools-and-analysis/taylor-diagrams (accessed on 18 October 2018).

National Data Buoy Center (NDBC). Archive of Historical Ocean Data. Available online: http://www.ndbc.noaa.gov/data/historical/ocean/ (accessed on 18 March 2018).

Peng, M., Schmalz, R, Zhang, A., Aikman, F. (2014): Towards the Development of the National Ocean Service San Francisco Bay Operational Forecast System. *J. Mar. Sci. Eng.*, **2014**, 2(1), 247-286; https://doi.org/10.3390/jmse2010247.

Pruessner, A & Fanelli, P & Paternostro, C. (2007). C-MIST: An Automated Oceanographic Data Processing Software Suite. 1 - 5. 10.1109/OCEANS.2007.4449155.)

Smagorinsky, J. General circulation experiments with the primitive equations I. the basic experiment. *Mon. Weather Rev.* **1963**, *91*, 99–164.

Sturges, W.; Lugo-Fernandez, A. *Circulation in the Gulf of Mexico: Observations and Models*; American Geophysical Union: Washington, DC, USA, **2005**.

Szpilka, C.; Dresback, K.; Kolar, R.; Feyen, J.; Wang, J. Improvements for the Western North Atlantic, Caribbean and Gulf of Mexico ADCIRC tidal database (EC2015). *J. Mar. Sci. Eng.* **2016**, *4*, 72.

Taylor, K.E. Summarizing multiple aspects of model performance in a single diagram. *J. Geophys. Res.* **2001**, *106*, 7183–7192, doi:10.1029/2000JD900719.

U.S. Geological Survey (USGS). USGS Water Data for the Nation. Available online: http://waterdata.usgs.gov/nwis/ (accessed on 15 October 2013).

Wei, E.; Yang, Z.; Chen, Y.; Kelley, J.W.; Zhang, A. *The Northern Gulf of Mexico Operational Forecast System (NGOFS): Model Development and Skill Assessment*; NOAA Technical Report NOS CS33: Silver Spring, MD, USA, **2014**.

Wei, E.; Zhang, A.; Yang, Z.; Chen, Y.; Kelley, G.W.; Aikman, F.; Cao, D. NOAA's Nested Northern Gulf of Mexico operational forecast systems development. *J. Mar. Sci. Eng.* **2014**, *2*, 1–17.

Westerink, J. J.; Muccino, J. C.; Luettich, R.A. Resolution requirements for a tidal model of the Western North Atlantic and Gulf of Mexico, Computational Methods in Water Resources IX, Volume 2: Mathematical Modeling in Water Resources. Russell, T.F. et al., Eds.; Computational Mechanics Publications, Southampton, UK, **1992,** pp. 669-674.

Wiseman, W.J.; Rabalais, N.N.; Turner, R.E.; Dinnel, S.P.; MacNaughton, A. Seasonal and interannual variability within the Louisiana coastal current: Stratification and hypoxia. *J. Mar. Syst.* **1997**, *12*, 237–248.

Yang, Z.; Myers, E.; White, S. *VDatum for Eastern Louisiana and Mississippi Coastal Waters: Tidal Datums, Marine Grids, and Sea Surface Topography*; NOAA Technical Memorandum NOS CS 19, U.S. Department of Commerce: Silver Spring, MD, USA, **2010**. Available online: https://vdatum.noaa.gov/download/publications/CS_19_FY09_26_Zizang_VDatum_NewOrleans_techMemor.pdf (accessed on 16 June 2018).

Zhang, A.; Hess, K.W.; Wei, E.; Myers, E. *Implementation of Model Skill Assessment Software for Water Level and Current*; NOAA Technical Report NOS CS 24; U.S. Department of Commerce, National Oceanic and Atmospheric Administration: Silver Spring, MA, USA, 2006.

Zhang, A.; Yang, Z. *High Performance Computer Coastal Ocean Modeling Framework for the NOS Costal Operational Forecast System*; NOAA Technical Report NOS CO-OPS 069. U.S. Department of Commerce: Silver Spring, MD, USA, **2014**. Available online: https://tidesandcurrents.noaa.gov/publications/NOAA_Technical_Report_NOS_COOPS_069.pdf (accessed on 1 June 2018)

Zhang, X.; Marta-Almeida, M.; Hetland, R.D. A high-resolution pre-operational forecast model of circulation on the Texas-Louisiana continental shelf and slope. *J. Oper. Oceanogr.* **2012**, *5*, 1–16.

Zhang, X.; Marta-Almeida, M.; Hetland, R.D. A high-resolution pre-operational forecast model of circulation on the Texas-Louisiana continental shelf and slope. *J. Oper. Oceanogr.* **2012**, *5*, 1–16.

Zhang, Z.; Hetland, R.; Zhang, X. Wind-modulated buoyancy circulation over the Texas-Louisiana shelf. *J. Geophys. Res. Oceans* **2014**, 119, 5705–5723, doi:10.1002/2013JC009763.

Zhang, Z.; Hetland, R.D. A numerical study on convergence of alongshore flows over the Texas-Louisiana shelf. *J. Geophys. Res.* **2012**, *117*, C11010, doi:10.1029/2012JC008145.

Zhao, L.; Chen, C.; Cowles, G. Tidal flushing and eddy formation in Mount Hope Bay and Narragansett Bay: An application of FVCOM. *J. Geophys. Res.* **2006**, *111*, C10015, doi:10.1029/2005JC003135.

Zheng, L.; Weisberg, R.H. Modeling the West Florida coastal ocean by downscaling from the deep ocean, across the continental shelf and into the estuaries. *Ocean Modell.* **2012**, *48*, 10–29, doi:10.1016/j.ocemod.2012.02.002.

Zheng, L.Y.; Weisberg, R.H. Rookery Bay and Naples Bay circulation simulations: applications to tides and fresh water inflow regulation. *Ecol. Model.* **2010**, *221*, 986–996. doi:10.1016/j.ecolmodel.2009.01.024.